PASSIVE SYNTHETIC APERTURE RADAR IMAGING USING COMMERCIAL OFDM COMMUNICATION NETWORKS

DISSERTATION

José R. Gutiérrez del Arroyo, Major, USAF

AFIT/DEE/ENG/12-10

DEPARTMENT OF THE AIR FORCE
AIR UNIVERSITY

AIR FORCE INSTITUTE OF TECHNOLOGY

Wright-Patterson Air Force Base, Ohio

AFIT/DEE/ENG/12-10

PASSIVE SYNTHETIC APERTURE RADAR IMAGING USING COMMERCIAL

OFDM COMMUNICATION NETWORKS

DISSERTATION

Presented to the Faculty

Graduate School of Engineering and Management

Air Force Institute of Technology

Air University

Air Education and Training Command

in Partial Fulfillment of the Requirements for the

Degree of Doctor of Philosophy

José R. Gutiérrez del Arroyo, B.S.E.E., M.S.E.E., M.A.S.
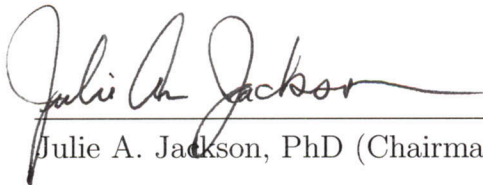
Major, USAF

September 2012

AFIT/DEE/ENG/12-10

PASSIVE SYNTHETIC APERTURE RADAR IMAGING USING COMMERCIAL OFDM COMMUNICATION NETWORKS

José R. Gutiérrez del Arroyo, B.S.E.E., M.S.E.E., M.A.S.
Major, USAF

Approved:

_____   8 Aug 2012
Julie A. Jackson, PhD (Chairman)   Date

_____   15 Aug 2012
Michael A. Temple, PhD (Member)   Date

_____   8 Aug 2012
Mark E. Oxley, PhD (Member)   Date

Accepted:

_____   23 Aug 2012
M. U. THOMAS   Date
Dean, Graduate School of Engineering
and Management

AFIT/DEE/ENG/12-10

Abstract

Modern communication systems provide myriad opportunities for passive radar applications. Orthogonal frequency division multiplexing (OFDM) is a popular waveform used widely in 4G wireless communication networks. Understanding the structure and potential of these waveforms and their networks is critical in future passive radar systems design and concept development. This document introduces research in the collection and processing required to produce passive synthetic aperture radar (SAR) ground images using OFDM communication networks. One such network system is defined by the IEEE 802.16 standard and is known as *Worldwide Interoperability for Microwave Access* or WiMAX. The OFDM-based WiMAX network is selected as a relevant example and is evaluated as a viable source for radar ground imaging. The anatomy of the WiMAX OFDM waveform is explored and carefully applied to radar functions through bistatic ambiguity function analysis and radar design analogies. The monostatic and bistatic phase history models for OFDM are derived and validated with experimental single-dimensional data. An airborne passive collection model is defined based on bistatic geometries and network deployment structures. Then a collection processing design and two multi-symbol signal processing approaches are proposed. These are evaluated using simulations which highlight the impact of several WiMAX-specific items such as the preamble symbols, the cyclic prefix, and the transmission of sequential symbols in downlink subframes. These design approaches are used to propose practical solutions to passive SAR imaging scenarios. Finally, experimental SAR images using general OFDM and WiMAX waveforms are shown to validate the overarching signal processing approach accounting for and/or exploiting WiMAX signal features.

Acknowledgements

Table of Contents

List of Figures

x

List of Tables

List of Acronyms

AAS	adaptive antenna systems
ADC	analog to digital converter
AF	ambiguity function
AMF	averaging match filter
AWG	arbitrary waveform generator
AWGN	additive white Gaussian noise
BER	bit error rate
BPSK	binary phase shift keying
CW	continuous wave
CBP	convolution backprojection
CP	cyclic prefix
CPI	coherent processing interval
DAB	digital audio broadcast
DC	direct current
DFT	discrete Fourier transform
DL	downlink
DS	direct signal
DSL	digital subscriber line

DSO	digital storage oscilloscope
DSP	digital signal processing
DVB-TV	digital video broadcast television
FCH	frame carrier heading
FFT	fast Fourier transform
FOV	field of view
FLL	frequency lock loop
FM	frequency modulaion
FSMF	full segment match filter
FRFT	fractional Fourier transform
GUI	graphical user interface
GPS	global positioning system
HF	high frequency
HDTV	high definition TV
ICI	inter-carrier interference
ID	identification
IEEE	Institute of Electrical and Electronic Engineers
IFFT	inverse fast Fourier transform
IDFT	inverse discrete Fourier transform

ISAR   inverse synthetic aperture radar

ISI   inter-symbol interference

LO   local oscillator

LCO   local control oscillator

LFM   linear frequency modulation

LOS   line-of-sight

LPF   low-pass filter

LTE   long term evolution

MCPC   multi-carrier phase-coded signals

MIMO   multiple-input-multiple-output

MOCOMP motion compensation point

MUSIC   multiple signal classification

OFDM   orthogonal frequency division multiplexing

OFDMA   orthogonal frequency division multiplex access

PAPR   peak-to-average power ratio

PBR   passive bistatic radars

PCR   passive covert radars

PCL   passive coherent location

PFA   polar formatting algorithm

PHY	physical layer
PLL	phase lock loop
PSF	point spread function
PRF	pulse repetition frequency
PSNR	peak signal-to-noise ratio
QAM	quadrature amplitude modulation
QPSK	quadrature phase shift keying
RAIL	radar instrumentation laboratory
RCS	radar cross section
RF	radio frequency
RSR	reference-to-segment ratio
SAR	synthetic aperture radar
SNR	signal to noise ratio
TDD	time division duplexing
UL	uplink
UHF	ultra high frequency
UWB	ultra-wideband
WiMAX	worldwide interoperability for microwave access
WLAN	wired local area network

PASSIVE SYNTHETIC APERTURE RADAR IMAGING USING COMMERCIAL OFDM COMMUNICATION NETWORKS

I. Introduction

Passive radar systems are designed to detect and track targets using signals of opportunity. Existing operational passive radar designs employ analog broadcasts with a wide variety of time-varying frequency content. These analog broadcasts are random in nature and significantly limit the radar system's ability to produce advanced radar products. The recent emergence of digital broadcasts using orthogonal frequency division multiplexing (OFDM) offers predictable transmission properties not typically found in analog forms. Designed around well-established international standards, the "predictability" of OFDM broadcasts provides the passive radar engineer a knowledge base from which to design advanced radar processing algorithms; algorithms that are otherwise impractical or sometimes impossible using analog transmissions. In particular, synthetic aperture radar (SAR) imaging requirements are typically too complex for the simple random analog transmission to fulfill. In recent years, OFDM waveforms have been considered by many radar researchers as the electromagnetic source in both passive and non-passive radar scenarios, mostly geared towards radar detection and tracking radar functions. **The goal of this research is to understand, evaluate, and provide practical solutions to the use of commercial OFDM signals for SAR imaging within a passive radar construct.**

The benefits of passive radars for military applications is well recognized [97]. Many of its benefits and advantages include the absence of a transmitter which reduces

system cost and payload requirements, coverage of low altitude targets, covertness, increased survivability, and robustness against intentional interference. Unfortunately, their use implies higher algorithm complexity, limited performance and the need for high dynamic range and precision equipment [64].

A passive radar determines ranging and range rate information through the use of non-cooperative or signals of opportunity; it receives and processes returns from a scattering environment illuminated by non-radar sources. Griffith refers to these systems as passive coherent location (PCL) radars [42, 43] while others refer to them as passive covert radars (PCR) [62, 73] or passive bistatic radars (PBR) [98] . In practicality, the descriptive term is irrelevant, and for this work *passive radar* will encompass any radar system that exploits non-radar signals of opportunity. A passive radar system is then a subclass of the more general bistatic and multistatic radar systems which also employ cooperative radar signals.

Communication, television, and radio networks are good examples of non-radar commercial sources which could potentially be used to detect, track, or image targets in an area of interest. Although these signals are available almost anywhere, their exploitation is not without challenges. The passive radar designer simply has no control over the transmitted wave and as such, must work with significant performance limitations. The Lockheed Martin's *Silent Sentry* [34] and the Thales *Homeland Alerter 100* (HA100) [91], which are the first known commercial systems developed, exploit analog FM-radio broadcast transmissions for the detection and tracking of aircraft over large geographical areas.

With the advent of modern communication systems came the availability of digi-

tal waveform transmissions; unveiling new signal processing opportunities. OFDM is a digital waveform modulation scheme employed in many modern cellular and broadband access systems world-wide. OFDM efficiently transfers data using closely allocated frequency subcarriers in a predetermined frequency band. The modulation and demodulation of the signal is achieved by direct use of fast Fourier transform (FFT) and inverse fast Fourier transform (IFFT) respectively. The use of Fourier transforms guarantees the orthogonality of the subcarriers, significantly reducing intra-symbol interference. The OFDM orthogonality properties and the use of FFT for modulation and demodulation fits well with legacy SAR imaging processes such as the polar formatting algorithm (PFA). Furthermore, the multicarrier OFDM wave will inherently have non-zero bandwidth which will be shown to be suitable for range compression.
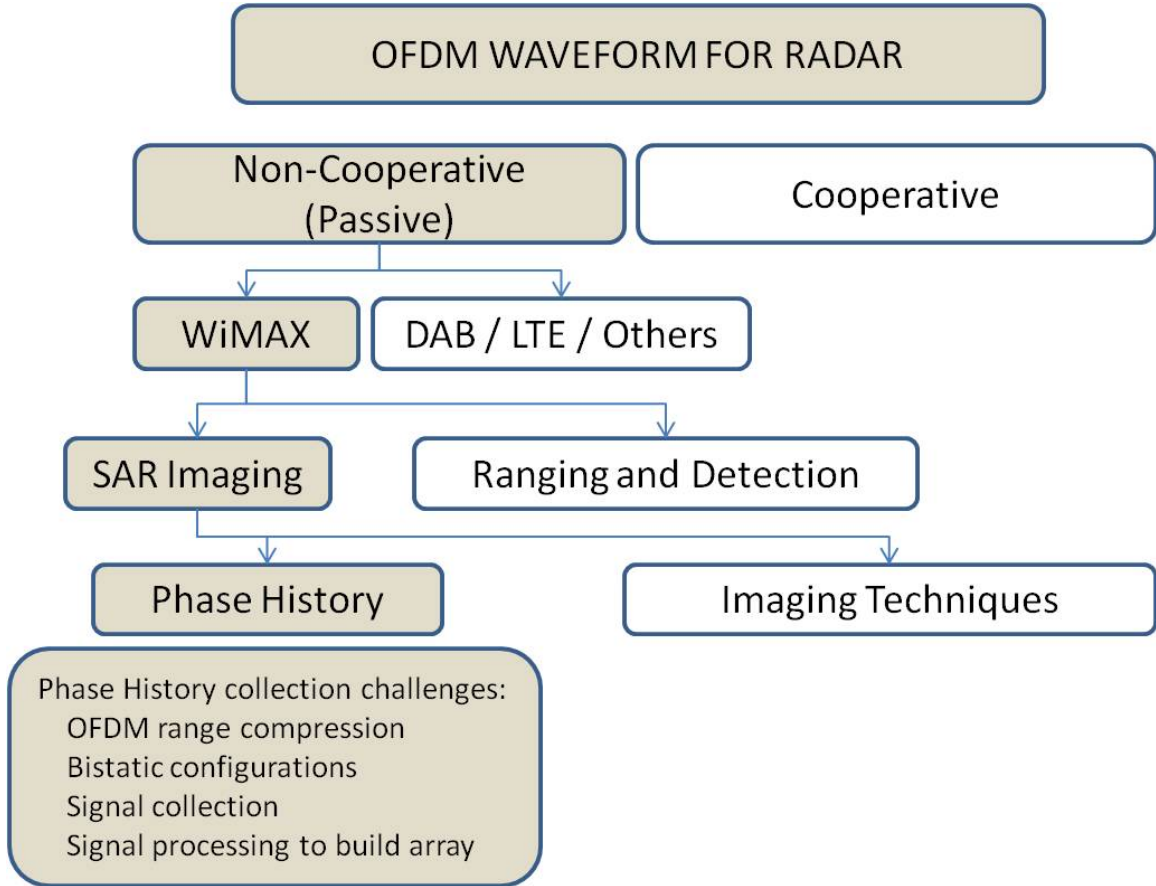
Figure 1. Research road map.

This research focuses on the general understanding of SAR imaging using OFDM waveforms from emerging wireless communication networks. A general research *road map* is shown in Figure 1. Of the many OFDM broadcast networks in existence, the *Worldwide Interoperability for Microwave Access* (WiMAX) broadband network is chosen as the subject study due to its availability and accessibility to its well-known standard. The results of the research should be easily expandable to other existing and future OFDM broadband networks. Within the radar products possible, this research focuses on the SAR imaging aspect which can be divided into: 1) the collection model of ground returns and 2) the signal processing required to achieve the formation of phase histories.

Many SAR image reconstruction and processing techniques exist in the literature to address the image reconstruction challenges, which are not necessarily unique to the OFDM waveforms. That is, once the phase history array is obtained, the signal source becomes irrelevant to SAR reconstruction and image enhancement algorithms. For such reasons, specific research focus is placed on those aspects leading up to the phase history collection. Image reconstruction techniques are employed to produce simulated and experimental imagery supporting specific research concepts.

This document is organized as follows. General background information is included in Chapter II where basic concepts of SAR, bistatic radar, OFDM and WiMAX waveforms are discussed. Chapter III briefly introduces the current state of the art in passive radar and the use of OFDM waveforms in radar systems. The OFDM monostatic and bistatic phase history model is derived and presented in Chapter IV while Chapter V covers the data collection model and signal processing design

4

to build phase histories. Range profile and imaging results using an experimental OFDM radar are presented in Chapter VI where the signal processing design is validated using non-dynamic scenarios. Chapter VII ends the document with a research summary and conclusions, followed by future research recommendations.

II. Background

This research involves concepts from radar, communications, and image processing. The reader is assumed to be familiar with at least basic aspects of all three disciplines to include synthetic aperture radar theory. The intent of this chapter is to briefly introduce concepts, notation, and definitions used throughout the document. The topics discussed include synthetic aperture radar (SAR), bistatic radar, orthogonal frequency division multiplexing (OFDM), IEEE 802.16-2009 (WiMAX), and resolution enhancement methods.

2.1 Synthetic Aperture Radar

The size of a radar antenna in an aircraft platform is unquestionably limited by payload and mounting restrictions, severely limiting the azimuth resolution in radar products. In 1951, Carl Wiley of the Good Year Aircraft Corporation devised an azimuth resolution improvement technique by coherently summing radar pulse returns from a sequence of flight path locations [12]. The concept is called synthetic aperture radar (SAR). The improved azimuth resolution, combined with the range resolution of large bandwidth pulses allow the capability of producing SAR images where scene reflectivity values transduce to pixel intensity values.

The two most common SAR collection modes are *stripmap* and *spotlight*. In stripmap mode, the beam remains at a constant look angle and observes a strip of terrain parallel to the flight path [86]. In spotlight mode, the radar beam is kept fixed looking at the center of the scene of interest during the collection process as shown in Figure 2.
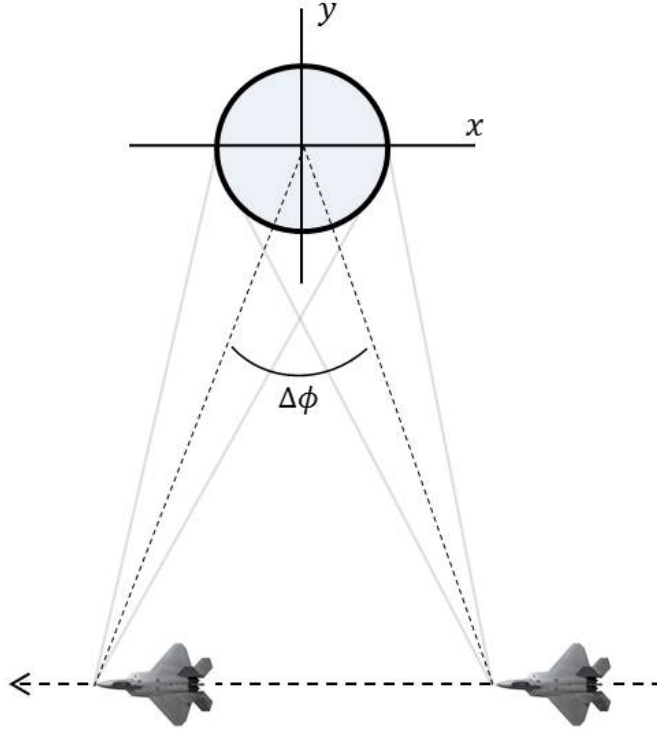
Figure 2. Spotlight SAR collection mode.

Monostatic spotlight SAR image resolution in the down-range (y axis) can be defined by

$$\rho_y = \frac{c}{2B} \tag{2.1.1}$$

and in the cross-range (x axis) by

$$\rho_x = \frac{\lambda}{2\Delta\phi} \tag{2.1.2}$$

where c is the speed of light in meters per second, B is the pulse bandwidth in Hertz, λ is the pulse wavelength in meters, and $\Delta\phi$ is the azimuth collection in radians. Each pulse return is matched filtered (or "compressed" in the case of linear frequency modulation) and sampled in what is commonly known as *fast time* samples. The time each pulse is transmitted defines the *slow time*, resembling the much slower sampling

rate (pulse rate) as the aircraft travels the collection trajectory.

The fast and slow time samples are arranged in a two-dimensional data grid in spatial frequency domain before image formation; the data at this point are known as *phase histories*. Several algorithms and variations thereof are commonly used in the image formation process. An image is easily obtained through a two or three dimensional Fourier transform operation; however, simply transforming the raw data will generally introduce undesired distortion errors. Two of the most common and basic image formation algorithms are the polar formatting algorithm (PFA) and the convolution backprojection (CBP) briefly introduced next. For a more detailed description, the reader is referred to [12, 57, 86].

The Fourier transform and its discrete versions assume that the data is uniformly spaced. The nature of the collection geometry will result in a non-uniform data grid, resembling a section of an annulus in spatial domain. Hence the PFA calls for an interpolation of phase data into a squared uniformly-spaced data grid before the multi-dimensional Fourier transform operation. Alternatively, an image can be reconstructed using backprojection. Used extensively in medical tomography, the CBP is based on the Radon transform introduced by J. Radon in 1917 [77].

2.2 Bistatic Radar

A bistatic radar is one in which the transmitter and receiver are spatially separated. A passive radar system is by default a bistatic radar. When more than one transmitter or receiver is employed the system is known as multi-static radar; not to be confused with the multiple-input-multiple-output (MIMO) radar concept. The
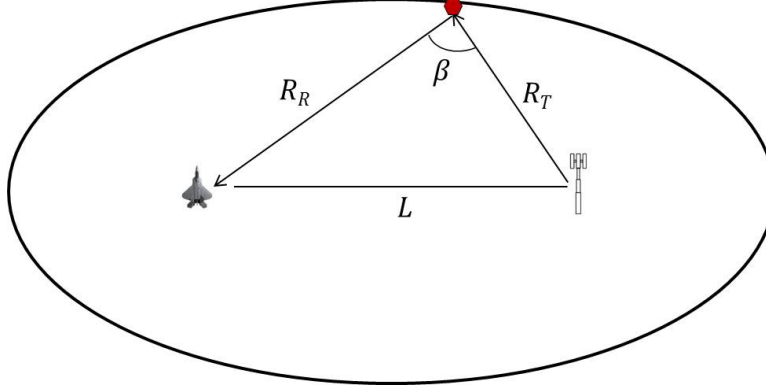
Figure 3. Two-dimensional bistatic geometry.

bistatic concept is fundamental to this research. As such, a detailed description is provided, and the used notation and model conventions are properly defined.

The signal path or *range* from a transmitter to a target to a receiver can be simply defined by

$$R = R_T + R_R \qquad (2.2.1)$$

where R is the total range or signal path length, R_T is the transmitter-to-target range, and R_R is the target-to-receiver range. The two-dimensional concept is best shown in Figure 3 where L is the baseline and β is known as the bistatic angle. Note that the transmitter and receiver are the foci of the isorange ellipse that encompass them. In a bistatic configuration, all the targets lying on the ellipse will have the same range value R. If a target location is desired, multiple receivers must be employed overlapping coverage to determine the intersection of the isorange contours via multilateration [98].

The bistatic radar equation approach is taken from [98] where the equation is developed in two parts. First, the bistatic equation is solved for the *bistatic maximum range product*

$$R_M = \sqrt{(R_T R_R)_{max}}. \qquad (2.2.2)$$

9

Second, ovals of Cassini are plotted against the baseline L to define the geometric properties of the bistatic radar equation in terms of constant signal to noise ratio (SNR). In this way, maximum and minimum ranges, and coverage areas can be determined as a function of R_M.

The range product R_M is the equivalent monostatic range (also known as *geometric mean range*), and represents bistatic radar performance as if receiver and transmitter were collocated. As such, it can be used to relate to the performance of monostatic radar. Willis defines the continuous wave (CW) form of the bistatic maximum range as

$$R_M = \left[\frac{P_T \rho G_T G_R t_c \lambda^2 \sigma_B F_T^2 F_R^2}{(4\pi)^3 k T_i (S/N)_{min} L_T L_R L_{sp}} \right]^{\frac{1}{4}} \tag{2.2.3}$$

where

P_T	transmitter average power
ρ	power utilization factor
G_T	transmitter antenna gain
G_R	receiver antenna gain
t_c	coherent processing interval (CPI) (sec)
λ	wavelength (m)
σ_B	bistatic RCS (m^2)
F_T	pattern propagation factor (transmitter-target)
F_R	pattern propagation factor (target-receiver)
k	Boltzman constant
T_i	receiver input noise temperature (K)
$(S/N)_{min}$	SNR required for detection
L_T	transmitter losses

L_R receiver losses

L_{sp} signal processing losses.

The power utilization factor ρ specifies the fraction of the total transmitter power utilized by the receiver, usually accomplished through band-limiting. Note that coherent processing interval (CPI) is used in lieu of the more commonly used noise bandwidth B_n mainly to discourage attempts at achieving extra long detection ranges by reducing B_n [98]. The CPI is usually limited by the Doppler spread

$$\Delta f_d = t_c^{-1} = B_n. \tag{2.2.4}$$

For bistatic scenarios with significant bistatic angles, the Doppler spread is related to the radial velocity v_r of the bisector $\beta/2$ where the *rule of thumb* defines it as [98]

$$\Delta f_d = \sqrt{\frac{v_r}{\lambda}} \quad \text{bistatic} \tag{2.2.5}$$

which is half of the monostatic version

$$\Delta f_d = \sqrt{\frac{2v_r}{\lambda}} \quad \text{monostatic.} \tag{2.2.6}$$

The bistatic geometries in a passive radar scenario are critical in defining or predicting radar performance. The general bistatic, pseudo-bistatic, and forward scattering geometries are shown in Figure 4.

When the bistatic angle β is close to zero (or baseline $L \approx 0$) , the radar operates with many monostatic characteristics. At the other end, when β approaches 180 degrees, a forward scattering condition exists, and although the clutter scattering coefficients are significantly enhanced, range and Doppler measurements are greatly

11
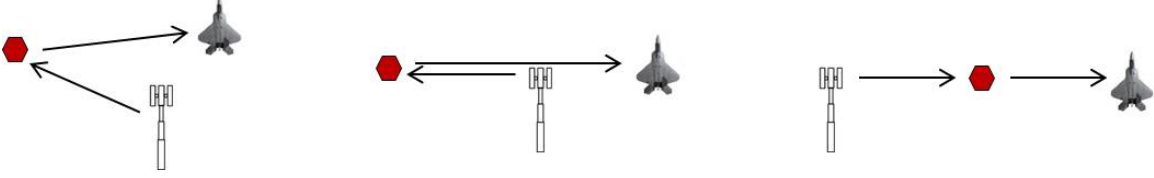
Figure 4. **Three bistatic geometry cases:** *bistatic* (left), *pseudomonostatic* (center), and *forward scatter* (right).

Table 1. Area and range calculation for the four constant SNR cases [98].

Condition	Area	Max R_R	Min R_R
$L = 0$	πR_m^2	R_m	R_m
$L < 2R_m$	$\approx \pi[R_m^2 - (L^4)/(64R_m^2)]$	$\sqrt{R_m^2 + L^2/4} + L/2$	$\sqrt{R_m^2 + L^2/4} - L/2$
$L > 2R_m$	$\approx \pi R_m^2(R_m^2/L^2)$	$L/2 - \sqrt{L^2/4 - R_m^2}$	$\sqrt{R_m^2 + L^2/4} - L/2$
$L \geq 3R_m$	$\approx \pi R_m^2)(R_m^2/L^2)$	$\approx R_m^2/L$	$\approx R_m^2/L$

degraded [89].

Ovals of Cassini are typically used to describe bistatic coverage areas based on detection ranges. These peculiar figures give the bistatic radar designer an idea of radar performance as a function of receiver transmitter baseline L. Constant radar cross section (RCS), pattern propagation factors, and receiving noise temperatures are assumed within the coverage areas. Table 1 details area and range calculations for the four general cases [98].

Figures 5 and 6 show the normalized ovals of Cassinni for the four cases detailed in Table 1. The left focus is the receiver (always at 0) and right focus the transmitter. These contours represent the area of coverage around the transmitter and the receiver for a particular baseline length L. Note that for $L/R_m \geq 2$ the contour no longer shows a single oval. Targets in areas between the separate ovals are no longer detectable and the radar coverage area is significantly reduced. This effect is symmetrical; that is, the receiver and transmitter coverage areas are equivalent. However
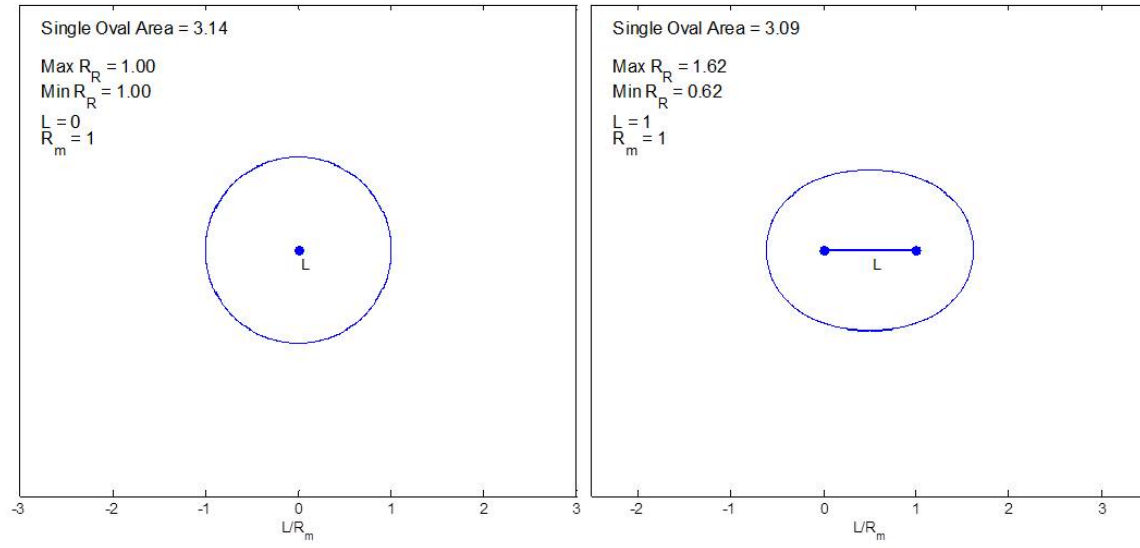
Figure 5. Normalized bistatic radar range and coverage areas. $L/R_m = 0$ **(left),** $L/R_m = 1$ **(right)**
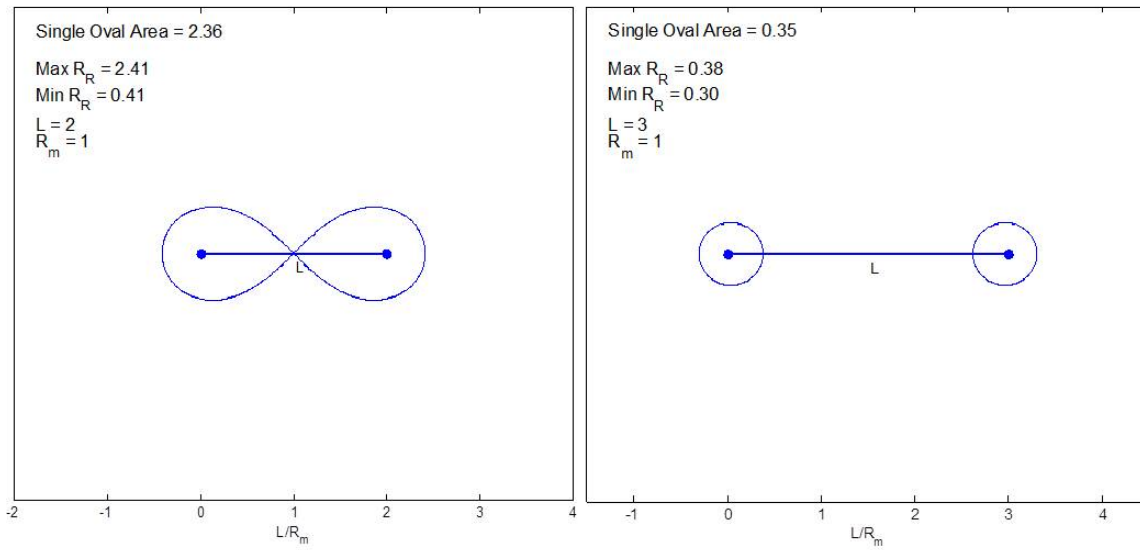
Figure 6. Normalized bistatic radar range and coverage areas. $L/R_m = 2$ **(left),** $L/R_m = 3$ **(right)**

it is this separation that allows extreme remote sensing applications like planetary surface observations using either receiver or transmitter centered approaches [82].

2.3 Orthogonal Frequency Division Multiplexing (OFDM)

An OFDM signal carries coded information in multiple carrier channels simultaneously. A pre-determined bandwidth is partitioned into N subcarriers, each a harmonic of the lowest frequency in the band. In this sense, all subcarriers are mutually orthogonal. The orthogonality allows for close spreading of the data in frequency with minimum interference between them, resulting in a more efficient use of the allocated bandwidth [2].

Although the use of OFDM in communications is widespread, there has been limited research in OFDM for radar applications. OFDM as a radar waveform was formally evaluated by Levanon in [67] [66]. Despite OFDM usability, linear frequency modulation (LFM) has been the waveform of preference for radar imaging due to its range compression and baseband sampling properties.

The OFDM waveform generation begins with a randomized set of data bits modulated using binary phase shift keying (BPSK), quadrature phase shift keying (QPSK), or quadrature amplitude modulation (QAM), producing complex data d_n. The desired signal bandwidth B is divided into N subcarriers evenly spaced in frequency by

$$\Delta f = \frac{B}{N} \tag{2.3.1}$$

where N is the number of the available subcarriers and the discrete Fourier transform (DFT) length. Alternatively, a fixed spacing Δf can be set and have a variable

14
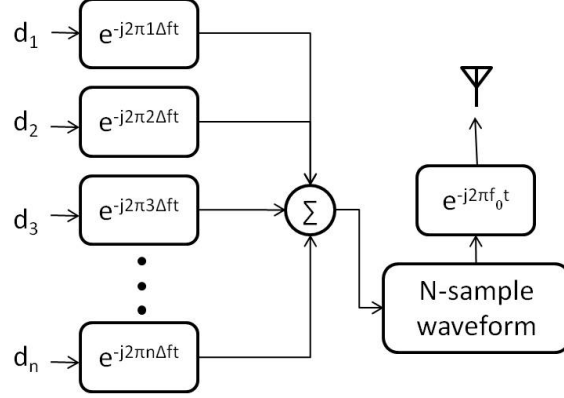
Figure 7. OFDM passband time domain symbol model.

number of subcarriers based on the bandwidth available.

Note the effective signal bandwidth is defined by $B_{eff} = 1/Ts = \Delta f$. Each nth subcarrier is modulated with the amplitude and phase of a particular data d_n. All subcarriers are subsequently assembled in parallel through an inverse DFT operation before transmission. Figure 7 shows a simplified model of the OFDM wave generating process. The time-domain signal becomes a sequence of symbols, each a linear superposition of the N-modulated subcarriers as depicted in Figure 8. The communication symbol duration is defined by $T_s = 1/\Delta f$. For one communication symbol, the OFDM transmitted signal voltage to the antenna is modeled in complex form as [63]

$$s(t) = e^{j\omega_0 t} \sum_{n=0}^{N-1} d_n e^{jn\Delta\omega t}, \ 0 \le t < T_s. \qquad (2.3.2)$$

2.4 802.16-2009, WiMAX

Employing signals of opportunity for radar imaging requires full understanding of the candidate waveform. This section provides a brief introduction to the WiMAX signal structure before and after transmission. For a thorough description, the reader
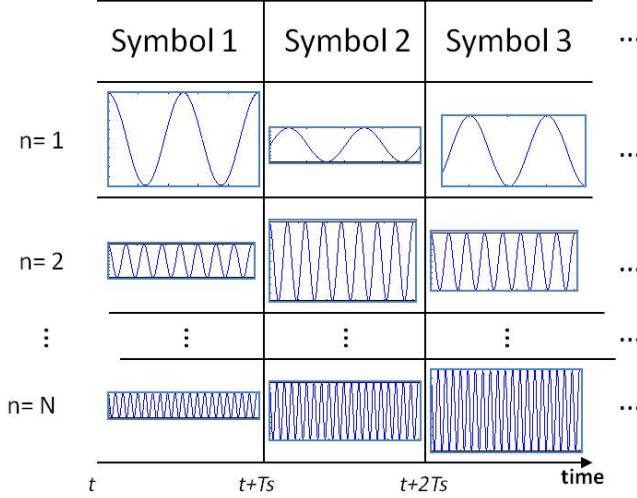
Figure 8. Time domain signal assembly. Symbols in time domain are the linear superposition of N modulated subcarriers.

is referred to the IEEE 802.16-2009 documentation [63].

The *Worldwide Interoperability for Microwave Access* or WiMAX, is a wireless networking standard which aims to address interoperability across IEEE 802.16-2009 standard based products [63]. It is a wireless networking connection for broadband access directly competing against widely-used cable, digital subscriber line (DSL), and T1 systems. As of May 2011, there were 583 fixed and mobile WiMAX deployments in 149 countries [74, 92]. Operating in the frequency band between 2 and 11 GHz, WiMAX systems can provide 5 to 10 km of service area with a maximum data rate of 70 Mbps in a scalable 20 MHz channel [79].

The 802.16-2009 standard defines three physical layer (PHY) configurations [63]: single carrier, 256-point OFDM for fixed stations, and orthogonal frequency division multiplex access (OFDMA) with a maximum of 2048 subcarriers for mobile subscribers. Figure 9 shows a graphical representation of the 256-point OFDM subcarrier structure in the frequency domain. Of the 256 subcarriers, 192 are used for
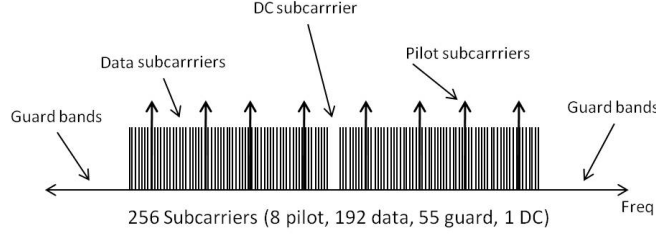
Figure 9. Subcarrier allocation in frequency domain [63].

data, eight are used for pilot codes, and 55 are used for guard bands. The eight pilot bits are equally spaced throughout the bandwidth and are appended to all data symbols after the preamble for channel condition estimation. The DC subcarrier and the guard bands are always null.

The OFDMA PHY mode is based on several FFT sizes: 2048, 1024, 512, or 128. This facilitates support of various channel bandwidths. The active subcarriers are divided into groups of subcarriers forming a *subchannel*. In the downlink (DL), a subchannel may be intended for different (groups of) receivers; in the uplink (UL), a transmitter may be assigned to one or more subchannels and several transmitters may transmit simultaneously. The subcarriers forming one subchannel may, but need not be adjacent [63]. The OFDMA PHY is not considered in this research.

Once transformed to time domain through an inverse DFT operation, a replica of a fraction of the symbol is appended to the beginning to minimize inter-symbol interference (ISI) due to multipath. This replica is defined as the cyclic prefix (CP) with time duration of T_g as shown in Figure 10.

Note that the subcarriers in the WiMAX OFDM PHY are arranged around the
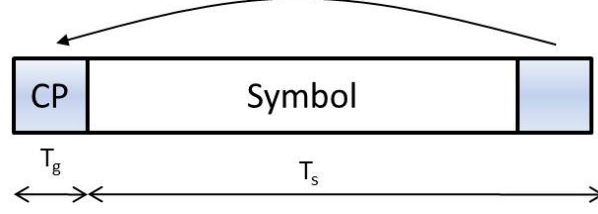
Figure 10. Transmitted symbol (result of one inverse DFT). Cyclic prefix appended at beginning is a replica of the end of the symbol [63].
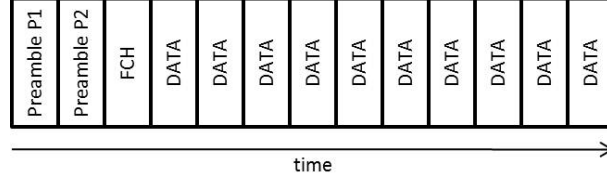
Figure 11. Downlink subframe assembly. Each time block represents a symbol [63].

DC subcarrier ($n = 0$) suggesting the transmitted symbol model [28]

$$s(t) = e^{jw_0 t} \sum_{n=-N/2}^{N/2-1} d_n e^{jn\Delta wt}, \quad -T_g \leq t < T_s \tag{2.4.1}$$

where the symbol duration now includes the CP time extension T_g. The bandwidth of the transmitted symbol is properly defined between $f_c - B/2$ and $f_c + B/2$ where typically $f_c \gg B$ resulting in positive frequencies. After down conversion to baseband in digital domain, the baseband is defined using both negative and positive frequencies about the DC or 0 carrier.

The data symbols are transmitted in time domain using a predefined time division duplexing (TDD) frame structure. Each TDD frame consists of a DL subframe and an UL subframe. For radar applications, only the DL subframe is considered. Figure 11 shows the DL subframe general structure. The DL preamble consists of either one or two symbols and is used for initial ranging and synchronization. For clarity in the document, the first and second preamble symbols are defined as P1

18
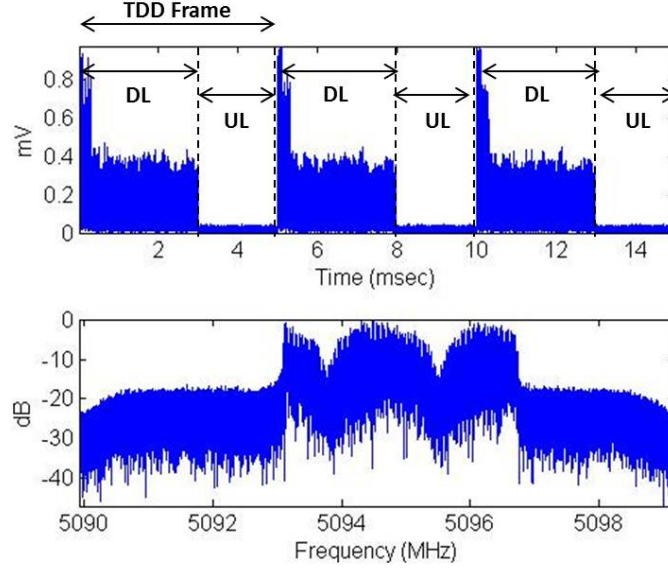
Figure 12. Time and frequency power spectral density responses for three collected WiMAX OFDM TDD frames.: $B = 5$ **MHz bandwidth over a** $f_c = 5.1$ **GHz carrier**

and P2 respectively. The preamble data is subcarrier dependent, always employs the same predefined bit sequence regardless of the operating region, and is 3 dB higher in amplitude relative to the rest of the data symbols. The frame carrier heading (FCH) symbol contains subcarrier mapping information for the entire subframe. Every subframe carries all the necessary details (frame length, number of symbols, number of preambles, etc.) for signal processing at the communications receiver. Figure 12 shows three DL subframes from a real WiMAX signal collected from an experimental WiMAX test bed. The preamble symbols are clearly seen at the beginning of each DL burst. The selective frequency fading is likely due to multipath interference; typically corrected through equalization filters. No UL subframes were transmitted between DL subframes.

A particular feature of WiMAX which will impact SAR image performance is the selection of the sampling frequency f_s. For the OFDM form, the 802.16 standard

Table 2. Values of sampling frequency factor η.

For channel bandwidths B that are multiple of:	η
1.75 Mhz	8/7
1.5 Mhz	86/75
1.25 Mhz	144/125
2.75 Mhz	316/275
2.0 Mhz	57/50
Other	8/7

defines the symbol sampling frequency as

$$f_s = 8000 \left\lfloor \frac{\eta B}{8000} \right\rfloor \tag{2.4.2}$$

where η is a sampling factor greater than 1 which depends on the channel bandwidth B. The possible values of η are shown in Table 2. The processing bandwidth of the DL subframe would technically be f_s. However for document clarity, no distinction will be made between the bandwidth B and sampling frequency f_s; that is, when referring to the WiMAX bandwidth B, f_s is implied. For example: a WiMAX 20 MHz WiMAX DL burst, will implicitly have a bandwidth of $8000 \left\lfloor \frac{(144/125)B}{8000} \right\rfloor = 23.04$ MHz.

2.5 Resolution Enhancement through Compressed Sensing

It will be seen that the WiMAX bandwidth is small when compared to legacy SAR systems, significantly limiting image resolutions levels. Although not within the scope of this research, techniques to enhance the resolution exist and could be applied in future research. One of such techniques is compressive sensing. The primary goals of compressed sensing research is the problem of recovering a signal $\mathbf{f} \in \mathbb{C}^N$ [76] from

noisy linear measurements

$$\mathbf{y} = \mathbf{A}\mathbf{f} + \mathbf{n} \in \mathbb{C}^M \tag{2.5.1}$$

where $\mathbf{y}$ is the measurement vector and $\mathbf{A} \in \mathbb{C}^{M \times N}$ is a forward operator with unit norm columns forming an incomplete basis with $M \ll N$; producing an *ill-posed* problem [76]. Within the SAR context, Cetin formulated the SAR image reconstruction as the optimization problem [15, 16]

$$\hat{\mathbf{f}} = \arg \min_{\mathbf{f}} J(\mathbf{f}) \tag{2.5.2}$$

The cost function $J(\mathbf{f})$ has the form

$$J(\mathbf{f}) = \|\mathbf{y} - \mathbf{A}\mathbf{f}\|_2^2 + \lambda_1^2\|\mathbf{f}\|_p^p + \lambda_2^2\|\nabla|\mathbf{f}|\|_p^p \tag{2.5.3}$$

where the first term incorporates the tomographic SAR observation and geometric model, the second term incorporates prior information regarding the field $\mathbf{f}$ behavior and the nature of point features while the third term considers region features of interest. The Lagrange multipliers λ_1 and λ_2 determine the relative emphasis on the two types of features, $\|\cdot\|_p$ denotes the l_p norm with $p \leq 1$, and ∇ is a two-dimensional derivative operator [16].

III. Previous Work

A literature review was conducted on passive and bistatic radar, OFDM use in radar, and resolution enhancement algorithms. Although many conference papers, journals articles, and technical books are available on the aforemention topics, there was no specific documentation found on SAR ground imaging using commercial OFDM broadband networks. The following is a compilation of the most relevant articles.

3.1 Passive Radar

Passive radar technology has been in existence since the mid 1930's when the *Daventry* experiment was conducted in the U.K. [62]. The use of signals of opportunity has been studied and well documented over the years. Griffiths presented a comprehensive range and Doppler analysis of FM radio, cellular phone and digital audio broadcast (DAB) signals for passive radar locators [19, 42, 43]. Guner focused on the ambiguity function analysis and direct signal path filtering of the DAB [44, 45]. Other signals of opportunity considered are the analog television by Howland [54], digital video broadcast television (DVB-TV) [5], multi-frequency FM [6], high definition TV (HDTV) [13], high frequency (HF) [29, 30], and space-based geostationary sources [25] among others.

The typical passive radar configuration has been a dual receiver setup where one is used to receive target returns and the other the direct signal. This setup requires the identification and removal or cancellation of the main signal, multipath, and clutter to achieve desired levels of target SNR. Colone presents a series of techniques for

clutter, direct signal, and multipath removal in [11, 21, 22, 24].

Passive radar imaging has also received reasonable attention. Most of the passive radar imaging research is focused towards the imaging of moving airborne targets (inverse synthetic aperture radar (ISAR)), employing the passive radar configuration as an air surveillance system. Munson and Lanterman have developed algorithms for ISAR imagery using ultra high frequency (UHF) radio and televisions signals [64, 69, 100] while a super-resolution algorithm is presented in [104]. One of the challenges of passive radar imaging is obtaining sufficient equally distributed frequency samples for the inversion problem (sparse data collections). Wu and Wang present methods to create frequency diverse arrays using multiple narrowband sources [58, 99] while imaging algorithms for sparse data sets are presented in [18, 101]. A novel algorithm for narrowband sources is presented by Yacizi in [93, 103, 107] where through statistical correlation processes, the author eliminates the dependency of the transmitter location in the inverse problem of static and moving targets. Other advanced passive ISAR imaging methods are found in [68, 105, 106]. Cetin introduces the use of compressive sensing for passive radar imaging using television and FM radio sources in [16] while Pengge uses the fractional Fourier transform (FRFT) to produce images from GPS sources [72]. Lastly, Suwa shows results from an ISAR experiment using OFDM-based digital television in [88].

Unfortunately, SAR imaging of two-dimensional ground scenes has received limited attention probably because the concept of the passive radar has been traditionally applied to airborne surveillance. Xuezhi introduces a two-dimensional non-uniform FFT algorithm which eliminated the need for data interpolation [102] and Cazzani shows experimental ground imaging results from a system using a television broad-

casting satellite and a ground-based receiver [14]. But what is perhaps the most relevant and comprehensive analysis of bistatic surface SAR is presented by Rigling in [78,98]. Although not specifically for passive radar, Rigling's general bistatic SAR models and bistatic imagery properties are completely applicable to this research. Other important bistatic radar modeling considerations are found in early documents by Loffeld and Jackson [55,70,71].

3.2   OFDM in Radar Systems

The recent widespread of communication and broadcast OFDM sources of opportunity has spurred multiple passive research topics. The concept of OFDM as a radar waveform is not new. Levanon introduced and evaluated the radar performance attributes of the wave in [66,67]. The waveform, also known as multi-carrier phase-coded signals (MCPC) has favorable ambiguity function, complex envelope and spectrum, when optimized parameters are used. Levanon's general expression for the MCPC complex envelope is:

$$g(t) = \sum_{n=1}^{N} \sum_{m=1}^{M} \omega_n a_{n,m} s[t - (m-1)t_b] e^{j2\pi\left(n - \frac{N+1}{2} \frac{t}{t_b}\right)} \tag{3.2.1}$$

where ω_n is the nth subcarrier complex weight, $a_{n,m}$ is the mth element of the sequence subcarrier n ($|a_{n,m}| = 1$), and $s(t) \equiv 1$ for $0 \leq t \leq t_b$ and zero elsewhere. Note that the form in (3.2.1) describes a sequence of M consecutive *symbols*, each with its own modulation set ω_n. Despite OFDM usability and acceptance into the radar environment, linear frequency modulation (LFM) has been the waveform of preference for radar imaging due to its range compression and baseband sampling properties. The rest of this chapter briefly covers relevant research in the OFDM radar imaging area.

Falcone and Colone recently presented passive radar work using the 802.11 OFDM WiFi signal [31]. The study demonstrates the practical feasibility of a OFDM-based passive radar. The authors describe the signal processing required to remove direct signal breakthrough (from a reference channel) and multipath reflections. The process uses an adaptive cancellation approach which operates by subtracting from the surveillance signal scaled replicas of the reference signal. The authors also discuss monostatic ambiguity function sidelobe control using a Hamming window which shows reasonable performance. The paper ends with the results of an experimental setup in which a moving car and a running man are effectively detected.

In a different paper, Falcone presents a thorough ambiguity function analysis of the WiMAX transmissions [23]. The analysis uncovers the presence of two "types" of side-peaks: the intra-symbol side-peaks which are due to the autocorrelation with the same pulse, and the inter-symbol peaks which are due to the repetition of the pulse during normal transmission. Many of the peaks found are specifically due to fixed and variable pilot carriers, and the guard intervals. In summary, it is expected that the ambiguity function (AF) of a real signal will depend greatly on the transmission mode employed.

An analytical evaluation of the Doppler tolerances of OFDM coded signals was published by Franken [33]. He shows how Doppler resolution is directly proportional to the ratio of the signal bandwidth to the number of subcarriers or $B/N = \Delta f$. Note that the pulse width is determined by $1/\Delta f$; so just like a CW pulse, the longer the pulse, the better the Doppler resolution. One key advantage over LFM is that although OFDM is capable of range compression, there is no range-doppler coupling in its ambiguity function.

Chetty, evaluated the feasibility of using WiMAX as a passive radar waveform for marine surveillance [20]. He employs a surveillance simulation of marine targets at several speeds over open water and shows detection performance on a range-Doppler map. In addition, Chetty presents an analysis of WiMAX maritime radar coverage based on a maximum transmission power of 85 dBm, where detection of medium size vessels is deemed theoretically possible up to a range of 45km.

Similar to Chetty, Wang studies the use of WiMAX as a passive radar waveform using a WiMAX base station in Singapore [96]. Although the presentation is somewhat vague, the experimental results show positive detection of a moving vehicle in presence of a WiMAX field. On another paper, Wang presents the signal model and generation process for a MIMO-OFDM testbed [94]. The intent is to provide a signal generation tool for WiMAX ambiguity function analysis.

Of the authors mentioned herein, perhaps the most publications on the subject of OFDM radar belong to Garmatyuk. He proposes a dual-use waveform for a single system capable of supporting communications and radar processing [36–38,40,41,59,80]. However, the most relevant work is found in [39] and [35] where the author introduces radar imaging concepts using ultra-wideband (UWB) OFDM. Using simulation, Garmatyuk showed that UWB-OFDM imaging has range resolution characteristics similar to other UWB waveforms with the same bandwidth, however no mathematical support is provided. Later, he addresses slow-time signal processing using a least square approach coupled with a grid search to realize estimates of the cross-range phase history of all the subcarriers in strip map mode [35]. The multicarrier approach is geared towards UWB signals, where slow time differences in the subcarriers

phase history are exploitable.

Other related work includes that of Berger [3]. Berger authors a journal article where he describes the signal processing required for a passive OFDM radar using digital audio and digital video broadcast (DAB/DVB). He develops a match filter approach compensating for the phase rotation in time domain caused by Doppler shift. His approach integrates over a series of continuous OFDM blocks using a two-dimensional FFT assuming linear Doppler shift over the integration time (small Doppler approximation). He then discusses and evaluates the multiple-signal classification "MUSIC" and compressive sensing "basis pursuit" signal processing approaches to extract high resolution target information.

Braun presents OFDM range and range rate solutions by establishing maximum likelihood criteria using the return signal model over all symbols in a downlink frame [7]. The formulation was developed for a single point target and results in a two-dimensional search using fast Fourier transformed functions.

The work most relevant to OFDM range compression is that by Sturm. In [84], Sturm shows that when using OFDM waveforms, range profile information can be obtained using the information carried in the pulses. The author's description of the process is summarized in the inverse discrete Fourier transform

$$g(k) = \frac{1}{N} \sum_{n=0}^{N-1} I_{div}(n) e^{j2\pi nk/N} \tag{3.2.2}$$

for $k = [0, \ldots, N-1]$ and where

$$I_{div}(n) = \frac{I_r(n)}{I(n)} \tag{3.2.3}$$

27

In (3.2.3), $I_r(n)$ is the received *soft state* information at the output of the OFDM de-multiplexer before channel equalization and $I(n)$ is the known (or decoded) transmitted information. A subsequent paper showed experimental range profile results using the aforemention approach where he verified practical dynamic range and signal-to-noise (SNR) levels. [85].

3.3 Resolution Enhancement Methods

It will be shown that the attainable resolution using WiMAX broadband OFDM networks is relatively limited. In addition, collection constraints and availability of sources may lead to sparse data collection grids with insufficient information to establish a practical inversion problem. The concepts of resolution enhancement using *compressive sensing* and *weighted extrapolation* are introduced as potential solutions to the aforementioned problems.

General high resolution compressed sensing techniques for radar signals are found in [3, 52, 53, 65]. Formulations specifically for SAR imaging are discussed in [3, 15, 17, 60, 61, 76, 81]. Berger and Cetin extended the compressed sensing algorithms to passive radar designs in [4, 16] using bistatic and multistatic data collection models. A survey of sparse image reconstruction algorithms and randomized measurement strategies are conveniently summarized in [76].

Another resolution enhancement technique is based on spectra extrapolation and estimation [10] using weighted minimum norm. These methods generally produce an initial spectral estimate using *periodograms* on the available samples, followed by a series of iterations converging to the minimum energy extrapolation [56]. The use

of spectral extrapolation on bandlimited SAR imaging collections is discussed and evaluated in [8, 9, 26, 87, 109].

IV. Phase History Model Using OFDM Waveforms

The goal of imaging radar is to obtain an estimate of the two-dimensional scene reflectivity function. The interest is in producing phase history data to assemble a portion of the scene reflectivity spectrum. When using linear frequency modulation (LFM), low-pass filtering after the *dechirp* process directly transduces spatial frequency phase histories [57]. In contrast, demodulating and filtering a continuous wave (CW) pulse results in the convolution in spatial domain of the scene reflectivity function with the system point spread function (PSF). One can think of an OFDM broadcast as the simultaneous transmission of multiple CW pulses over a given frequency band. Using the return signal modeling approach in [57], it is shown that for OFDM signals, phase histories are obtained by a match filtering process using the modulation data. The OFDM range profile solution is initially developed within the monostatic radar construct as in [46], and followed by the bistatic generalization [48].

4.1 Monostatic OFDM Range Compression Model

Consider the transmission of a single OFDM communication symbol as modeled by (2.4.1). Assuming interference-free channels and known modulation data d_n, the received signal from a single OFDM symbol interacting with a ground patch of infinite scatterers in complex form is

$$s_{r0}(t) = A_0 \int_{u_a}^{u_b} g(u) e^{j\omega_0(t-\tau_0-\tau_u)} \sum_{n=-N/2}^{N/2-1} d_n e^{jn\Delta\omega(t-\tau_0-\tau_u)} du \qquad (4.1.1)$$

where $A_0 > 0$ is the gain associated with the radar range equation, $g(u)$ is the

reflectivity as a function of the monostatic slant range u (the limits u_a and u_b represent the near and far ranges of the illuminated scene respectively), τ_0 is the two-way delay associated with the slant range to scene center, and τ_u is the two-way delay associated with differential slant range u with respect to scene center. After mixing the received signal with the in-phase and quadrature-phase of the signal carrier, delayed to the center of the scene $(e^{-j\omega_0(t-\tau_0)})$, the resulting signal becomes

$$
\begin{aligned}
s_r(t) = {} & \frac{A_0}{2} \int_{u_a}^{u_b} g(u) e^{j\omega_0(2t-2\tau_0-\tau_u)} \sum_{n=-N/2}^{N/2-1} d_n e^{jn\Delta\omega(t-\tau_0-\tau_u)} du \\
& + \frac{A_0}{2} \int_{u_a}^{u_b} g(u) e^{-j\omega_0\tau_u} \sum_{n=-N/2}^{N/2-1} d_n e^{jn\Delta\omega(t-\tau_0-\tau_u)} du.
\end{aligned}
\tag{4.1.2}
$$

When low-pass filtering the mixed signal, higher frequency terms are eliminated. The ideal resultant baseband signal then becomes

$$
s_r(t) = \frac{A_0}{2} \int_{u_a}^{u_b} g(u) e^{-j\omega_0\tau_u} \sum_{n=-N/2}^{N/2-1} d_n e^{jn\Delta\omega(t-\tau_0-\tau_u)} du.
\tag{4.1.3}
$$

Bringing the integral term inside the summation and rearranging yields

$$
s_r(t) = \frac{A_0}{2} \sum_{n=-N/2}^{N/2-1} d_n e^{jn\Delta\omega(t-\tau_0)} \int_{u_a}^{u_b} g(u) e^{-j(\omega_0+n\Delta\omega)\tau_u} du.
\tag{4.1.4}
$$

Assuming a monostatic configuration, $\tau_u = 2u/c$. Define a spatial frequency variable $k_n = \frac{2}{c}(\omega_0 + n\Delta\omega)$ which simplifies (4.1.4) to

$$
s_r(t) = \frac{A_0}{2} \sum_{n=-N/2}^{N/2-1} \left[d_n e^{jn\Delta\omega(t-\tau_0)} \int_{u_a}^{u_b} g(u) e^{-jk_n u} du \right].
\tag{4.1.5}
$$

Similar to the LFM case [57], the integral in (4.1.5) is a Fourier transform over the range of discrete spatial frequencies $\frac{2}{c}(\omega_0 - \frac{N}{2}\Delta\omega) \le k_n \le \frac{2}{c}(\omega_0 + \frac{N}{2}\Delta\omega)$ or in terms

31

of signal bandwidth B, $\frac{2}{c}(\omega_0 - \pi B) \leq k_n \leq \frac{2}{c}(\omega_0 + \pi B)$. Letting

$$\int_{u_a}^{u_b} g(u)e^{-jk_n u} du = G[k_n] \tag{4.1.6}$$

and

$$A_n = \frac{A_0}{2} d_n G[k_n] e^{-jn\Delta\omega\tau_0} \tag{4.1.7}$$

reduces (4.1.5) to

$$s_r(t) = \sum_{n=-N/2}^{N/2-1} A_n e^{jn\Delta\omega t}. \tag{4.1.8}$$

Equation (4.1.8) is the Fourier series representation of the received signal for which coefficients are determined by

$$A_n = \frac{1}{T_s} \int_0^{T_s} s_r(t) e^{-jn\Delta\omega t} dt. \tag{4.1.9}$$

Note that the integral in (4.1.9) is the Fourier transform S_n of the received signal $s_r(t)$ for all integers n of which only N subcarriers carry signal energy. Equating (4.1.9) and (4.1.7), and solving for $G[k_n]$ yields

$$G[k_n] = \frac{2S_n e^{jn\Delta\omega\tau_0}}{A_0 T_s d_n} \tag{4.1.10}$$

for all n such that $d_n \neq 0$. Multiplying the numerator and the denominator by the conjugate of d_n results in

$$G[k_n] = \psi_n(S_n d_n^*) \tag{4.1.11}$$

where

$$\psi_n = \frac{2e^{jn\Delta\omega\tau_0}}{A_0 T_s |d_n|^2}. \tag{4.1.12}$$

Equation (4.1.11) reveals a frequency domain match filter operation $(S_n d_n^*)$ where

32

the return signal is matched with the complex subcarrier modulation d_n. The phase history model in (4.1.11) agrees with the one presented in [84], where the author *matches* the return baseband signal in frequency domain to the transmitted modulated data in a transfer function approach. An equivalent match filter form is presented in [3] using a time-domain approach compensating for Doppler shift over a series of symbols.

Note that the reference waveform d_n represents the underlying modulated complex data used to build the OFDM communication symbol. The recreation of the reference waveform d_n can be achieved by either 1) demodulating the data symbol using a communications receiver or 2) when using WiMAX preamble symbols, using the known WiMAX preamble definitions in [63].

In the SAR imaging context the phase history model in (4.1.11) represents a single-dimensional set of N down-range spatial frequency values. Note that the number of useful *fast time* samples is limited to the number of active subcarriers in a WiMAX OFDM transmission. Collecting and processing returns from P receiver locations will then produce the $N \times P$ phase history array required for imaging. Any imaging technique such as the polar reformatting algorithm or convolution backprojection may be employed to recover the image—the estimate of scene reflectivity map.

In summary, the general monostatic process to obtain phase histories in spatial frequency domain on a pulse-by-pulse basis using OFDM is:

1. Fourier transform the return signal

2. Multiply in frequency domain by the conjugate of the complex modulation data.

A one-dimensional range profile can be obtained from any OFDM single-symbol pulse

by applying the inverse Fourier transform to the match filter output over the applicable spatial frequencies k_n.

The spatial frequency support k_n defines a monostatic down-range (y) resolution $\rho_y = c/2B$ and imaging range extent $D_y = N\rho_y$. Note that for a WiMAX OFDM symbol, only 200 of the 256 subcarriers are used. The unused or unmodulated subcarries are used as frequency guardbands (55) and the DC component (1) (see Figure 9). The result will be a reduced bandwidth of $B = 200\Delta f$ with a corresponding down-range resolution of $c/(400\Delta f)$. Similar to the LFM case, the cross-range resolution and extent will depend on the carrier frequency and the number of pulses collected.

4.2   Bistatic OFDM Range Compression Model

Using the diagram shown in Figure 13, the generalization of OFDM range compression to the bistatic model is achieved by replacing the delay to scene center τ_0 and differential delay $\tau(u)$ in (4.1.4) with the bistatic delays τ_0' and $\tau(u')$. Then

$$s_r(t) = \frac{A_0}{2} \sum_{n=-N/2}^{N/2-1} \left[d_n e^{jn\Delta\omega(t-\tau_0')} \int_{u_a'}^{u_b'} g(u') e^{-j(\omega_0+n\Delta\omega)\tau(u')} du' \right] \qquad (4.2.1)$$

where
$$\tau_0' = \frac{R_{T0} + R_{R0}}{c} \qquad (4.2.2)$$

$$\tau(u') = \frac{(R_T + R_R) - (R_{T0} + R_{R0})}{c} \qquad (4.2.3)$$

Since the transmitter on a WiMAX system can be safely assumed stationary and known, it is desired to find an approximation for u' in terms of receiver range and
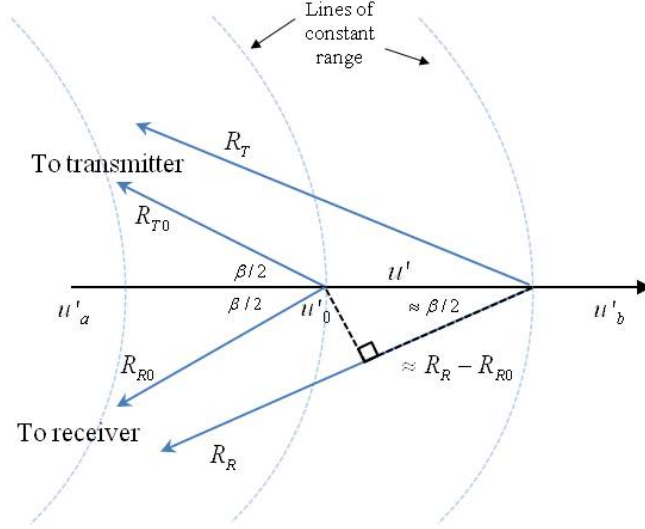
Figure 13. Bistatic collection geometry. The variables u'_a and u'_b define the intersection between the areas illuminated by the transmitter and receiver along the bistatic line of sight. R_T and R_R are the ranges to the transmitter and receiver respectively and the subscript zero is associated with the center of the scene.

bistatic angle, namely $u'(R_{R0}, R_R, \beta)$, where u' represents the vector bisecting the transmitter and receiver line-of-sight (LOS). In this context, u' becomes a *virtual* monostatic view where uniformly spaced differential ranges can be used to define the SAR scene on the bistatic slant plane. Assuming receiver and transmitter ranges R_{R0} and R_{T0} greater than u', and small bistatic angles β

$$u' \cos(\beta/2) \approx (R_T - R_{T0}) \approx (R_R - R_{R0}) \qquad (4.2.4)$$

where the approximation stems from differences in ranges $(R_{R0} \neq R_{T0})$ and the varying bistatic angle along u'. Using (4.2.4) in (4.2.3) yields

$$\tau(u') \approx \frac{2u' \cos(\beta/2)}{c}. \qquad (4.2.5)$$

Define a bistatic spatial frequency variable

$$k'_n = \frac{2(\omega_0 + n\Delta\omega)\cos(\beta/2)}{c} \qquad (4.2.6)$$

which when combined with (4.2.5) leads to

$$G[k'_n] = \int_{u'_a}^{u'_b} g(u')e^{-jk'_n u'}du'. \qquad (4.2.7)$$

Note that (4.2.7) can be treated as a *virtual* monostatic phase history model. The bistatic phenomena is accounted for in the frequency domain spacing k'_n where larger bistatic angles reduce the frequency sample spacing leading to a narrower spatial frequency bandwidth and a coarser down-range resolution. For $\beta = 0$, the model reduces to the monostatic case. This concept agrees with the resolution analyses presented in [98] and [57] which leads to the bistatic down-range range resolution of $\rho'_y = c/(2B\cos(\beta/2))$ and a bistatic imaging range extent of $D'_y = N\rho'_y$. The cross-range resolution and extent will still depend on the carrier frequency and the number of pulses collected, where the discrete azimuth spacing follows the virtual LOS during the collection.

Under the small bistatic angle assumption, (4.2.7) approaches the monostatic model with a linear spacing factor of $\cos(\beta/2)$. It can be shown that under larger β values, the frequency spacing will get "compressed" in a non-linear sense as a function of u', invalidating the Fourier transform form of (4.2.7). Nonetheless, the exact resulting spacing function could be determined through collection geometry and conveniently compensated by non-linear interpolation in the phase history domain along the down-range dimension. Note that the correction will not improve the resolution, it will only provide uniform spacing. The proposed correction approach is beyond the

scope of this research; as such, all bistatic angles are assumed small.

Analogous to the monostatic development, the bistatic phase history in (4.2.7) can be viewed as a Fourier integral with discrete spatial frequencies k'_n. Using the Fourier series approach in (4.1.7)-(4.1.11), the phase history may be solved for as

$$G[k'_n] = \psi'_n (S_n d^*_n) \qquad (4.2.8)$$

where $\psi'_n = 2e^{jn\Delta\omega\tau'_0}/(A_0 T_s |d_n|^2)$. The OFDM match filter correlates the received signal with the transmitted signal, as expected. The derivation of (4.2.8) defines the specific relation between the time domain, spatial domain, and spatial frequency (phase history) domain for OFDM signals in a bistatic scenario. Note that (4.2.8) suggests the same signal processing as for the monostatic case under the aforementioned assumptions. The only difference lies in the spatial frequency spacing which defines the phase history down-range bandwidth.

4.3 OFDM vs LFM

It is worthwhile to provide a brief discussion on similarities and differences of OFDM and LFM waveforms within the imaging domain. The resolution attainable using both waveforms is directly related to the signal bandwidth with a range compression factor [46, 57]. The pulse compression or pulse *dechirp-on-receive* in LFM has the advantage of directly producing a lower bandwidth baseband signal, relaxing the sampling criteria but only in those cases where the pulse length is much longer than the illuminated scene [12, 57, 83]. When the length of the scene of interest is larger than the LFM pulse, match filtering is generally required. OFDM requires

match filtering in either case. However, the filtering is greatly simplified and made efficient through the use of the frequency-domain modulated data and the use of fast Fourier transforms.

A small but convenient advantage of the OFDM phase history is the absence of the residual video phase error associated with the square terms in LFM demodulation. Although several techniques exist in the literature to handle this error [12, 57], it can be completely ignored when using OFDM. Another advantage of OFDM is its simplicity of use. The frequency samples correspond one-to-one to the subcarriers used. The processor can sample the returns at any practical rate and obtain the frequency samples by simple Fourier transform techniques as discussed later in Chapter V.

In terms of transmitting power and energy, LFM and OFDM are simply designed differently with OFDM deserving special consideration. The peak power P_p of a single carrier sinusoidal pulse is defined by $A^2/2$, where A is the maximum amplitude of the signal. The same value applies to an LFM signal where only its frequency is varied as a function of time. In OFDM, N such carriers are transmitted simultaneously. The peak power of the OFDM symbol transmission will depend on the relative phase of its subcarriers with the potential of producing a maximum peak power of

$$P_p = \frac{NA^2}{2} \tag{4.3.1}$$

or N times that of a single carrier. This leads to a high peak-to-average power ratio (PAPR) and creates design challenges in communication systems [28]. The energy delivered by an LFM pulse is a function of its duration. In OFDM, assuming

all of its carriers are in phase, the maximum energy delivered becomes

$$E = \frac{T_s N A^2}{2} = \frac{N A^2}{2\Delta f} \quad \text{per symbol.} \tag{4.3.2}$$

In other words, in LFM the waveform designer chooses a time-bandwith product which leads to desired energy levels [67] whereas in OFDM, these properties become a function of the number of subcarriers N and their separation in frequency Δf. Hence, with proper OFDM design, one could potentially mimic the same power and energy levels achieved with LFM while maintaining a reasonable PAPR. As in any passive radar, these parameters are not in the radar designer control and one can only understand the potential detection ranges based on the OFDM source configuration.

V. Using WiMAX Commercial Transmissions for Passive SAR Imaging

This research considers the possibility of using communication OFDM broadcast networks to perform radar functions in a passive or covert mode. Specifically, the introduction of the *fourth generation* or 4G networks leads to new passive radar concepts and signals-of-opportunity processing ideas. Two examples of emerging OFDM network technologies are the IEEE 802.16-2009 WiMAX and the long term evolution (LTE) broadband networks. Both are based on OFDM and OFDMA transmission schemes. For this research, only the WiMAX network is considered. Radar imaging solutions using WiMAX networks should provide a design base for future extensions to other similar OFDM-based systems. Research efforts are focused on the following:

1. Understanding the OFDM waveform generation, transmission, and reception processes.

2. Monostatic and bistatic phase history model using the general OFDM symbol model.

3. Understanding of the IEEE 802.16-2009 OFDM PHY structure.

4. WiMAX OFDM bistatic ambiguity function.

5. Bistatic data collection model for SAR imaging based on expected WiMAX network configurations.

6. SAR data collection using WiMAX OFDM DL transmissions.

7. Use of the WiMAX preamble in phase history.

8. Two-dimensional WiMAX-based SAR image simulations.

9. Concept validation through the collection and processing of experimental data.

Chapter II introduced the basic concepts of items 1 and 3 while chapter IV shows the development of item 2. This chapter highlights key aspects of the remaining concepts.

5.1 General Assumptions

To maintain a manageable research scope and to establish a research build-up approach, the following general assumptions are adopted:

1. Scatterers in the illuminated scene are single point scatterers.

2. The receiver platform is stationary during the transmission and reception of a single DL (speed of light is much greater than platform velocity).

3. The transmitted WiMAX DL burst has constant relative average power over the signal frequency band.

4. The data transmitted in any WiMAX DL burst is either known or can be extracted via signal demodulation.

5. The WiMAX DL frame rate is constant and stable during the SAR collection period.

6. The impact of Doppler on the transmitted and received pulses is negligible.

7. The power of the users UL transmissions is low and can be ignored at the passive radar receiver.

5.2   WiMAX as a Radar Signal

The WiMAX signal is, by design, a communications signal, optimized for the efficient transmission of high data rates over an allotted bandwidth. However, careful analysis of its structure leads to many characteristics favorable and suitable to radar employment. First, transmission of the DL and UL portions of the frame occur at a predetermined repetition interval. In other words, the DL subframe is transmitted at a certain specific rate analogous to a radar pulse repetition frequency (PRF) in a traditional SAR collection approach. Second, the transmitted signal has non-zero bandwidth (not a single carrier) establishing the fundamental spectral diversity required in the SAR process. Third, the OFDM framework is well suited for data collection forms in spatial domain using efficient FFT processing. Lastly, it is expected that WiMAX (or other similar networks) will eventually provide world-wide coverage over rural and urban areas, providing abundant signals of opportunity for a real worldwide passive radar capability.

Table 3 defines several typical WiMAX parameters "mapped" to radar imaging. Note that WiMAX has bandwidth for range resolution and PRF for cross-range resolution—the basic elements of radar imaging processing. The ratio of the signal bandwidth to the operating frequencies is less than 1%; small enough to be considered narrow-band for Doppler and signal processing purposes [108]. Analogous to the LFM signal, there is a pulse compression factor inherent in the OFDM pulse. When using a single carrier of duration T_s, the effective bandwidth is inversely proportional to the symbol duration: $B_{eff} = 1/T_s = \Delta f$, leading to an effective resolution of $\rho_{eff} = c/2\Delta f$. However, the bandwidth of an N-subcarrier OFDM symbol is

Table 3. Radar parameters for a typical WiMAX signal.

Parameter	Value
Base station tx power	85 dBm
Operating frequency	2-11 GHz
PRF (DL frame rate)	50-400 Hz
Pulse width (one symbol)	0.04-0.7 μs
Bandwidth B	1.25-20 MHz
Range resolution	7.5-120 m
Unambiguous range (one symbol)	375-3000 Km

$B = N\Delta f$, resulting in a range compression factor of

$$\frac{\rho_{eff}}{\rho_y} = \frac{c/2\Delta f}{c/2B} = \frac{cN/2B}{c/2B} \approx N \qquad (5.2.1)$$

The pulse compression value is approximate because there is a slight bandwidth increase caused by a sampling factor $\eta > 1$ as defined by the standard [63]. On a user-controlled OFDM radar system, increasing the bandwidth and the range compression ability of the pulse can be conveniently achieved by increasing the number of subcarriers N used in the pulse generation process.

WiMAX networks are designed to be deployed over large urban and rural areas through the use of tower mounted antennas using line-of-sight (LOS) and non-LOS transmissions. As such, the transmitter locations can be assumed fixed and known. The transmitter-target path and incident angle will always be constant. Phase histories will then depend mostly on receiver location, simplifying the bistatic collection model to only one moving variable.

Although suitable for radar use in many ways, the maximum bandwidth of a current WiMAX DL is 20 MHz [63]; small relative to the bandwidth typically used in
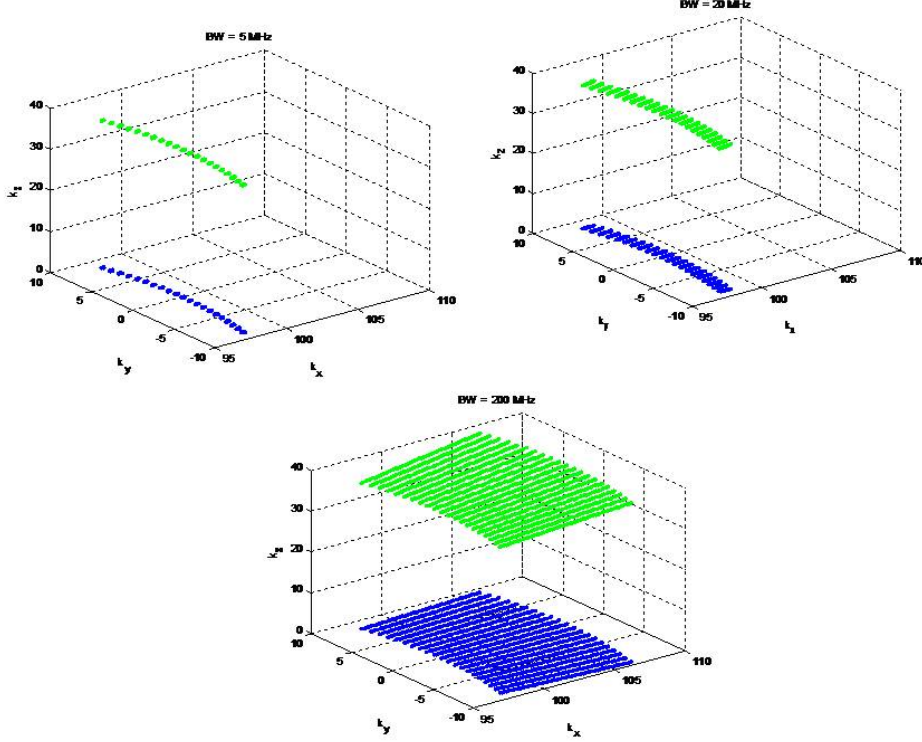
Figure 14. **Spatial frequency domain monostatic collection for 5 MHz (top left), 20 MHz (top right), and 200 MHz (bottom). The relative reduction in down-range bandwidth is significant when compared to the bandwidth of a practical SAR radar system. Green shows three-dimensional view, Blue shows two-dimensional ground projection.**

legacy SAR systems. Figure 14 shows the spatial frequency domain collection grids for a 5 MHz, 20 MHz and 200 MHz signal for a visual notion of the relative differences. Under deteriorating communication channel conditions, this bandwidth is intentionally decreased to maintain a minimum level of bit error rate (BER) [63], reducing the resolution capability for radar purposes. Furthermore, the WiMAX symbols only employ 200 of the 256 subcarriers available (the unused subcarriers are used as guard bands) reducing the already small bandwidth. The resolution of a WiMAX imaging system will then be limited, variable, and for most cases unpredictable. These limitations in bandwidth will limit the radar usefulness to large distributed targets, at least in the down-range dimension. However, as in any other spotlight SAR system, the cross-range resolution depends mainly on transmission frequency and the resulting
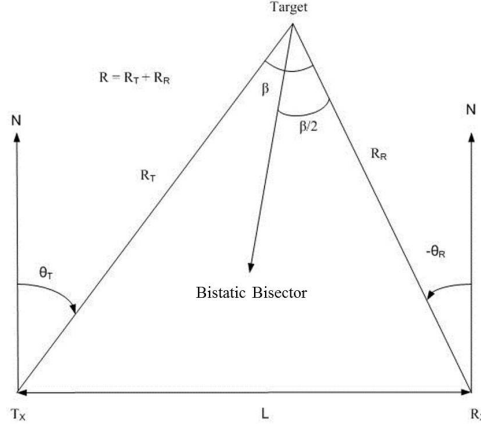
Figure 15. North-referenced bistatic geometry.

angular displacement, not on the waveform used. Flight path planning may ensure sufficient cross-range resolution to offset degraded range resolution.

Although difficult, these challenges are not impossible to overcome. The ability to use OFDM signals of opportunity for radar imaging certainly outweighs the limitations of a practical solution.

5.3 WiMAX Ambiguity Function

When considering the use of commercial waveforms for passive radar applications, bistatic is naturally implied. Monostatic ambiguity function analysis for OFDM and WiMAX waveforms have been evaluated in [23, 33, 95]. A WiMAX-based SAR system will have a stationary transmitter (cell tower) and a moving receiver. Hence, the bistatic effects on SAR range and Doppler resolution must be understood to establish collection strategies and limitations. With the exception of results being presented here and in [47], there are no other known published works on bistatic ambiguity function analysis on WiMAX.

The ambiguity function for this research incorporates bistatic geometry as defined by Tsao in [89] and briefly presented next. Using the north-referenced coordinate system shown in Figure 15 and a target located North of the bistatic baseline, the total transmission time delay proportional to the total range $R = R_R + R_T$ is defined as

$$\tau(R_R, \theta_R, L) = \frac{R_R + \sqrt{R_R^2 + L^2 + 2R_R L \sin(\theta_R)}}{c} \tag{5.3.1}$$

where R_R is the range from the target to the receiver, L is the bistatic baseline or range between receiver and transmitter, and θ_R is the angle from the North axis to the target. Assuming the transmitter and receiver are stationary, the Doppler shift is defined by [89]

$$w_D(V, \cos(\beta/2), \phi) = 2\frac{w_c}{c}V \cos(\phi) \cos(\beta/2) \tag{5.3.2}$$

where V is the target velocity vector, w_c is the carrier angular frequency, ϕ is the angle between the velocity vector and the bistatic bisector, and β is the bistatic angle. The cosine term in (5.3.2) is defined as

$$\cos(\beta/2) = \sqrt{1/2 + \frac{R_R + L \sin(\theta_R)}{2\sqrt{R_R^2 + L^2 + 2R_R L \sin(\theta_R)}}} \tag{5.3.3}$$

Further, it is shown in [89] that the target-receiver range in terms of total range R and target-receiver angle θ_R is

$$R_R = \frac{L^2 - R^2}{2R - 2L \sin(\theta_R)} \tag{5.3.4}$$

Note that for the bistatic geometry, target-receiver range R_R and in turn the associated range rate, will vary differently than for a monostatic radar system. Consequently, a target that moves in the bistatic geometry with velocity V will also

46

produce non-linear Doppler frequencies with respect to the total range R. It is clear that as the transmitter-receiver baseline distance L approaches zero, R_R approaches the monostatic range $R/2$. For these reasons, the bistatic ambiguity function only makes sense in terms of target-receiver or target-transmitter range [89]. Given the bistatic geometry described above, the bistatic ambiguity function can be defined as [89]

$$|\Psi(\cdot)| = \left| \int_{-\infty}^{\infty} s(t - \tau_a(\cdot))s^*(t - \tau_h(\cdot))e^{j(w_{Dh}(\cdot) - w_{Da}(\cdot))t} dt \right|^2 \qquad (5.3.5)$$

where the subscripts h and a represent the hypothesized and actual signal parameters. The delay τ, Doppler w_D, and the ambiguity function $|\Psi(\cdot)|$ are all functions of the bistatic geometry parameters R_R, L, and θ_R defined in (5.3.1)-(5.3.4) represented by $(\cdot)$.

The simulation of (5.3.5) properly accounts for bistatic geometries. The algorithm input is a complex signal $s(t)$ with sampling frequency f_s and duration T. A uniformly distributed set of hypothesized range and target velocity values are chosen to define the ambiguity function extent and desired resolution. Delay and Doppler values are computed using (5.3.1) and (5.3.2) and inserted in (5.3.5). Doppler effects are evaluated only on the carrier frequency.

The ambiguity function is evaluated for probable field geometries based on the advertised WiMAX signal and network properties. There are a large number of options and configurations possible; too many to represent them all. Signals with $1T_s$, $10T_s$, and $50T_s$ of duration are considered (single symbol, 10 and 50 symbols in series) along with bistatic angles greater than 120 degrees where the bistatic impact is more significant. Figures 16 and 17 show the geometries with a target-receiver range of 5km and a bistatic baseline of 10km for $\beta = 0$ degrees (monostatic) and $\beta = 126$
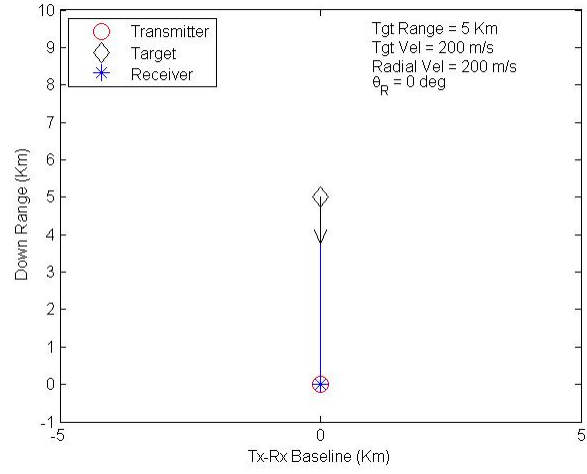
Figure 16. Monostatic geometry based on the bistatic construct, $\beta = 0$ **degrees,** $L = 0$, $\theta_R = 0$ **degrees, and** $R_R = 5$ **km.**
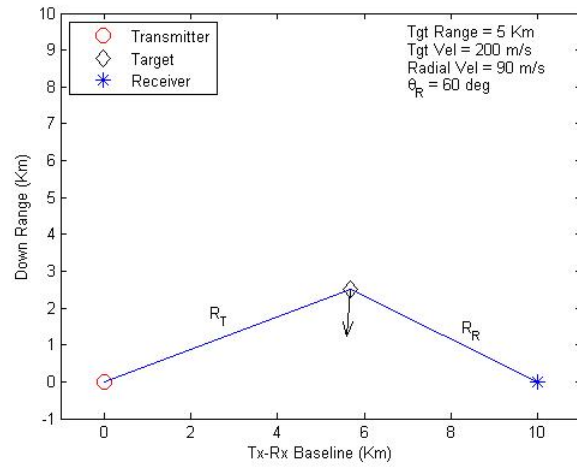
Figure 17. Bistatic geometry simulated, $\beta = 126$ **degrees,** $L = 10$ **km,** $\theta_R = 60$ **degrees, and** $R_R = 5$ **km.**

Table 4. System parameters.

Parameter	Value
WiMAX PHY	OFDM, 256 subcarriers
Bandwidth	20 MHz
Carrier Frequency	2.5 GHz
Target Range	5 km
Target Velocity	200 m/s (389 kts)

degrees respectively.

A single WiMAX DL subframe is considered for the ambiguity function evaluation. The duration of the DL depends on the number of symbols used as the reference signal, where the first two are the preambles P1 and P2. A larger number of symbols will result in a longer "pulse", improving Doppler performance. Even though an actual WiMAX transmission could transmit hundreds of symbols in a single DL, the simulation employs cases with one (only P1), 10, and 50 symbols to show the variations in Doppler performance. A 2.5 GHz carrier frequency is assumed. Tables 4 and 5 summarize the waveform parameters and system configurations for the ambiguity function analysis. For all cases, a single target is assumed at 5km range from the transmitter (R_T) with a closing velocity along the bistatic bisector of 200 m/s. The "monostatic" evaluation is based on the bistatic geometry construct with baseline $L = 0$ and $\theta_R = 0$, representing the best-case scenario.

Figures 18-20 show the monostatic ambiguity functions for WiMAX pulses containing 1 (preamble P1), 10, and 50 symbols respectively. The range resolution at half peak is approximately 7.5 meters; corresponding to the resolution of a 20 MHz pulse. Moreover, since OFDM is built using a set of single frequency carriers, the range domain peak correctly resembles the ambiguity function of a rectangular pulse.

Table 5. Ambiguity function cases evaluated.

Configuration	β (degrees)	# of symbols
Monostatic	0	1
Monostatic	0	10
Monostatic	0	50
Bistatic	126	50
Bistatic	160	50
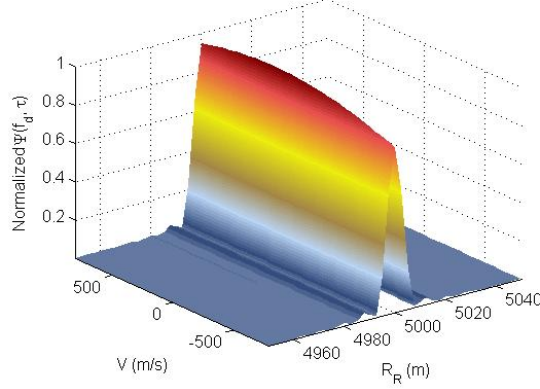
Figure 18. WiMAX monostatic ambiguity function, $R_R = 5$ km, one symbol (P1).

Clearly the more symbols used, the better Doppler resolution is obtained as can be noted by comparing the single symbol case with the multiple symbols cases. Sequential symbols will carry unique data, creating a *pseudo random*-like pulse, maintaining the range resolution of a single symbol.

The ambiguity function for bistatic angles of 126 and 160 degrees are shown in Figures 21 and 22 respectively. For the wide bistatic angle of $\beta = 126$ degrees, the ambiguity function shows a range resolution of approximately twice the monostatic case. When considering a bistatic SAR system, this would be a reasonable limit to the collection geometry for large distributed targets (building, airfields, etc.). Higher values will significantly degrade the range and performance of the wave as can be seen in Figure 22 ($\beta = 160$ degrees) where now the range resolution is practically
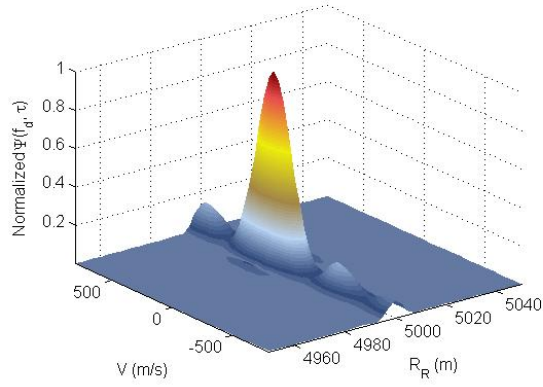
Figure 19. WiMAX monostatic ambiguity function, $R_R = 5$ km, 10 symbols.
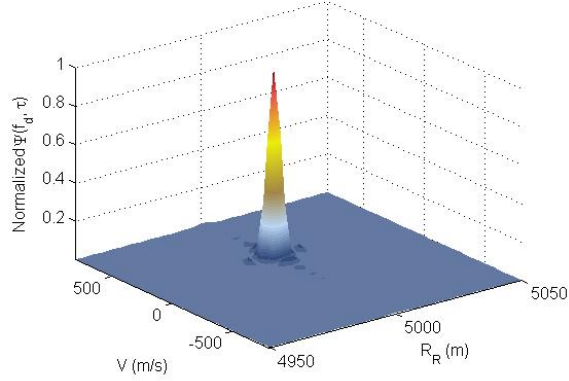
Figure 20. WiMAX monostatic ambiguity function, $R_R = 5$ km, 50 symbols.

unusable for any kind of SAR product. Despite the degradation in range resolution performance, the Doppler performance suffers less degradation with the increase in bistatic angles. If necessary, a larger number of symbols can be used in the radar processing to improve Doppler performance under extreme bistatic conditions.
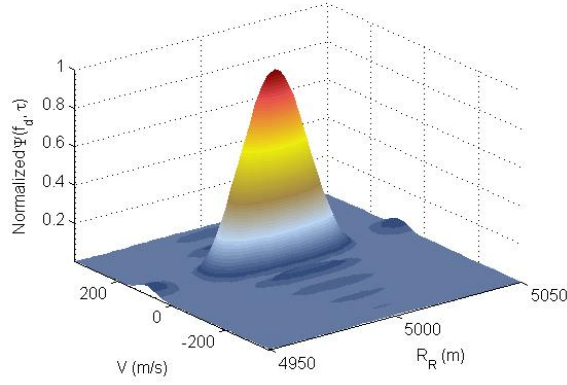
Figure 21. WiMAX bistatic ambiguity function, $\beta = 126$ degrees ($\theta_R = 60$ degrees), $R_R = 5$ km, 50 symbols.
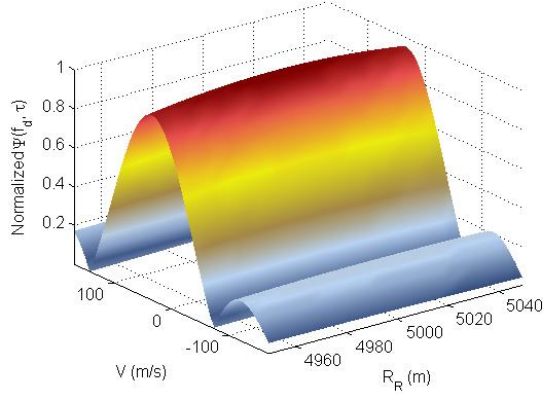
Figure 22. WiMAX bistatic ambiguity function, $\beta = 160$ degrees ($\theta_R = 80$ degrees), $R_R = 5$ km, 50 symbols.

5.4 The WiMAX Collection Model

As a signal of opportunity, WiMAX is outside the control of the airborne radar operator. The only user-controllable parameters are platform flight path and velocity during a collection run. As such, the airborne collection of WiMAX ground returns requires careful planning. In this section, the WiMAX network infrastructure is defined within a bistatic radar construct. One of the most salient difference from other airborne bistatic systems is that the transmitter will always be fixed (in ground networks) and the angle of incidence upon the illuminated scene will always be constant.
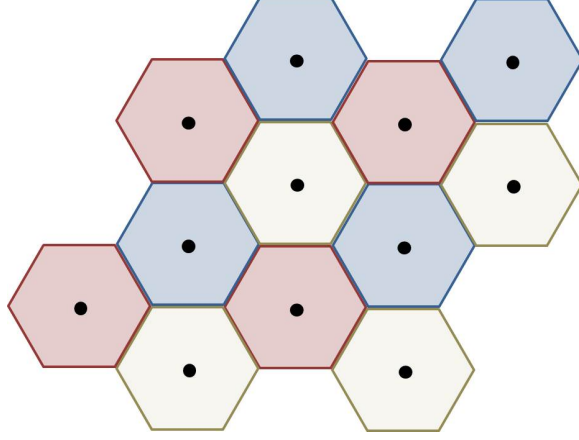
Figure 23. Typical cellular configuration. Black circles represent transmitter; same-color cells re-use the same frequency bands.
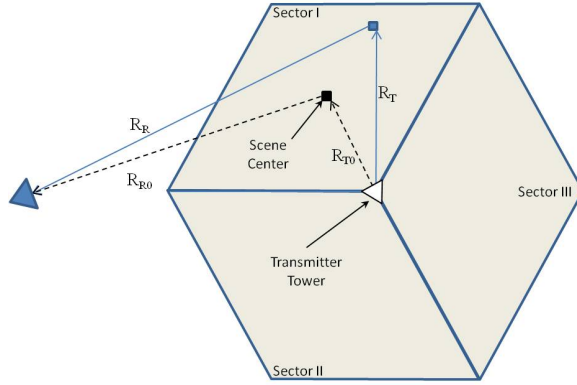
Figure 24. WiMAX bistatic scenario, top view [51].

To evaluate and design passive WiMAX collection approaches, one needs to understand the key parameters which will impact the final SAR image product such as bistatic range and SNR contours, bistatic resolutions, and Doppler ambiguities.

WiMAX ground networks are designed using the concepts used for cellular ground network designs. Figure 23 shows a typical cellular configuration over a geographical area (top view). The black dots between the cells represent a transmission tower and each honeycomb shape a *cell* [1]. Typical cell radius can range from 1 to 30 kilometers [32]. Each transmission tower will usually have three or more *sectors* providing

---

[1]In reality, the cell shapes will be irregular; overlapping slightly over the other adjacent cells.

coverage over the entire cell. An radio frequency (RF) engineer designs the number of transmission towers, the number of sectors, and the transmission bands of each based on propagation models, digital maps, and site signal-strength surveys [32]. Note that cells with similar colors may be assigned the same frequencies [2]. However, they will each carry their own ID code and will independently serve the customers within their particular sectors [32].

For this study, three 120-degree sectors per cell are assumed. As such, consider a single sector to be the illuminated area of interest. Figure 24 shows the WiMAX spotlight SAR concept where R_{T0} is the range from the transmitter to the center of the sector, R_{R0} is the range from the receiver to the center of the sector, R_T is the range from the transmitter to the mth scatterer in the sector, and R_R is the range from the mth scatterer to the receiver. If a receiver beam covers the complete sector, then it is assumed that all the returns from such sector can be processed into a spatial reflectivity map (a SAR image).

Figure 25 shows the general collection model for the illumination of a single sector where A_T is the area illuminated by the transmitter and A_R is the area illuminated by the receiver. During a *spotlight* mode collection run, the receiver is turned "ON" at a time t_a, and turned "OFF" at time t_b. During this period, P complete DL ground returns are collected (based on the transmitter's PRF) from a single WiMAX sector and stored for processing. Interference from neighboring sectors is assumed negligible through WiMAX network design [28]. The transmitter frequency and transmitter position are assumed known per publicly available data. It is also assumed that the

---

However due to frequency diversity, the interference from the adjacent cells can be considered negligible [32].

[2]A concept known as *frequency re-use.*
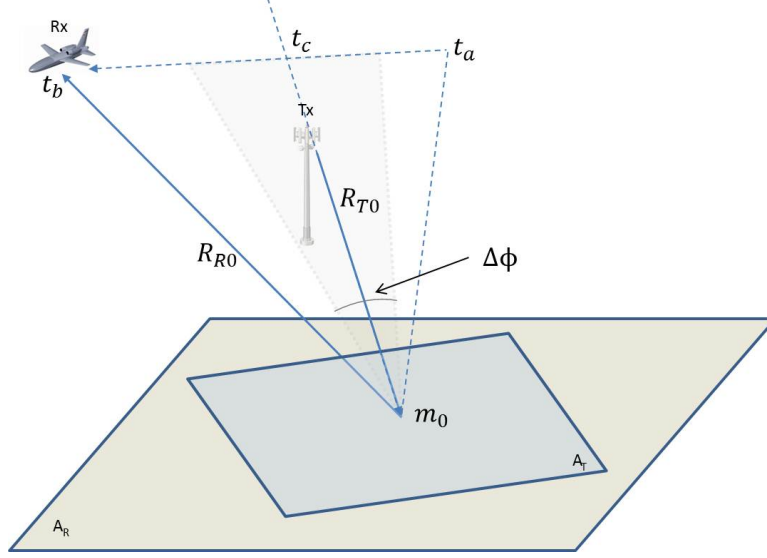
Figure 25. General WiMAX collection model. The transmitter illuminates area A_T and the receiver illuminates the area A_R. The collection begins at time t_a and ends at time t_b resulting in a bistatic azimuth displacement of $\Delta\phi$. The bistatic center of the collection occurs at time t_c [51].

communication data d_n is either known a-priori (in the case of the preambles) or perfectly obtained using a communications receiver .

The center m_0 of the scene A_T is commonly known as the motion compensation point (MOCOMP) and is used in the spotlight mode SAR process as a common reference to align all the pulses in phase. For this analysis, m_0 is defined by coordinates (0,0) in terms of down-range and cross-range respectively. The bistatic down-range is defined along the bistatic LOS vector at the center of the collection. As shown, down-range is along the line between the WiMAX transmitter and m_0, where t_c is the time at the collection center ($\phi = 0$). Nevertheless, the following signal processing design applies to any general bistatic configuration.

Ignoring any time dependencies at this point, the total range R_0 through the

center of the cell A_T is determined by

$$R_0 = R_{T0} + R_{R0} \tag{5.4.1}$$

and the total range through a scatterer is

$$R_m = R_T + R_R. \tag{5.4.2}$$

Note that relative to the center of A_T, the received signal phase Φ associated with target m is proportional to the difference in range R_m with respect to R_0. It follows that:

$$
\begin{aligned}
\Delta\Phi_m &= k\Delta R_m \\
&= k(R_0 - R_m) \\
&= k(R_{T0} - R_T + R_{R0} - R_R)
\end{aligned}
\tag{5.4.3}
$$

where k is a spatial frequency variable defined by $k = \omega/c$, ω is temporal frequency in radians per second and c is the speed of light.

Rigling defines the phase history model as [78, 98]

$$S(f_n, t_p) = \sum_m A_m e^{\Phi_m(f_n, t_p)} + \mathrm{w}(f_n, t_p) \tag{5.4.4}$$

where $S(f_n, t_p)$ is the phase history for the nth spatial frequency f_n and pth pulse, t_p is the transmission instant of the pth pulse, A_m is the reflectivity value of the mth scatterer, Φ_m is the phase of the return signal relative to the phase of the scene center, and w is additive white Gaussian noise. The relative bistatic phase function

56

Φ is modeled as

$$\Phi_m(f_n, t_p) = -2\pi j f_n \frac{\Delta R_m(t_p)}{c} \tag{5.4.5}$$

where ΔR is described in (5.4.3) above. Rigling approximates the variable ΔR_m using a first-order Taylor series expansion leading to [98]

$$
\begin{aligned}
\Delta R_m(t_p) = &-x_m[\cos\phi_T(t_p)\cos\theta_T(t_p) + \cos\phi_R(t_p)\cos\theta_R(t_p)] \\
&- y_m[\sin\phi_T(t_p)\cos\theta_T(t_p) + \sin\phi_R(t_p)\cos\theta_R(t_p)] \\
&- z_m[\sin\theta_T(t_p) + \sin\theta_R(t_p)]
\end{aligned}
\tag{5.4.6}
$$

where x_m, y_m, and z_m are the cartesian coordinates of the mth scatterer relative to the scene center. Note that for the WiMAX configuration, (5.4.6) can be rewritten as

$$
\begin{aligned}
\Delta R_m(t_p) = &-x_m[\cos\phi_T\cos\theta_T + \cos\phi_R(t_p)\cos\theta_R(t_p)] \\
&- y_m[\sin\phi_T\cos\theta_T + \sin\phi_R(t_p)\cos\theta_R(t_p)] \\
&- z_m[\sin\theta_T + \sin\theta_R(t_p)]
\end{aligned}
\tag{5.4.7}
$$

where the transmitter T terms are assumed known a priori and constant during the entire collection. In (5.4.6), a small scene relative to the platform ranges is assumed, leading to a far-field approximation.

The far field approximation can introduce phase errors when using the polar formatting algorithm (PFA) for image reconstruction. The second-order Taylor series expansion terms are comprised of constant, linear, and quadratic functions of the slow time t_p. The constant and linear terms will introduce spatially dependent geometric distortion in the final image (incorrect target position) [98]; however these are correctable by creating a spatial correction function based on the known bistatic

geometry. The second order terms will introduce phase errors, creating de-focusing effects on targets far from the scene center. The defocusing error at the center frequency due to range curvature is

$$\Phi_e = \frac{2\pi f_c}{c}\left(\frac{x^2 y_T^2}{2R_T^3} + \frac{x^2 y_R^2}{2R_R^3}\right) \tag{5.4.8}$$

Limiting the phase error to $\pi/2$ (generally considered "acceptable") and expressing target locations in terms of aperture and cross-range extents leads to the maximum radius of an image scene [98]

$$r_{max} < \frac{\sqrt{2\lambda_0}}{\sqrt{\frac{L_T^2}{R_T^3} + \frac{L_R^2}{R_R^3}}} \tag{5.4.9}$$

where L_T and L_R are the straight line distance of the transmitter and receiver respectively, R_T and R_R are the transmitter and receiver ranges to scene center, and λ_0 is the center frequency wavelength. Note that for a WiMAX scenario, $L_T = 0$, reducing (5.4.9) to

$$r_{max} < \sqrt{\frac{2\lambda_0}{L_R^2/R_R^3}}. \tag{5.4.10}$$

As an example, consider a receiver at 10 km from the scene center with an aperture distance of 100 meters and a transmitter frequency of 2.5 GHz. The maximum imaging radius (in meters) using PFA would be

$$r_{max} < \sqrt{\frac{2(0.12)}{100^2/10000^3}} = 4900 \text{ m.} \tag{5.4.11}$$

Since the typical cell sizes can be in the order of 1km to 30km, the use of PFA would be a practical solution to the inverse problem if the geometrical errors introduced by the constant and linear terms of the second-order approximation can be properly
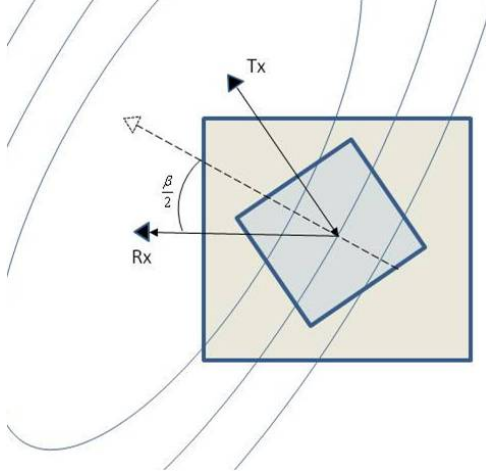
Figure 26. Two-dimensional overlay of bistatic isorange regions on a target scene.

corrected.

Isorange Contours.

Recall from Chapter II that the total range in a bistatic geometry results in isorange contours represented by ellipses with the transmitter and receiver at their foci locations. For R_T and R_R much greater than the scene radius, constant range lines will be oriented perpendicular to the bisector of the bistatic angle β. Figure 26 shows a two-dimensional overlay of the oval regions on the target scene. The dashed line represents the resultant *virtual* LOS. This virtual radar is equivalent to a monostatic SAR system where down-range cells are uniformly spaced. As such, the returned waveform transduces integrated reflectivities along these constant oval range contours [57, 78]. Under ideal circumstances, the illuminated scene radius will be much smaller than the transmitter and receiver ranges. In such cases, the isorange lines will appear to be straight across the scene. However, this is not necessarily the WiMAX scenario. When considering a broadband network, the illuminated area will be "close" to the transmitter, probably much closer than a covert airborne receiver.
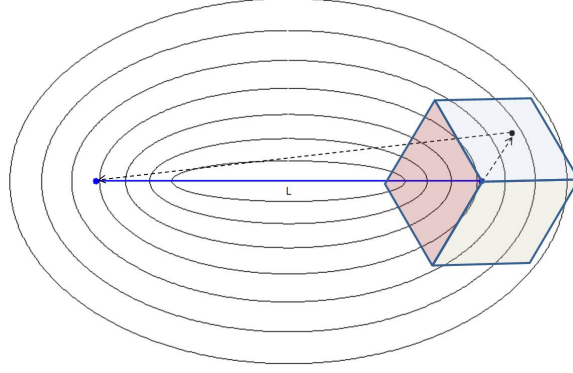
Figure 27. Bistatic constant range contours over WiMAX sectors. $\beta < 90$ **degrees.**
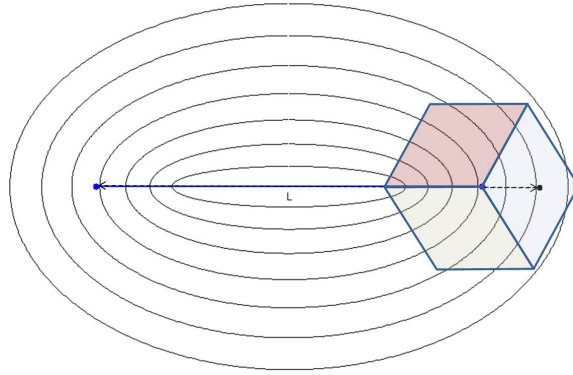
Figure 28. Bistatic constant range contours over WiMAX sectors. $\beta = 0$ **degrees.**

The far range assumption breaks down and the quadratic nature of the isorange lines is not negligible. To illustrate the idea, consider Figures 27-29. The isorange contours are indeed quadratic and the impact of the quadratic distortion appears to loose symmetry towards the larger bistatic angles (at $\beta = 90$ degrees) aggravating monostatic correction techniques like the ones described in [27].

Bistatic Signal-to-Noise Ratio (SNR) contours.

Another consideration lies with the constant range power lines defined by the ovals of Cassini (Refer to Chapter II). Figure 30 shows the maximum range contours over the illuminated region at $\beta < 90$ degrees. Note that the higher SNR region is
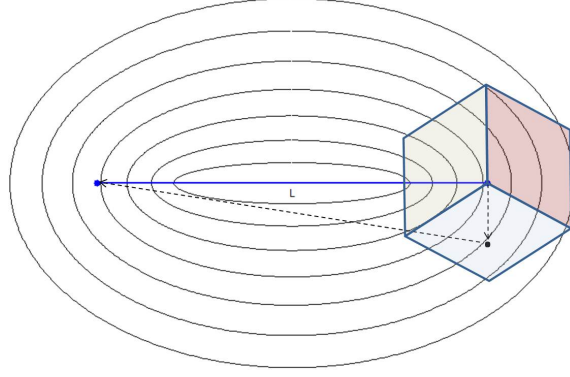
Figure 29. Bistatic constant range contours over WiMAX sectors. $\beta = 90$ **degrees.**
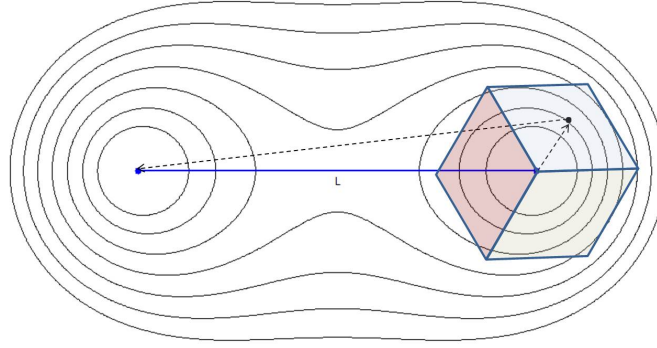
Figure 30. Bistatic constant SNR lines over WiMAX sectors. $\beta < 90$ **degrees.**

concentrated around the transmitter; an ideal situation for the WiMAX scenario.

Some noteworthy considerations emerge based on the general bistatic discussion herein. First, as for any arbitrary bistatic SAR system, it becomes clear that a non-linear spatially dependent geometric correction model is required for proper SAR image reconstruction. Second, there may be a "best collection" strategy considering the impact of non-linear terms in phase histories and the maximum scene radius attainable using PFA. Lastly, note that under ideal conditions, the range from the transmitter to the scene will remain constant throughout the collection process with some antenna motion errors.

Bistatic Resolution.

A well known bistatic nuisance is the impact of bistatic angles on image resolution. The WiMAX collections geometry will naturally lead to bistatic configurations. Using Rigling's approach to bistatic SAR [98], the phase term in (5.4.7) can be expressed in terms of the spatial frequency f and slow time variable t_p as

$$\frac{2\pi}{c}[x_m f_x(f, t_p) + y_m f_y(f, t_p) + z_m f_z(f, t_p)] \tag{5.4.12}$$

where x_m, y_m, and z_m are the three-dimensional coordinates of the scatterer with respect to the scene center, and f_x, f_y, and f_z are the spatial frequency components in the x, y, and z axes defined by

$$
\begin{aligned}
f_x(f, t_p) &= f[\cos\theta_T + \cos\phi_R(t_p)\cos\theta_R(t_p)] \\
f_y(f, t_p) &= f[\sin\phi_R(t_p)\cos\theta_R(t_p)] \\
f_z(f, t_p) &= f[\sin\theta_T + \sin\theta_R(t_p)]
\end{aligned}
\tag{5.4.13}
$$

where θ_T and θ_R are the transmitter and receiver elevation angles and ϕ_T and ϕ_R are the transmitter and receiver azimuth angle with respect to the central azimuth of the collection. Using (5.4.13), an approximate bistatic look angle can be defined in azimuth and elevation as the principal values of [98]

$$\phi_b = \tan^{-1}\left[\frac{f_y(f, 0)}{f_x(f, 0)}\right] \tag{5.4.14}$$

$$\theta_b = \tan^{-1}\frac{f_z(f, 0)}{\sqrt{f_x^2(f, 0) + f_y^2(f, 0)}} \tag{5.4.15}$$

where $t_p = 0$ defines the center of the collection interval. The bistatic range direction

is defined in terms of (5.4.14) and (5.4.15) by the vector

$$\vec{r}(0) = [\cos\phi_b \cos\theta_b, \sin\phi_b \cos\theta_b, sin\theta_b] \tag{5.4.16}$$

and the cosine of the bistatic angle can be determined by

$$\cos\beta = \frac{(\vec{r}_T)^T(0)\vec{r}_R(0))}{||\vec{r}_T(0)||\,||\vec{r}_R(0)||} \tag{5.4.17}$$

where $\vec{r}_T(0)$ and $\vec{r}_R(0)$ are the transmitter and receiver LOS vectors to the center of the scene. Using the aforementioned bistatic model, the down-range (y) and cross-range (x) resolutions are defined by [98]

$$\rho_y = \frac{c}{2B\cos(\beta/2)} \tag{5.4.18}$$

$$\rho_x = \frac{c}{4f_0 \sin(\Delta\phi/2)\cos\theta_b \cos(\beta/2)} \tag{5.4.19}$$

where B is the WiMAX signal bandwidth, β is the bistatic angle at the center of the collection, f_0 is the carrier frequency, θ_b is the bistatic elevation angle, and $\Delta\phi$ is the bistatic azimuth span of the collection. From the above equations it becomes clear that the best down-range resolution is obtained when $\beta = 0$ while the best cross-range resolution is achieved when $\beta = 0$ and $\theta_b = 0$. Since the transmitter is fixed, it follows that the optimal collection strategy for best resolution will be achieved by positioning the receiver at the transmitter's elevation angle (with respect to the scene center) with an azimuth path coincident with the center of the illuminated scene as shown in Figure 25. Although this flight path is easily achievable with proper planning, other factors might impede its execution (terrain, obstacles, electromagnetic interference, etc.).

Doppler Bandwidth.

Another important consideration when designing SAR collection strategies for a WiMAX-based system is the relation of the Doppler bandwidth B_d to the WiMAX frame rate or pulse repetition frequency (PRF). In a monostatic SAR system, the PRF is set to account for the maximum Doppler observed during the collection where the condition

$$\text{PRF} \geq B_d. \tag{5.4.20}$$

must be met to avoid aliasing in the cross-range domain [86]. When using passive sources such as WiMAX, the PRF (which is equivalent to the WiMAX DL frame rate) is outside the operator control. However, the operator can control the extent of Doppler frequencies observed by establishing proper LOS velocities and bistatic angles during the collection. In [98], Rigling defines the total observed Doppler bandwidth for the bistatic SAR collection as the sum of the *along-track Doppler bandwidth* $B_d^{(1)}$ (a single scatterer at scene center) and the *spotlighted Doppler bandwidth* $B_d^{(2)}$ (range of Doppler from all scatterers)

$$B_d = B_d^{(1)} + B_d^{(2)} \tag{5.4.21}$$

For Doppler purposes, the WiMAX pulse can be assumed narrowband where Doppler is observed only on the carrier frequency. Following the along-track Doppler definition, the frequency shift observed at the receiver at slow time t_p from a point scatterer at the scene center is given by [98]

$$f_d^{(1)} = -\frac{1}{\lambda_c} \frac{\partial(R_R(t_p) + R_T(t_p))}{\partial t_p} \tag{5.4.22}$$
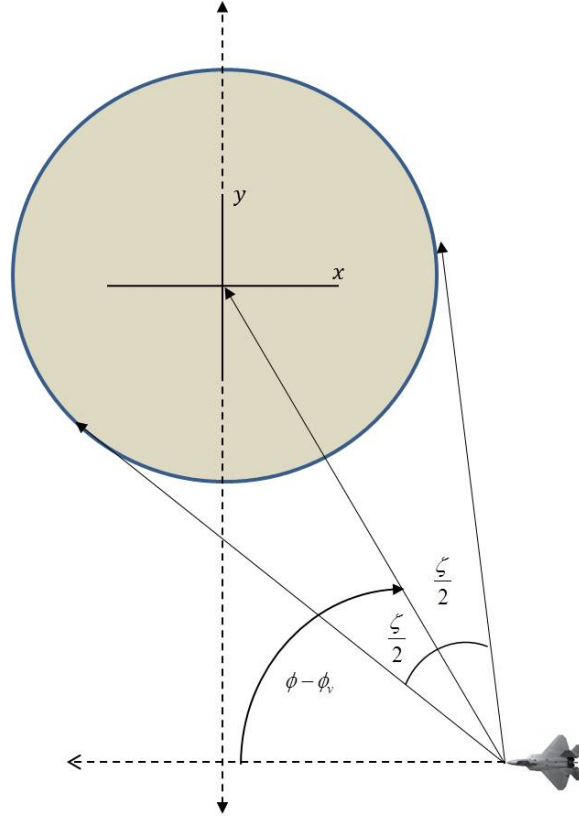
Figure 31. Azimuth definitions for spotlighted Doppler bandwidth.

which for the WiMAX case, the fixed transmitter condition results in

$$f_d^{(1)} = -\frac{1}{\lambda_c} \left[\frac{x_R(t_p)v_x + y_R(t_p)v_y + z_R(t_p)v_z}{\sqrt{x_R^2(t_p) + y_R^2(t_p) + z_R^2(t_p)}} \right].$$

(5.4.23)

The along-track bandwidth will be the difference between the maximum and the minimum Doppler frequencies observed during the collection period T_c

$$B_d^{(1)} = \max_{t_p} f_d^{(1)}(t_p) - \min_{t_p} f_d^{(1)}(t_p).$$

(5.4.24)

The spotlighted Doppler bandwidth is the range of Doppler frequencies observed from all scatterers in the scene by the receiver. These Doppler frequencies can be

65

determined by [98]

$$f_d^{(2)} = \frac{v \cos(\phi - \phi_v \pm \zeta/2) \cos(\theta)}{\lambda_c} \qquad (5.4.25)$$

where θ is the receiver's depression angle to the scene center, ϕ is the azimuth to the center of the collection, ζ is the antenna field of view (FOV), and $\phi - \phi_v$ is the angle separating the LOS to the origin and the receiver velocity vector as shown in Figure 31 [98]. Assuming no change in elevation during the collection, the spotlighted Doppler bandwidth due to receiver's movement is then

$$B_d^{(2)} = \frac{2}{\lambda_c} \left[v_y \cos(\phi_R) \sin(\zeta_R/2) \cos(\theta_R) - v_x \sin(\phi_R) \sin(\zeta_R/2) \cos(\theta_R) \right]. \qquad (5.4.26)$$

Rearranging terms yields

$$B_d^{(2)} = \frac{2 \sin(\zeta_R/2) \cos(\theta_R)}{\lambda_c} \left[v_y \cos(\phi_R) - v_x \sin(\phi_R) \right]. \qquad (5.4.27)$$

Note that using (5.4.27), the operator is capable of controlling the extent of Doppler frequencies observed through the velocity and bistatic angle parameters.

The final item of consideration is the cross-range sample intervals and cross-range scene extent. Realizing that the PRF is defined by the WiMAX system, the collection platform can only adjust its velocity to achieve the required sampling parameters. The DL interval will determine the amount of pulses P within the desired azimuth span which ultimately defines the scene cross-range extent.

Consider Figure 32. Without loss of generality, assume a pulse is transmitted at time t_1 from the center of the scene (transmitter tower is fixed) at a stable PRF. The collection platform is assumed stationary during the signal travel time to the platform. At time t_1, the receiver is located at position $\vec{p}_1 = [x_1, y_1, z_1]$. Furthermore, assume
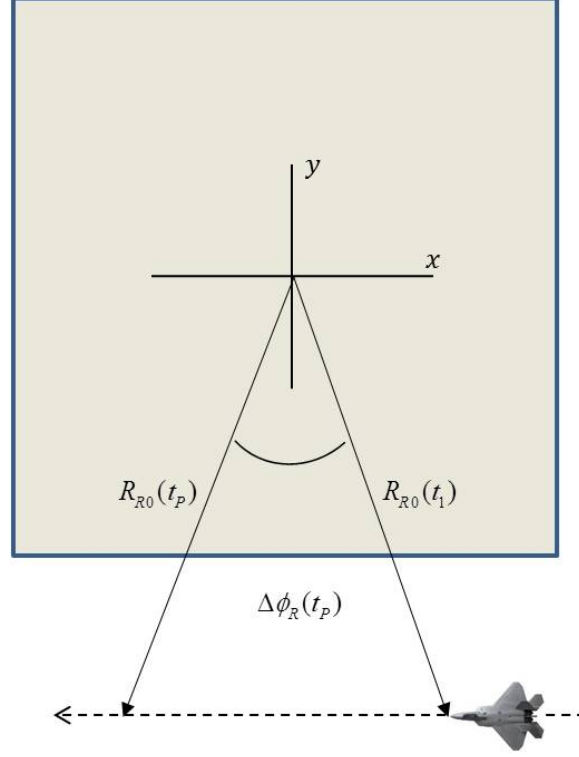
Figure 32. Sample collection interval.

the collection platform maintains a straight flight trajectory with constant velocity $\vec{v}_R = [v_x, v_y, v_z]$. At time t_P, the receiver intercepts the last pulse of the collection at a certain differential receiver azimuth $\Delta\phi_R(t_1)$. The amount of samples collected is simply determined by using the PRF and the collection time interval $T_c = t_P - t_1$

$$P = \text{PRF} \times T_c. \tag{5.4.28}$$

To evaluate the feasibility of a real WiMAX passive SAR system, a hypothetical example using typical WiMAX network parameters is presented next. A WiMAX system will operate at a frame rate of 200Hz using a carrier frequency of 2.4 Ghz ($\lambda = 0.13$ m). Assume the bistatic collection geometry depicted in Figure 33 with a velocity vector of $\vec{v}_R = [100, 0, 0]$ m/s (about 195 knots in the cross-range dimension) and an elevation of 1500 meters (4921 feet). The receiver antenna beamwidth (ζ)
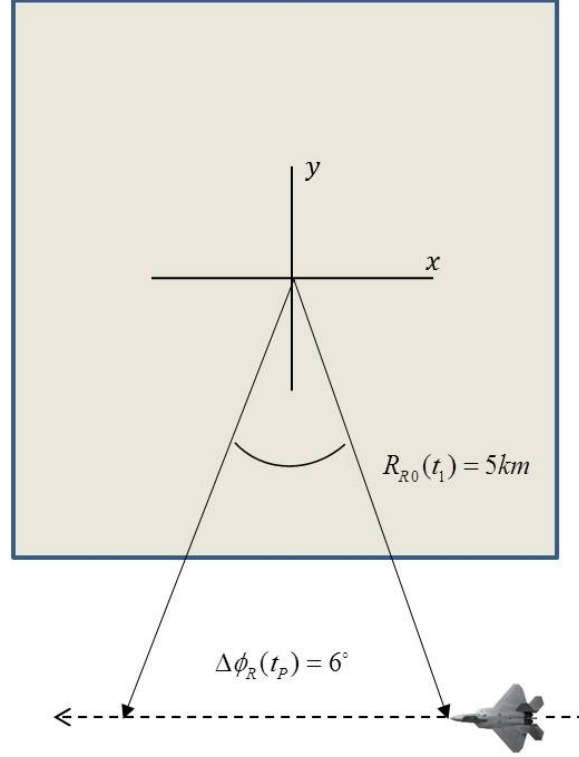
Figure 33. Collection example.

is assumed to be 11 degrees in azimuth. By symmetry, the along track Doppler is calculated as

$$B_d^{(1)} = 2 \max_{t_p} f_d^{(1)}(t_p) \tag{5.4.29}$$

where the maximum and minimum values are found at the beginning and end of the collection. Using (5.4.23) in (5.4.29)

$$B_d^{(1)} = \frac{2}{0.13 \text{ m}} \left[\frac{(261 \text{ m})(100 \text{ m/s}) + 0 + 0}{5000 \text{ m}} \right] \approx 80 \text{ Hz.} \tag{5.4.30}$$

Using (5.4.27), the spotlighted Doppler is

$$B_d^{(2)} = \frac{2\sin(5.5°)\cos(16°)}{0.13 \text{ m}} [0 - (100 \text{ m/s})\sin(3°)] \approx -7 \text{ Hz} \tag{5.4.31}$$

68

producing an observed Doppler bandwidth of

$$B_d^{(1)} + B_d^{(2)} = 73 \text{ Hz}. \tag{5.4.32}$$

Note that as required, the system PRF of 200 Hz will be larger than the observed Doppler, eliminating aliasing in the cross-range domain. The number of DL pulses collected would be

$$\text{pulses collected} = \frac{(200 \text{ Hz})(260 \text{ m})}{100 \text{ m/s}} = 520 \tag{5.4.33}$$

which at a cross-range resolution of 1.4 m produces a cross-range extent of 728 meters.

It is easy to see how the selection of receiver trajectory and velocity are key parameters of the desired passive SAR image product. The example results show that a real system implementation is reasonable within the pre-established assumptions. However, there are additional elements which were not considered here that would be critical to a real implementation. For example, the return signal strength at the receiver antenna must have an adequate SNR. It is clear that careful pre-collection planning becomes critical to ensure adequate imaging properties.

5.5   SAR Digital Signal Processing

Before obtaining phase histories, the processor must prepare the received data to allow proper range compression. As discussed in Section 5.2, when using time division duplexing (TDD), the WiMAX base station transmits a series of DL subframes. Network users transmit UL subframes between the DL transmissions. The UL subframes are assumed to have just enough power to propagate within the service sector and

69
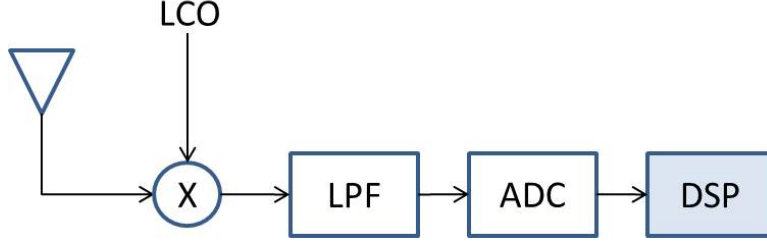
Figure 34. Basic receiver front end. After the antenna, the signal is down-converted to baseband, low-pass filtered and sampled digitally at the ADC before digital processing.

should not reach the airborne receiver. This transmission scheme parallels that of a pulse SAR radar system and is the underlying assumption of the collection and signal processing approach. This section introduces the proposed signal processing leading discretized received returns to a two-dimensional phase history array [51].

Figure 34 shows a general radar receiver block diagram. The received analog returns are down-converted to baseband through the local control oscillator (LCO) carrier, low-pass filtered (LPF), and sampled by a analog-to-digital converter (ADC) before the digital signal processor (DSP). During the collection, the DSP stores the incoming samples in a one-dimensional array. After the desired collection path is complete, the data is converted to a two-dimensional array in the *fast time* and *slow time* dimensions using known or estimated WiMAX transmission parameters.

When considering bistatic SAR, one of the commonly known challenges is the correct timing or synchronization between transmitter and receiver for proper compensation with respect to the scene center point m_0. Failure to synchronize the transmitter and the receiver in a bistatic SAR system hinders the correct reconstruction of SAR imagery by destroying phase coherence in the phase history array. There are some key aspects of the WiMAX network that offer some advantages in this area. First, the WiMAX transmitter is fixed and its position can be accurately known a-
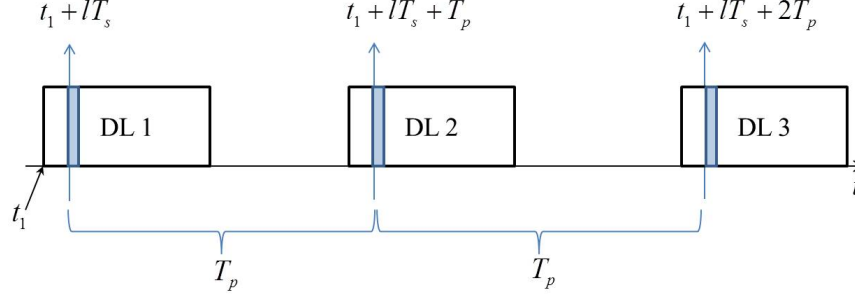
Figure 35. Timing of the transmission of three DL subframes ($P = 3$). Shaded area represents the $(l+1)$th symbol in each DL.

priori. Having a non-moving transmitter eliminates the need to continuously estimate the transmitter-m_0 range for every pulse simplifying the dependance of the relative signal path delay to the position estimate of the receiver only. Second, the WiMAX network will typically have a predefined frame rate; that is, the frame rate (or PRF) can be precisely estimated based on the allowable values defined by the standard. Using these key facts, a practical signal processing approach to the passive WiMAX SAR scenario is developed.

Figure 35 shows the transmission of three complete DL subframes. The shaded area in each DL represents a single symbol in time domain. The first DL is transmitted at time t_1 and its $(l+1)$th symbol is transmitted at time $t_1 + lT_s$. Note that under a constant and stable frame rate, the same symbol position in the $(p+1)$th DL is transmitted at $t_1 + lT_s + pT_p$ where T_p is the known duration of a complete WiMAX frame (DL and UL). Assuming a constant frame rate and the knowledge of t_1, the transmission instant of any symbol in any DL can be determined.

The transmission timing concept is applied to a SAR collection from an airborne platform. Figure 36 shows a notional data collection between times t_a and t_b. Different from the transmission scheme, each block now represents the combined DL

71
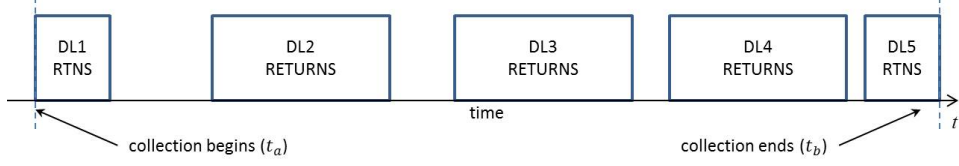
Figure 36. Notional airborne collection. DL returns 1 and 5 at each end are only partially complete while returns 2, 3, and 4 include all the transmitted symbols from their respective DLs. The decreasing spacing represents the decreasing platform range to the center of the scene.

returns from all the scatterers in the scene shifted in time by their associated path delays. Note that the spacing between returns will depend on the frame rate and the bistatic range $R_{R0} + R_{T0}$, where R_{T0} is constant. This behavior is exaggerated in Figure 36 which represents an airborne platform which is getting closer to the $\phi = 0$ azimuth point. The return timing can be exploited using a transmission reference time corrected for range. Let t_r be the reference time at *any* point before the first complete DL return (any point between returns DL1 and DL2 in Figure 36). Then the same relative point for the $(p+1)$th DL return can be determined by

$$t_{(p+1)} = t_r + pT_p - \frac{\Delta R_{R0}}{c} \tag{5.5.1}$$

where ΔR_{R0} is the change in receiver range between times t_r and $t_r + pT_p$. The utility of this timing approach is that the entire collection can now be partitioned into P returns, each collected from a particular bistatic azimuth. Knowledge of the returns starting time leads to knowledge of their relative starting phase. Note that the absolute starting phase does not need to be estimated; a constant phase bias error across all returns will have no effect on the SAR image, hence any bias in the initial phase estimate will not impact the quality of the final SAR product.

Having partitioned the collection into slow-time bins, one can define *segments* of arbitrary length for processing, each encompassing a complete or partial portion of a
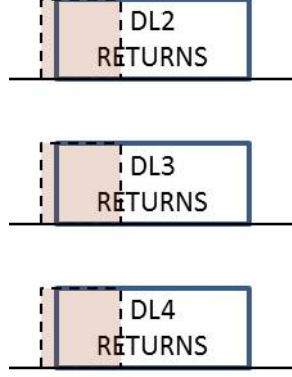
Figure 37. After the collection is partitioned into individual DL returns, processing segments (shaded areas) are defined to include the desired symbols for signal processing. Example shown guarantees the inclusion of the preambles. The length of the segment will impact the number of symbols used in the phase history process.

single DL return. The length of each segment is user defined and can be adjusted to include one or more symbols. The starting phase of each segment can be estimated and used to achieve phase coherence. The concept of return segments is presented in Figure 37 where a particular example is shown. Each segment is used to create one-dimensional phase histories along the resulting bistatic LOS.

It is important to note that in a return segment, there are an infinite amount of copies of the time-domain symbols based on the scattering properties of the scene. One can only approximate the location of the particular symbol(s) to be processed and define a segment wide enough to encompass most of its (their) return energy. The location of the symbols can be approximated by detecting the beginning of the DL return (using an envelope detector for example) and using the symbol duration T_s.

Based on the aforementioned timing concept and the WiMAX return model in [50], the return associated with a single point target at m_0 is described by

$$s_{r0}(t) = \sum_{p=0}^{P-1}\sum_{l=0}^{L-1} g(0)e^{j\omega_0(t-t_T-\tau_{0p}-lT_s-pT_p)} \sum_{n=-N/2}^{N/2-1} d_{p,l,n}e^{jn\Delta\omega(t-t_T-\tau_{0p}-lT_s-pT_p)} \quad (5.5.2)$$

73

where $g(0)$ is the complex reflectivity of the scatterer, L is the total number of symbols in the DL subframe, P is the number of frames in the collection, and τ_{0p} is the delay associated with the scene center for frame p. The variable t_T defines the first sample from the first DL return in the collection. Using envelope detectors, one can estimate t_T and discard any "left over" energy captured from any prior and incomplete DL. In this sense, the estimation of t_T becomes the pivot for symbol extraction and phase coherence among the processing segments. Letting $t' = t - t_T$, (5.5.2) can be rewritten as

$$s_{r0}(t') = \sum_{p=0}^{P-1} \sum_{l=0}^{L-1} g(0) e^{j\omega_0(t'-\tau_{0p}-lT_s-pT_p)} \sum_{n=-N/2}^{N/2-1} d_{p,l,n} e^{jn\Delta\omega(t'-\tau_{0p}-lT_s-pT_p)} \qquad (5.5.3)$$

In a real scenario, there will be an infinite amount of scatterers in the illuminated scene. The total return is a superposition of all the returns from all scatterers and is represented by

$$s_{r0}(t') = \sum_{p=0}^{P-1} \sum_{l=0}^{L-1} \int_{u_a'}^{u_b'} g(u') e^{j\omega_0(t'-\tau_{0p}-\tau_u'-lT_s-pT_p)} \sum_{n=-N/2}^{N/2-1} d_{p,l,n} e^{jn\Delta\omega(t'-\tau_{0p}-\tau_u'-lT_s-pT_p)} du'$$

$$(5.5.4)$$

where u' is the differential bistatic slant range with respect to the range $R_{T0} + R_{R0}$, $g(u')$ is the scene reflectivity density function (the limits u_a' and u_b' represent the differential ranges to the near and far scene limits respectively), and τ_u' is the delay associated with the differential bistatic slant range u'. It can be shown that after down conversion and filtering the signal becomes [49]

$$s_r(t') = \sum_{p=0}^{P-1} \sum_{l=0}^{L-1} \int_{u_a'}^{u_b'} g(u') e^{-j\omega_0(\tau_u'+lT_s+pT_p)} \sum_{n=-N/2}^{N/2-1} d_{p,l,n} e^{jn\Delta\omega(t'-\tau_{0p}-\tau_u'-lT_s-pT_p)} du'.$$

$$(5.5.5)$$

Rearranging terms leads to

$$s_r(t') = \sum_{p=0}^{P-1} \sum_{l=0}^{L-1} \sum_{n=-N/2}^{N/2-1} \varphi_{p,l,n} d_{p,l,n} e^{jn\Delta\omega t'} \int_{u'_a}^{u'_b} g(u') e^{-j(\omega_0+n\Delta\omega)\tau'_u} du' \qquad (5.5.6)$$

where

$$\varphi_{p,l,n} = e^{-j[(\omega_0+n\Delta\omega)(lT_s+pT_p)+n\Delta\omega(\tau_{0p})]}. \qquad (5.5.7)$$

Note that (5.5.7) adjusts the phase due to slant range to scene center (τ_{0p}), the timing of the pulse (pT_P), and the position of the reference symbol within the pulse (lT_s). From [49], τ'_u can be approximated by $2u'\cos(\beta/2)/c$. Defining the spatial frequency variable $k'_n = 2(\omega_0+n\Delta\omega)\cos(\beta/2)/c$ and phase history $G[k'_n] = \int_{u'_a}^{u'_b} g(u') e^{-jk'_n u'} du'$, (5.5.6) can be rewritten as

$$s_r(t') = \sum_{p=0}^{P-1} \sum_{l=0}^{L-1} \sum_{n=-N/2}^{N/2-1} \varphi_{p,l,n} d_{p,l,n} G_{p,l}[k'_n] e^{jn\Delta\omega t'}. \qquad (5.5.8)$$

The equation form in (5.5.8) suggests that a range profile is attainable from each of the L symbols in all of the P subframes in a collection. The φ term accounts for the instantaneous phase at the time a particular symbol is transmitted, effectively "tracking" the instantaneous phase along the transmitted sequence. Since the velocity of a collection platform is much slower than the speed of light, all sequential symbols from the same subframe will produce a coherent version of the reflectivity function from the same collection azimuth. This property is exploitable in the estimation of the range profiles and is discussed subsequently.

Consider a segment from the pth pulse which includes the returns associated with

lth symbol and described by

$$s_{p,l}(t') = \sum_{n=-N/2}^{N/2-1} \varphi_{p,l,n} d_{p,l,n} G_p[k'_n] e^{jn\Delta\omega t'}. \tag{5.5.9}$$

Because OFDM is only defined over N discrete frequencies, the baseband sampling is key to ensure proper correlation with a reference signal. The DFT represents the sampled spectrum of a periodic discrete sequence with period N and frequency spacing of $\omega = 2\pi/N$ [75]. The inverse DFT process in the OFDM generation produces the discrete time-domain version consisting of N samples per symbol with time spacing of T_s/N. For a single WiMAX OFDM symbol, the baseband frequency samples are defined at $\omega_n = \frac{2\pi n}{N}$ for $n = -N/2, -N/2 + 1, \ldots, N/2 - 1$.

Since N defines both the number of baseband time samples per symbol and the number of frequency samples, it is convenient to sample the baseband time domain segments at a rate of T_s/N. In this way, the segments are easily correlated to the elemental form of the underlying data d_n, significantly reducing complexity in the processor. The sampling interval of T_s/N leads to the discrete form of (5.5.9)

$$s_{p,l}[qT_s/N] = \sum_{n=-N/2}^{N/2-1} \varphi_{p,l,n} d_{p,l,n} G_p[k'_n] e^{jn\Delta\omega q T_s/N} \tag{5.5.10}$$

where $q = \{0, 1, \ldots, Q-1\}$, and Q defines the number of samples in the segment. Noting that $\Delta\omega T_s = 2\pi$ and applying the DFT to (5.5.10) yields

$$\sum_{q=0}^{Q-1} s_{p,l}[qT_s/N] e^{-j2\pi nq/Q} = \sum_{q=0}^{Q-1} \sum_{n=-N/2}^{N/2-1} \varphi_{p,l,n} d_{p,l,n} G_{p,l}[k'_n] e^{j2\pi nq(1/N-1/Q)} \tag{5.5.11}$$

for all p, l. For segments of length $Q = N$, (5.5.11) reduces to

$$S_{p,l,n} = \varphi_{p,l,n} d_{p,l,n} G_{p,l}[k_n'] N^2 \tag{5.5.12}$$

leading to a down-range phase history solution of

$$G_{p,l}[k_n'] = \frac{S_{p,l,n}}{\varphi_{p,l,n} d_{p,l,n} N^2}, \quad d_{p,l,n} \neq 0. \tag{5.5.13}$$

The segment need not be limited to N samples. For segments of length $Q \neq N$, the addition of zero-valued time samples to a length of $Q' = zN$ where $z \in I > 1$ will do. The reference symbol is also treated to a length of Q' and after correlation, the resulting spectrum is downsampled by a rate of $1/z$, reducing the discrete frequency sequence to the length of N. However, care should be taken since the return spectrum will either be undersampled $(Q < N)$ or will include spectrum interference from adjacent symbols not in the reference signal $(Q > N)$.

It is convenient to express (5.5.13) in matrix form [51]

$$\boldsymbol{G}_{p,l} = \boldsymbol{\Psi}_{p,l} \boldsymbol{D}_{p,l}^{-1} \boldsymbol{S}_{p,l} \tag{5.5.14}$$

where $\boldsymbol{G}_{p,l}$ is the N-length phase history vector associated with lth symbol of the pth subframe

$$\boldsymbol{G}_{p,l} = \left[G_{p,l}[k_{-N/2}] \quad G_{p,l}[k_{-N/2+1}] \quad \dots \quad G_{p,l}[k_{N/2-1}] \right]^T,$$

$$\boldsymbol{D}_{p,l} = \begin{bmatrix} d_{p,l,-N/2} & 0 & \ldots & 0 \\ 0 & d_{p,l,-N/2+1} & \ldots & 0 \\ \vdots & \vdots & \ddots & \vdots \\ 0 & 0 & \ldots & d_{p,l,N/2-1} \end{bmatrix},$$

and

$$\boldsymbol{\Psi}_{p,l} = \begin{bmatrix} \frac{1}{\varphi_{p,l,-N/2}} & 0 & \ldots & 0 \\ 0 & \frac{1}{\varphi_{p,l,-N/2+1}} & \ldots & 0 \\ \vdots & \vdots & \ddots & \vdots \\ 0 & 0 & \ldots & \frac{1}{\varphi_{p,l,-N/2-1}} \end{bmatrix}.$$

Note that the solution in (5.5.14) requires that the determinant $|\boldsymbol{D}_{p,l}| \neq 0$. Recall that in the WiMAX case, some subcarriers are intentionally set to 0 (e.g., guardbands and the DC carrier) producing a non-invertible matrix $\boldsymbol{D}$. A viable alternative to a direct inversion is to use a pseudoinverse form

$$\boldsymbol{D}'_{p,l} = \begin{bmatrix} d'_{p,l,-N/2} & 0 & \ldots & 0 \\ 0 & d'_{p,l,-N/2+1} & \ldots & 0 \\ \vdots & \vdots & \ddots & \vdots \\ 0 & 0 & \ldots & d'_{p,l,N/2-1} \end{bmatrix}$$

where the inversion of the diagonal elements in $\boldsymbol{D}$ take the familiar complex conjugate form of a match filter

$$d'_n = \begin{cases} \frac{d^*_{p,l,n}}{|d_{p,l,n}|^2}, & \text{for } d_{p,l,n} \neq 0 \\ 0, & \text{for } d_{p,l,n} = 0 \end{cases} \tag{5.5.15}$$

leading to [51]

$$\boldsymbol{G}_{p,l} = \boldsymbol{\Psi}_{p,l} \boldsymbol{D}'_{p,l} \boldsymbol{S}_{p,l}. \tag{5.5.16}$$

The phase history solution involves the correlation of return signal with a phase-

corrected version of the reference signal. Individually processed returns are arranged in matrix form to complete the two-dimensional N-by-P phase history array

$$\boldsymbol{\Phi_l} = \begin{bmatrix} G_{1,l}[k_{-N/2}] & G_{2,l}[k_{-N/2}] & G_{3,l}[k_{-N/2}] & \ldots & G_{P,l}[k_{-N/2}] \\ G_{1,l}[k_{-N/2+1}] & G_{2,l}[k_{-N/2+1}] & G_{3,l}[k_{-N/2+1}] & \ldots & G_{P,l}[k_{-N/2+1}] \\ \vdots & \vdots & \vdots & \ddots & \vdots \\ G_{1,l}[k_{N/2-1}] & G_{2,l}[k_{N/2-1}] & G_{3,l}[k_{N/2-1}] & \ldots & G_{P,l}[k_{N/2-1}], \end{bmatrix} \quad (5.5.17)$$

which is used to produce the final SAR image product. When using (5.5.16) and (5.5.17) to build SAR phase history from a series of symbol returns, the concepts of phase coherence, multi-symbol use, and timing synchronization must be carefully considered.

Achieving phase coherence in the phase history array requires that all the down-range profiles are phase shifted to the center of the spotlighted scene ($u' = 0$). That is the job of $\boldsymbol{\Psi}$ in (5.5.16) where each subcarrier is phase shifted by $1/\varphi_{p,l,n}$. The phase terms associated with the discrete times lT_s and pT_p account for the phase shift due to frame and symbol transmission time under a continuously running local frequency oscillator (LCO). Proper functionality of the phase adjustment will depend to some extent on the ability to synchronize the transmitter and receiver clocks typically achieved to an acceptable level through the use of phase lock loops (PLL) in the receiver [2].

To this point, a single WiMAX OFDM symbol with no CP has been considered as the reference signal in the match filter process. There are certain WiMAX features that could either hinder imaging solutions or create processing opportunities not available with other waveforms. For example, the symbol sequence nature of the

transmission gives way to creative multi-symbol processing schemes. Other features like the CP will impact correlation in the process and the use of preamble symbols exclusively will limit the utility of the solution. The following sections present a closer look at the impact of these and other WiMAX features to the SAR image.

Working with Multiple Symbols.

Since each WiMAX DL is comprised of a series of unique symbols, multi-symbol filtering options abound. Many creative algorithms can be designed to take advantage of the information diversity present in a WiMAX signal. Assuming that the modulation data d_n for every OFDM symbol is either known or attainable, two possible algorithm designs are proposed: the *full segment match filter* (FSMF), and the *averaging match filter* (AMF). Like most passive radar designs, the FSMF uses the complete length of the segment as its processing "pulse". That is, all the symbols within the segment are processed as a series rather than individually. The reference signal can be digitally built using the transmitted data d_n. On the other hand, the AMF estimates one single-dimensional range profile from individual or sub-groups of symbols in the return segment and then averages all the solutions to produce a single range profile. In this way, the AMF results in a processing gain similar to that produced through the increase of a CPI in detection radar, reducing noise in the averaged solution.

Consider a segment length of ΛT_s where Λ represents the number of consecutive symbols in a segment and T_s is the duration of a single symbol. For clarity, assume no CP at this time. The segment will have return energy from at least Λ symbols, each with the potential to produce an independent ranging solution in additive white

Gaussian noise (AWGN). Using the form in (5.5.16), the FSMF can be defined in spatial frequency domain as

$$\boldsymbol{G}_{p,\Lambda} = \left[\sum_{l=\Lambda_a}^{\Lambda_b} \boldsymbol{\Psi}_{p,l} \boldsymbol{D}'_{p,l} \right] \boldsymbol{S}_{p,\Lambda} \tag{5.5.18}$$

where Λ_a and Λ_b are the first and last reference symbols wholly in the segment respectively. For the purpose of this research, the matrix $\left[\sum_{l=\Lambda_a}^{\Lambda_b} \boldsymbol{\Psi}_{p,l} \boldsymbol{D}'_{p,l} \right]$ will be known as the *reference matrix* of size N-by-N and $\boldsymbol{S}_{p,\Lambda}$ is the *segment spectrum* of length N. The AMF takes the form

$$\boldsymbol{G}_{p,\Lambda} = \frac{1}{\Lambda} \sum_{l=\Lambda_a}^{\Lambda_b} \boldsymbol{\Psi}_{p,l} \boldsymbol{D}'_{p,l} \boldsymbol{S}_{p,l} \tag{5.5.19}$$

In both cases, the segment $\boldsymbol{S}_p$ must contain the spectrum of at least one symbol in the reference matrix. Ideally, the segment will contain return energy from the symbols in the reference matrix exclusively. Note that a segment in the AMF can be extracted through the implementation of a sliding window design over the collected return.

Two metrics are defined to aid in the performance evaluation of the match filter apporaches, the reference-to-segment ratio (RSR) and the peak signal-to-noise ratio (PSNR). Define the RSR as

$$\text{RSR} = \frac{\text{number of symbols in reference}}{\text{number of symbols in segment}} \tag{5.5.20}$$

and the PSNR as [1]

$$\text{PSNR} = 20 \log_{10} \left(\frac{1}{\sqrt{MSE}} \right) \tag{5.5.21}$$

where the numerator is the maximum attainable normalized correlation (or peak)
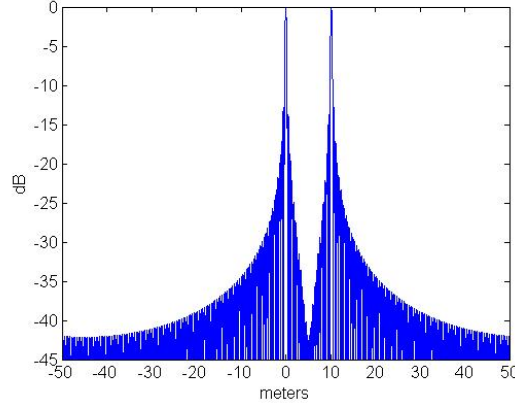
Figure 38. Baseline or truth response, 768 MHz bandwidth. This solution is the average FSMF response of 300 unique reference symbols. Reference-to-segment ratio (RSR) is 1/1.

value and

$$MSE = \frac{1}{rc} \sum_{i=0}^{r-1} \sum_{j=0}^{c-1} ||f(i,j) - g(i,j)||^2 \qquad (5.5.22)$$

is the mean square error of the "perfect" correlation f and the filter response g under evaluation, and $[r, c]$ are the row and column sizes of the array. It is important to emphasize that the PSNR is an image processing metric which measures the ratio of a true image to its distorted version. Not to be confused with the signal-to-noise ratio (SNR) of the received signal. As such PSNR is used strictly to measure the performance of the correlator or match filter output under various return signal and filter configurations.

Note that (5.5.21) and (5.5.22) are not limited to a two-dimensional array; it also serves as a metric for the one-dimensional range profile responses. Since every symbol will produce negligible differences in the solution due to variable frequency content, the truth response for this research is created by averaging the FSMF response from 300 different symbols under no noise conditions with an RSR = 1/1. Figure 38 shows the truth or baseline response showing one simulated target at the center of the profile
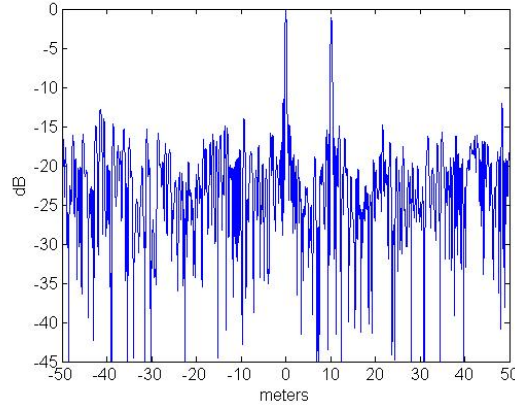
Figure 39. FSMF response to an RSR of 1/2, PSNR = 23.4 dB.
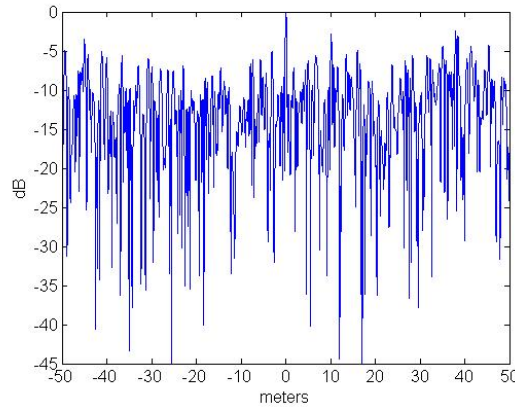
Figure 40. FSMF response to an RSR of 1/10, PSNR = 12.2 dB.

and a second simulated target at 10 meters. The OFDM bandwidth used in the match filter simulations is B=768 MHz. As can be inferred from (5.5.18) and (5.5.19), the AMF response (not shown) would be identical when the same 300 symbols are used.

Figures 39 and 40 show the FSMF results for RSR ratios of 1/2, and 1/10 respectively. As expected for lower RSR values, the response degrades when having spectrum interference from additional symbols not included in the reference matrix. The only practical need for lower RSR values would be under high uncertainty of where one symbol begins and ends; by capturing a longer segment one guarantees that the symbol of interest and all its multipath versions are found within the seg-
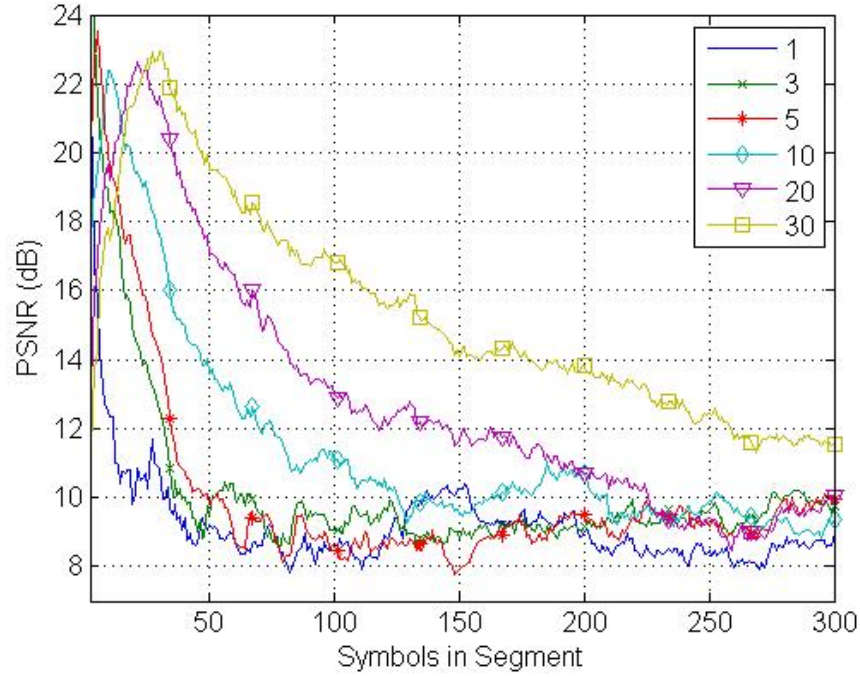
Figure 41. RSR versus PSNR using the FSMF. Legend identifies number of symbols in reference matrix while the horizontal axis is the number of symbols in segment [51].

ment.

There are many RSR combinations possible when considering multi-symbol process. For example, more symbols could be included in the reference matrix. Figure 41 shows the PSNR as a function of several RSR combinations. The noisy character of the curves is due to the randomness of the data d_n in the symbols (random spectrums); there is no noise in the simulated returns. Note how for this realization of d_n, the curves peak around PSNR values of 23 dB for RSR values of one (e.g., 3/3, 5/5, 10/10, etc.). Also note how the curves seem to converge to an average floor value of 9 dB at which point there is no clear distinction of the target in the solution. However the transition of the curves to PSNR < 10 dB occurs at different ratios with the slowest PSNR decline seen for the larger number of reference symbols.

The aforementioned observations suggests that the best filtering options are those with an RSR of one using a large number of symbols. Processing and data storage capacity will dictate the optimal RSR value to use in the filtering design. Even though the RSR results where shown for the FSMF filter, the same principle applies to the AMF. In the AMF, one can choose the number of symbols in the reference and in segment subgroups to achieve a particular RSR in the pre-averaging solutions.

Next, AWGN is introduced in the returns simulating receiver thermal noise. In legacy passive radar systems, a separate receiver is typically used to collect the transmitted signal directly from the transmitter. A secondary receiver system will have different noise realizations than the main receiver. The direct signal collection is used as the reference signal in the match filter process. This operation makes sense when building an exact replica of the waveform is impractical or impossible (e.g., AM and FM radio, television, etc.). Using the WiMAX OFDM standard in a communication receiver setup, one could possibly collect and demodulate the waveform to extract the modulating sequence d_n and use it to create a noise-free reference sequence. Alternatively, the WiMAX preambles may be used exclusively as an a-priori known data sequence without the need of a secondary receiver for direct signal collection or the need to demodulate the communication data.

To show the advantage of this approach, the noiseless reference method is compared to the traditional direct signal (DS) method. Figure 42 shows a single realization of the response for a return SNR of -10 dB. The FSMF and the DS use an RSR of 10/10, while the AMF is designed with an RSR = 1/1 for each of the 10 symbols. The AMF (PSNR = 24.5 dB) clearly outperforms the FSMF (PSNR = 12.6 dB) due to the averaging of the solutions while the DS (PSNR = 8.1 dB) could not handle
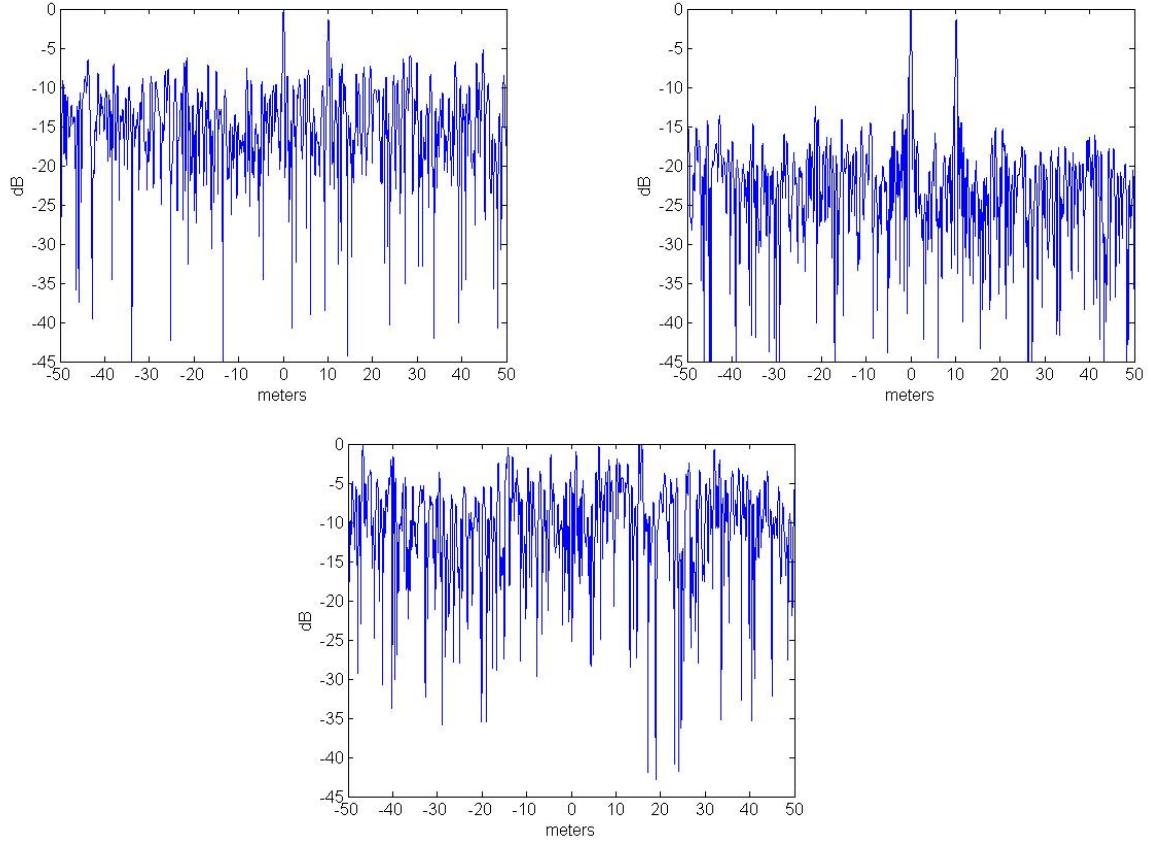
Figure 42. Single realization of the FSMF response (top left, PSNR = 24.5 dB), AMF response (top right, PSNR = 12.6 dB), and DS response (bottom, PSNR = 8.1 dB) for 10 300 MHz OFDM symbols; received SNR = -10 dB [51].

the poor SNR of the signal.

Since it employs an averaging solution, the AMF will benefit from a large number of symbols in the process. Figure 43 shows the filter response PSNR values as a function of number of symbols processed in a AMF for several SNR levels. Each SNR curve is the average of 100 Monte Carlo runs. The data shows that in all cases, the largest rate of improvement is obtained over the first 10 symbols; beyond which less improvement is achieved with increased computational cost. The right amount of symbols to process will be determined by the desired PSNR and processing power. For this research, a maximum of 10 symbols will be used in subsequent simulations
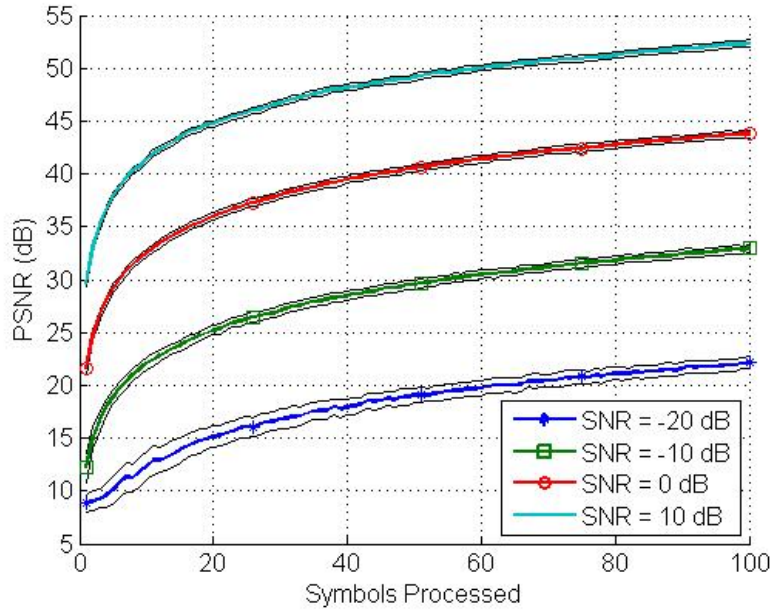
Figure 43. Peak-to-Noise Ratio (PSNR) versus number of symbols processed using AMF for various received signal-to-noise (SNR) ratios. Solid lines around the curves show the standard deviation value from 100 Monte Carlo simulations.

and data collections.

Processing the Cyclic Prefix.

The WiMAX OFDM PHY standard defines the use of a CP for every symbol transmitted to reduce multipath noise in the data recovery. The CP increases the symbol length to $T_s + T_g$ where $T_g = \gamma T_s$ and $\gamma \in \{1/4, 1/8, 1/16, 1/32\}$ in accordance with the standard [63]. However since the CP is a replica of a portion of the symbol, it does not change the spectral content of the reference. In the network, a user receiver searches through all possible CP values and once found, is able to discard the cyclic extension.

In the passive radar, the receiver would also search for the value of the CP but
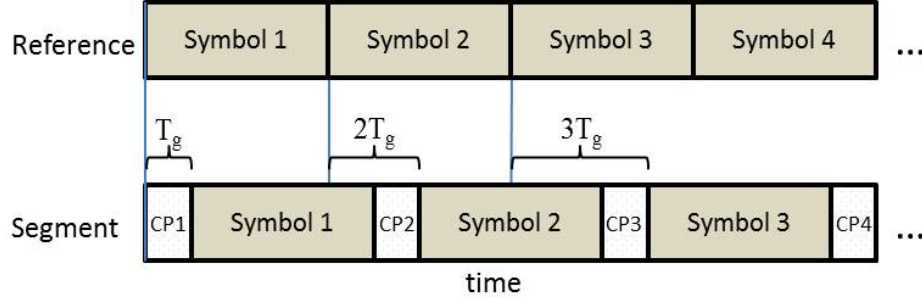
Figure 44. Effect of the CP in the uncorrected match filter. The CP causes incremental correlation peak shifts when reference signal is uncorrected.

the extension needs no discarding. The CP is integrated in the return signal model through (5.5.7)

$$\varphi_{p,l,n} = e^{-j[(\omega_0+n\Delta\omega)(l(T_s+\gamma T_s)+pT_p)+n\Delta\omega(\tau_{0p})]} \tag{5.5.23}$$

From (5.5.23), it becomes clear that the CP adds a phase shift of $e^{-j(\omega_0+n\Delta\omega)l\gamma T_s}$, which translates to a spatial shift in the down-range domain. If the value of γ is known, the phase correction term $e^{j(\omega_0+n\Delta\omega)l\gamma T_s}$ can be included in the phase correction matrix $\boldsymbol{\Psi}$ or it can be included in the reconstructed reference waveform. When processing a single symbol, the CP will only shift the initial phase of the return with respect to the reference waveform and will not impact the quality of the match filter response. The baseband sampling of the return signal still occurs at time intervals of T_s/N where now $Q > N$ (e.g., for RSR=1/1, $N = 256$ and $\gamma = 1/8$, $Q = 288$), thus, the proposed zero-padding and downsampling technique discussed earlier applies.

The effects of the CP will be distinctly noticeable when not corrected in the reference matrix of the match filter process. When no correction is applied, two effects are known to occur: 1) since the CP is appended at the beginning of the symbol, the correlation peak is shifted to the right by T_g, and 2) the filter assumes the symbol duration is T_s, so the next set of return samples into the match filter is shifted by and additional T_g. The concept is best seen in Figure 44. For a bandwidth of 768 MHz,
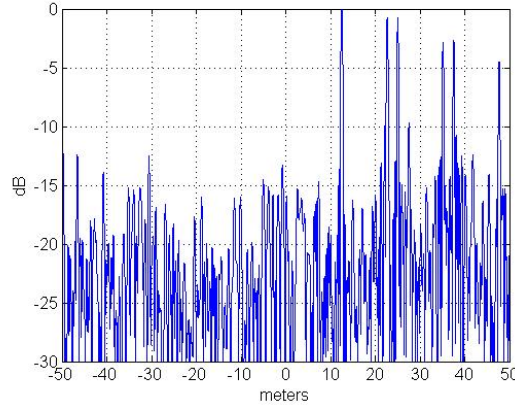
Figure 45. Uncorrected AMF response for three OFDM symbols with CP, $\gamma = 1/8$, 768 MHz.
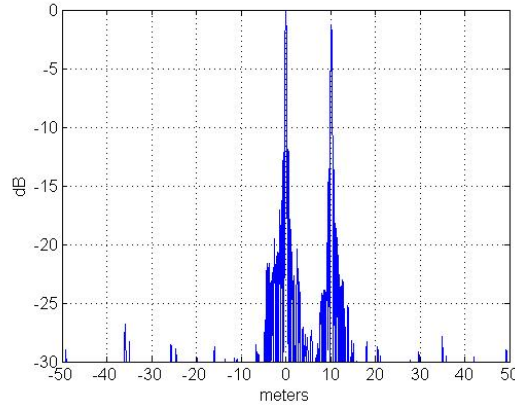
Figure 46. Corrected AMF response for three OFDM symbols with CP, $\gamma = 1/8$, 300 MHz.

and $\gamma = 1/8$, a single shift of T_g translates to a spatial distance of 12.5 meters.

Figure 45 shows the uncorrected response of a 3-symbol AMF. The process produces six distinct peaks, two per symbol for each target. The first two peaks from left to right represent the correlation of the first symbol with the two targets shifted by approximately 12 meters, the second and third target sets are shifted by approximately 25 and 37 meters respectively. This nuisance is easily corrected by integrating the CP in the reference signal of the AMF. Figure 46 shows the response of the AMF when corrected for the CP.

As can be inferred, the CP does not represent a significant obstacle to the use of WiMAX as a radar signal and its impact is shown to be easily correctable. In fact, there might be creative ways to use the CP to augment the final solution but these are beyond the scope of this study. The only correction required is that of the resulting additional spatial shift which is easily achieved once the transmission CP is properly estimated.

Using the Preamble.

Recall that the WiMAX DL subframe carries a series of *preamble*, *FCH*, and *data* communication symbols as shown in Figure 11. Each of these types of symbols have unique purpose and features within the DL. The data and FCH symbols are similar in the sense that both use 200 consecutive subcarriers in the spectrum. The FCH carries critical information describing how to process the rest of the DL. Conversely, the data symbols carry the communication data bits between users and base stations; as such, its spectral and temporal structure depends strictly on the user-base station demands which will be random in nature. Both the FCH and the data symbols will have specific subcarriers designated as *pilot* carriers, using pre-defined modulation for ranging and channel estimation according to [63]. The preamble symbols however deserve special attention.

The preamble symbols have features that makes them both favorable and unfavorable to passive radar collections. On the favorable side, these synchronization and ranging symbols are "boosted" 3 dB higher than the rest of the DL resulting in higher SNR at the passive receiver antenna. In addition, the modulation data and

the subcarriers used are specifically described in [63]; always known and always the same [3]. The preambles eliminate the need to demodulate transmitted data and may be used to synchronize the radar receiver with the WiMAX transmitter using communications receiver algorithms. Unfortunately, the preambles use only a limited set of subcarriers, reducing the number of frequency data samples and in turn, the possible SAR image extent.

There are two preambles symbols defined in [63] for the OFDM PHY which for documentation clarity, are defined here as P1 and P2. P1 modulates every fifth subcarrier (mod4) and P2 every third subcarrier (mod2). Figures 47 and 48 show the subcarrier time and frequency domain representations of P1 and P2 where the subcarrier spacing is easily observed. In time domain, these are represented by four cycles of 64 time units (P1) and two repetitions of 128 time units (P2).

When P1 and P2 are used consecutively, they are known as the *long* preamble and are jointly used as the first symbols in the DL for initial ranging and synchronization. After ranging and synchronization is achieved, the DL preamble consists of a single P1 symbol commonly referred to as the *short* preamble used mainly for channel estimation. There are other preamble configurations for space-time encoding regions and adaptive antenna systems (AAS) but those will not be considered in this research. The frequency domain sequence for all preambles is derived from the master sequence

$$P1 = \begin{cases} 2 \, \text{conj}(P_{code}(k)) & \text{for } k_{mod4} = 0 \\ 0 & \text{for } k_{mod4} \neq 0 \end{cases} \tag{5.5.24}$$

[3]There are several preamble modulation schemes for various WiMAX antenna configurations.
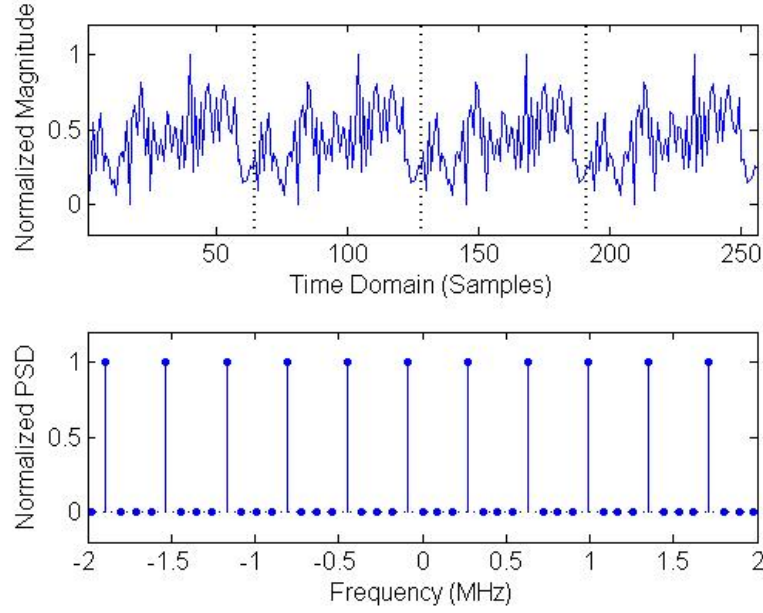
Figure 47. WiMAX OFDM preamble symbol P1; B**=20 MHz. Bottom plot is a zoomed-in version of the frequency spectrum.**
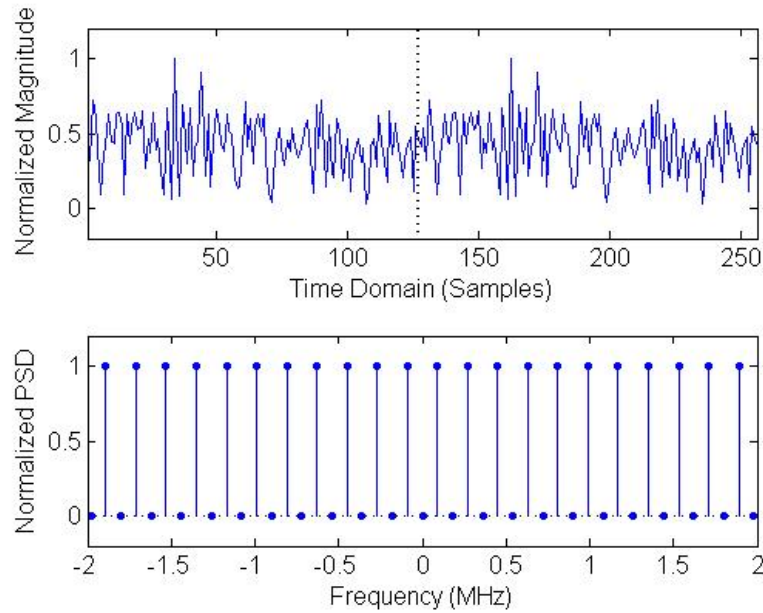
Figure 48. WiMAX OFDM preamble symbol P2; B**=20 MHz. Bottom plot is a zoomed-in version of the frequency spectrum.**
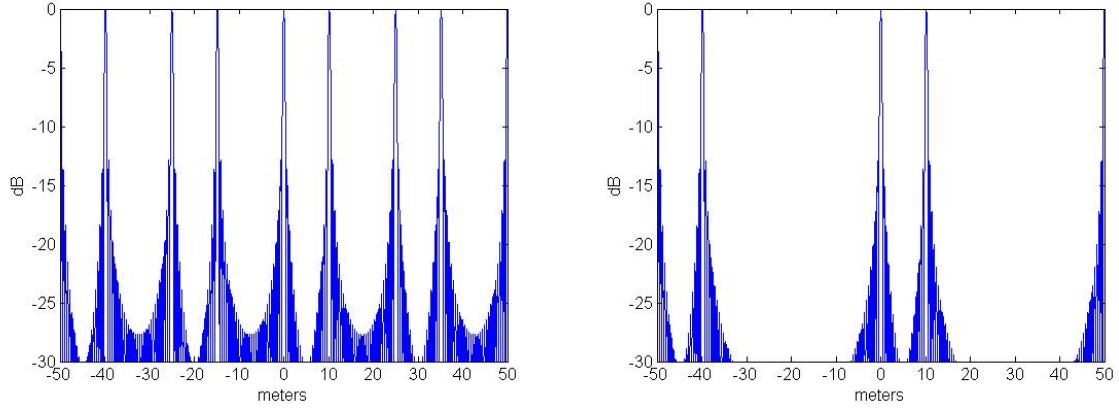
Figure 49. FSMF response for preamble P1 (left) and P2 (right) with no CP, $B = 768$ MHz.

$$P2 = \begin{cases} \sqrt{2} \; \text{conj}(P_{code}(k)) & \text{for } k_{mod2} = 0 \\ 0 & \text{for } k_{mod2} \neq 0 \end{cases} \qquad (5.5.25)$$

for $k = 1, 2, ..., N$ and where P_{code} are complex values taken from a subcarrier-indexed table in [63].

Processing the preambles will be no different than previously discussed for general WiMAX symbols; it is "just another symbol". However, the system designer should be aware that because of the reduced number of distinct frequency samples attainable, processing the preambles by themselves will limit the scene extent (P1 more than P2), reducing the system's usefulness. If used in multi-symbol processing in conjunction with regular data symbols, the preambles will still contribute to an overall increase in PSNR performance.

Figure 49 shows the FSMF response for P1 and P2 for two targets. The aliasing in range is evident with P1 seen to be more restrictive than P2 (50 frequency samples in P1 versus 100 frequency samples in P2). It is clear that by themselves, the imaging

93
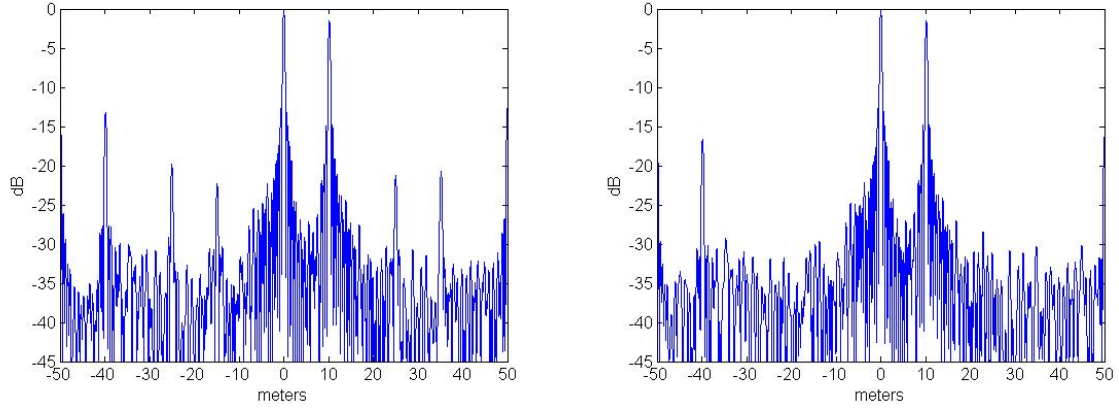
Figure 50. AMF response for 10 data symbols preceded by preamble P1 (left) and P2 (right) with no CP, 768 MHz.

extent is limited. However they can be used in multi-symbol processing effectively as can be seen in Figure 50 where the AMF response using the preamble and 10 additional random data symbols (a total of 12 symbols) is shown. The aliased peaks from the preambles are "averaged out" although they can still be seen in a much smaller scale.

Impact of other WiMAX features.

Other WiMAX features of consideration include the null DC subcarrier ($d_0 = 0$), pilot subcarriers, and frequency-domain guard bands. The pilot subcarriers are no different than any other modulated subcarriers; they simply use a known modulation which is continuously used in transmission channel estimation. Although it creates a small frequency gap in the processed spectrum, the null subcarrier creates no significant impact on the filter response; however the guard bands do.

Recall that of the 256 subcarriers available in a WiMAX OFDM symbol, only the center 200 are used to carry data. The $n = 0$ subcarrier is nulled, and the other 55 are

used as guard bands (also nulled) to reduce inter-carrier (ICI) and inter-symbol (ISI) interference [28]. The null subcarriers will produce no energy at those frequencies slightly reducing the bandwidth of the signal and in turn, the down-range resolution of the image. The impact in resolution is visually negligible as will be shown in the experimental results.

5.6 WiMAX SAR Sources of Error

Any real-world measurement system will inherently produce undesirable errors that deviate the measured value from the truth. In a passive radar imaging system like the one considered in this research those errors which directly impact the final SAR image product are of interest. For this research, three main sources of errors are specifically considered: receiver thermal noise, errors in the receiver's local oscillator (LO) frequency with respect to the transmitting frequency, and *slow time* phase errors associated with the location of the motion compensation point (MOCOMP) in the return signal and other effects. The impact of these errors to SAR products are characterized and their limits established.

The Error Model.

To simplify the error analysis, the single-symbol return signal at the antenna in (4.1.1) is recalled

$$s_{r0}(t) = A_0 \int_{u_a}^{u_b} g(u) e^{j\omega_0(t-\tau_0-\tau_u)} \sum_{n=-N/2}^{N/2-1} d_n e^{jn\Delta\omega(t-\tau_0-\tau_u)} du \qquad (5.6.1)$$

where without loss of generality, it is assumed the collection begins at the same time

as the pulse is transmitted (at $t = 0$), and where all the range variables (u, u_a, u_b, τ_u) are associated with the bistatic geometry (see section 4.2).

At the receiver front end, the LO produces a reference signal with frequency $\omega_0 + \delta\omega$, delay $\tau_0 + \delta\tau$, and thermal noise $w(t)$; where $\delta\omega$ is the error between the transmitter and receiver frequencies, $\delta\tau$ is the timing error with respect to the actual sample location of the scene center in the returned pulse, and $w(t)$ is uncorrelated complex white Gaussian noise. Note that τ_0 is the error-free delay associated with the range to the center of the scene and its purpose is to align in phase all the slow time pulses. The receiver reference signal can then be modeled in complex form by

$$s_{ref} = e^{-j(\omega_0 + \delta\omega)(t - \tau_0 - \delta\tau)} \qquad (5.6.2)$$

which after rearranging exponential terms results in

$$s_{ref} = [e^{j\delta\omega\tau_0} e^{-j\delta\omega t} e^{j(\omega_0 + \delta\omega)\delta\tau}] e^{-j\omega_0(t - \tau_0)}. \qquad (5.6.3)$$

Recall that for a SAR process, a constant phase bias will have no effect on the reconstruction of the scene [57]. Assuming the frequency error $\delta\omega$ is constant during the collection, the first exponential phase term ($e^{j\delta\omega\tau_0}$) can be safely removed from the reference signal model resulting in

$$s_{ref} = [e^{-j\delta\omega t} e^{j(\omega_0 + \delta\omega)\delta\tau}] e^{-j\omega_0(t - \tau_0)}. \qquad (5.6.4)$$

Mixing the reference signal with the return and adding receiver thermal noise $w(t)$
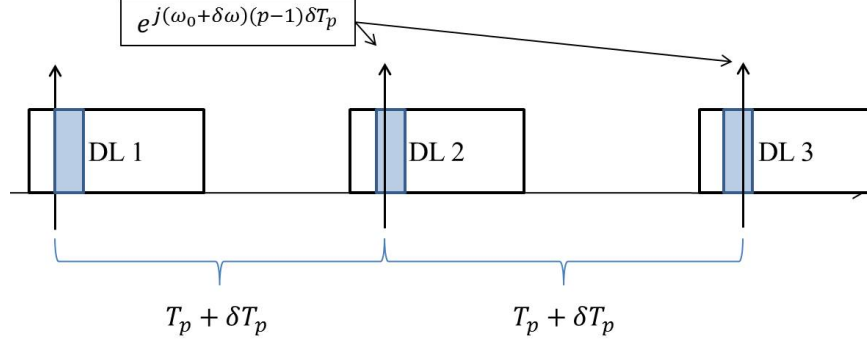
Figure 51. Frame interval error. An error in frame interval will create an incremental phase term along cross-range.

yields

$$\hat{s}_r(t) = [e^{-j\delta\omega t}e^{j(\omega_0+\delta\omega)\delta\tau}]e^{-j\omega_0(t-\tau_0)}A_0 \int_{u_a}^{u_b} g(u)e^{j\omega_0(t-\tau_0-\tau_u)}\sum_{n=-N/2}^{N/2-1}d_n e^{jn\Delta\omega(t-\tau_0-\tau_u)}du + \text{w}(t)$$

(5.6.5)

which can be re-written as

$$\hat{s}_r(t) = [e^{-j\delta\omega t}e^{j(\omega_0+\delta\omega)\delta\tau}]s_r(t) + \text{w}(t)$$

(5.6.6)

where $s_r(t)$ is the error-free down-converted returned signal in (4.1.3). By inspection of (5.6.6), it becomes clear that the received baseband signal is distorted in phase by the residual frequency $\delta\omega$ and the residual delay error $\delta\tau$. Assuming a perfectly stable oscillator, the frequency error $\delta\omega$ manifests itself in fast time along the frequency samples and will be generally constant along slow time. Conversely, the $\delta\tau$ phase term will be constant along fast time but can result in phase variations in slow time.

Another possible phase error source unique to a WiMAX passive radar system would be the frame rate timing. Recall that after the first reference point is selected in the collection data, subsequent segments are extracted based on the estimate of the frame interval. An error in frame interval, either due to estimation or sampling

97
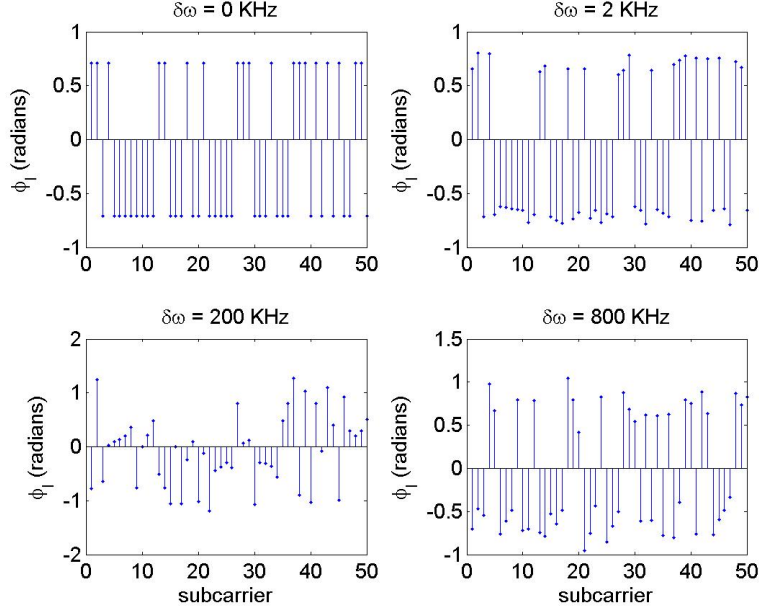
Figure 52. I-channel phase of first 50 subcarriers of arbitrary BPSK OFDM symbol for $\delta\omega = [0, 2, 40, 800]$ KHz.

constant offsets, will cause an incremental phase function along cross-range. The concept is shown in Figure 51. This error can be modeled as

$$Err_{T_p} = e^{j(\omega_0 + \delta\omega)(p-1)\delta T_p} \qquad (5.6.7)$$

where p is the pulse or DL number and δT_p is the constant frame interval error. Including this error in (5.6.6) leads to the final error model

$$\hat{s}_r(t) = [e^{-j\delta\omega t}e^{j(\omega_0 + \delta\omega)(\delta\tau + (p-1)\delta T_p)}]s_r(t) + w(t). \qquad (5.6.8)$$

Impact of Frequency Errors $\delta\omega$ on SAR Products.

In a bistatic scenario, the transmitter and receiver are spatially separated, each using independent LOs. Variations in LO crystals will cause carrier frequency mismatches between the transmitter and receiver introducing phase errors in the down-

Figure 53. Impact of $\delta\omega$ on a monostatic SAR image of an arbitrary target set; no other noise sources are employed. Image created by PFA.

converted baseband return signal.

Assuming no thermal noise and no phase errors, the frequency error behavior is best appreciated by comparing the phase of the OFDM subcarriers transmitter versus the phase of the subcarriers obtained after modulation. Figure 52 shows the reconstructed I-channel phase (after demodulation and downconversion) of the first 50 subcarriers of a BPSK OFDM signal under different levels of frequency errors.

While the phase distortion is clear, the effects on SAR imagery are less evident. Figure 53 shows monostatic SAR images of an arbitrary set of targets for four different values of $\delta\omega$. Note the small degradation at $\delta\omega = 100$ Khz and the visual tolerance at $\delta\omega = 200$ Khz. At $\delta\omega = 800$ KHz the image is no longer recognizable. Although 800 KHz would seem to be a large error, one can appreciate that it consists of only 0.08% of a 1 GHz carrier frequency. Phase lock loop (PLL) and frequency lock loop (FLL) circuitry should be able to maintain the phase and frequency errors under acceptable levels. Receiver error-correction designs are beyond the scope of this research.

Max phase err = π/4	Max phase err = π/2	Max phase err = π	Max phase err = 3π/2
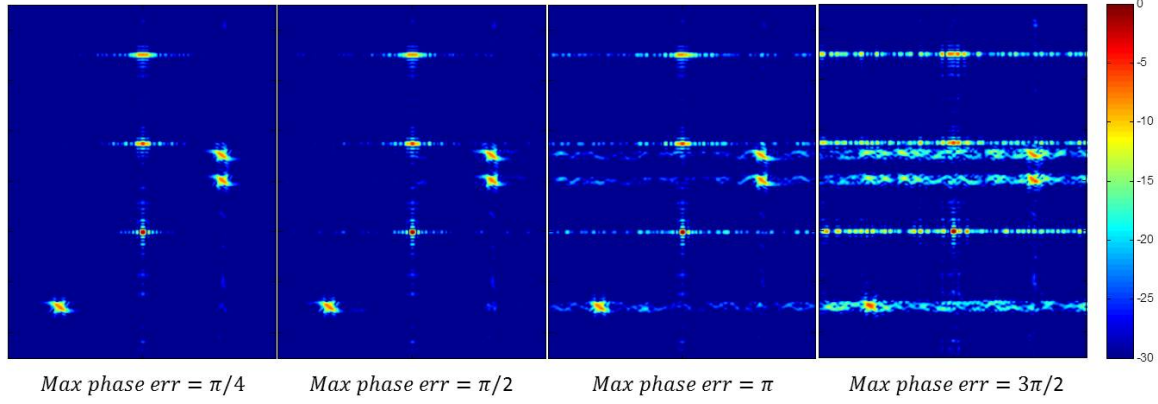
Figure 54. Impact of phase errors on a monostatic SAR image of an arbitrary target set. The phase errors are uniformly distributed along the phase history cross-range; no other noise sources are employed. Image created by PFA.

Impact of Phase Errors on SAR Products.

The spotlight mode SAR process requires every pulse in slow time to be referenced to the MOCOMP. Navigation measurement errors are the leading cause of phase errors along slow time. Errors in navigation measurements will produce errors in the range-to-scene center R_{R0} and in turn variations in phase that may destroy coherence and hinder image reconstruction [12]. Other phase perturbations can occur due to turbulence in the receiver flight path and ground antenna movement. A maximum phase error of $\pi/4$ along phase history slow time is considered tolerable [57].

Figure 54 shows SAR images under different levels of phase errors. The errors were applied along the cross-range domain using a uniform distribution between 0 and the maximum phase error value shown under each image. As expected, phase errors of $\pi/4$ or lower are considered negligible. Very small degradation can be seen at $\pi/2$ while significant image distortion is seen with phase errors greater than π. Correction of these phase errors will be based primarily on the capability and performance of the passive radar system and as such, is not discussed further.

$\delta T_{p,} phase\ slope = 0$ $\delta T_{p,} phase\ slope = \pi/3$ $\delta T_{p,} phase\ slope = \pi$
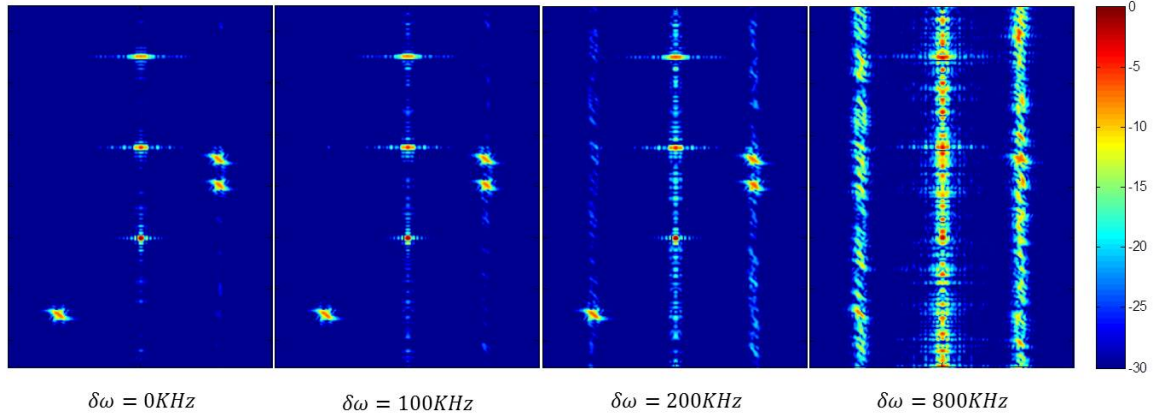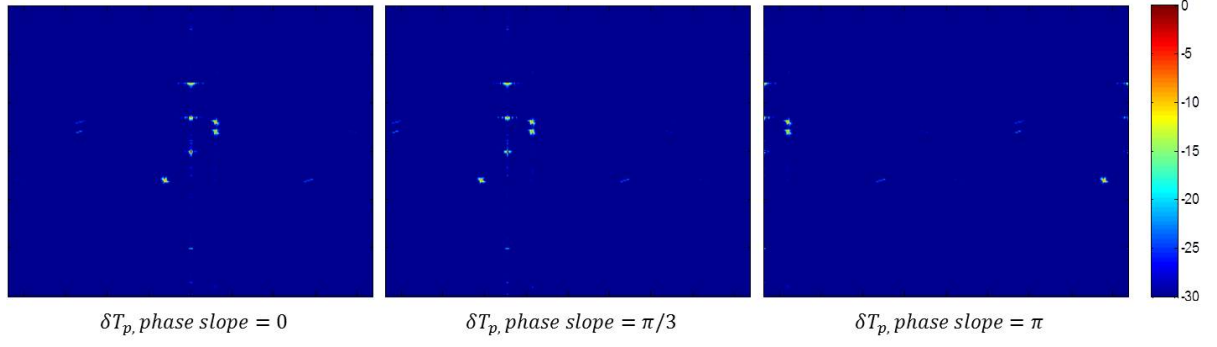
Figure 55. Impact of δT_p errors on a monostatic SAR image of an arbitrary target set; no other noise sources are employed. Image created by PFA.

The effect of the phase error due to frame interval error δT_p will manifest itself as a spatial shift in the image domain. As seen in Figure 55, the larger the error, the larger the cross-range shift. As long as the error is constant, there will be no further image degradation. Note that since the shift is circular, the worst possible error is produced with a slope of $p\pi$.

VI. Experimental Results

To support this research, an experimental OFDM radar setup was designed and configured using Tektronix laboratory equipment through MATLAB software interface. The radar configuration is inspired by the experimental radar setup in [85] and is organic to the radar instrumentation laboratory (RAIL) at the Air Force Institute of Technology.

The experiments consists of specific collections to validate two concepts: 1) the one-dimensional range compression model, and 2) the two-dimensional SAR imagery model under small and large bistatic angles. All the waveforms were created using random data d_n and where applicable, they precisely follow the IEEE 802.16-2009 OFDM PHY guidelines. However, the transmission is limited to static conditions using a pulse-by-pulse sequence, bypassing the continuous timing model of the pulses and its associated signal processing. Perhaps future data collections can include these timing variables or test WiMAX deployments with moving receivers to evaluate the processing design performance.

6.1   Experimental OFDM Radar

Figure 56 shows the experimental radar setup. A Tektronix AWG7102 arbitrary waveform generator (AWG) is used as the transmitter source. The AWG feeds a Mini-Circuits ZKL-2R7 amplifier driving an AirMax 2G-16-90 sector antenna which is used in some WiMAX RF systems. The receiver hardware consist of another AirMax 2G-16-90 sector antenna feeding a Tektronix TDS6124 digital storage oscilloscope (DSO) through a Mini-Circuits ZRL-3500 low-noise amplifier. The receiver antenna can be
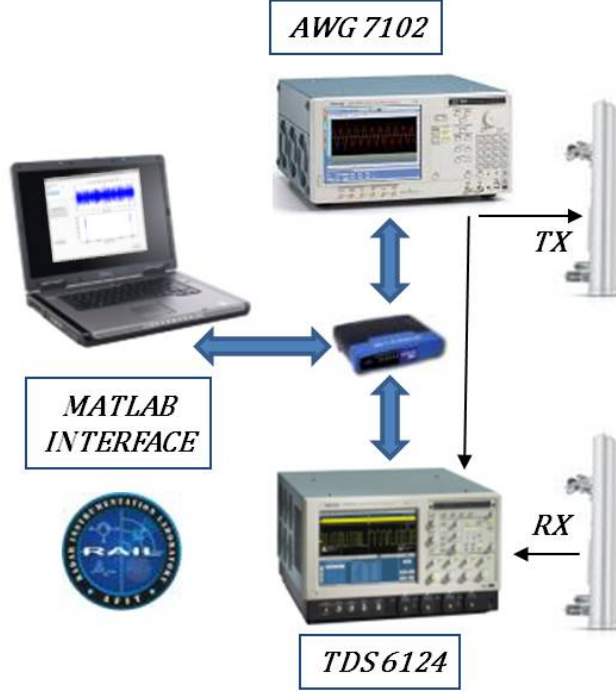
Figure 56. Experimental OFDM Radar. [49]

mounted on a software-controllable linear track which is used to move the antenna in
one dimension with precise positioning in SAR collections. The radar and the linear
track is operated through a laptop computer using a MATLAB interface. Communi-
cations between the AWG, the DSO, and the laptop is achieved through a standard
wired local area network (WLAN) connection.

The MATLAB software interface developed for this research controls the radar
system through a series of graphical user interfaces (GUIs). The waveform GUI
shown in Figure 57 provides flexible functionality for the creation of general OFDM
or WiMAX-specific waveforms. The waveform generation function uses random com-
plex data (d_n) to create the required number of OFDM symbols. WiMAX-specific
features such as guardbands, cyclic prefixes, and pilot subcarriers can be applied to
symbols individually or in combination.
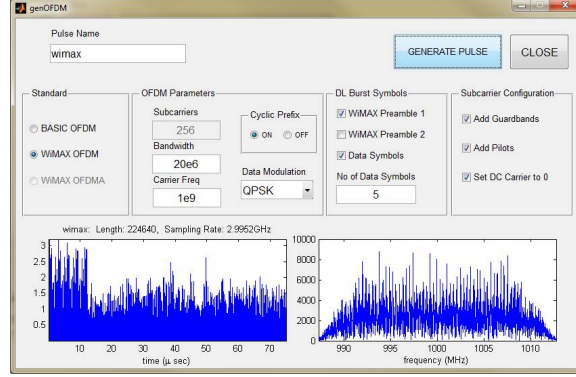
Figure 57. Waveform generator GUI (MATLAB).
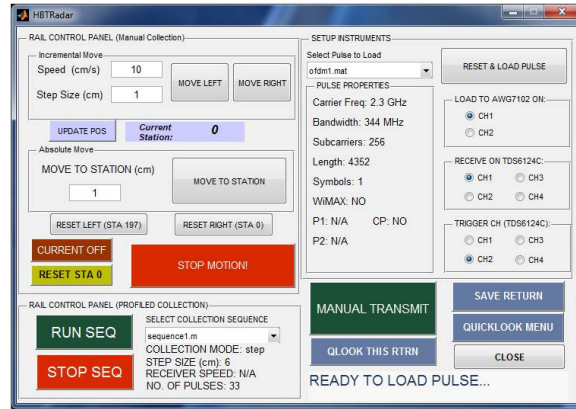
Figure 58. Radar controller GUI (MATLAB).

The operation of the radar and the linear track is controlled using the GUI screen shown in Figure 58. The interface main function is to send instruction messages to the AWG and the DSO, triggering transmission, collection, and file management of the recorded data. The GUI also controls waveform selection, instrument setup, and channel configuration. Lastly, the GUI sends movement control messages to the linear track and is capable of running automated moving and triggering sequences.

Once the desired baseband OFDM waveform is built in complex form, it is mixed with the complex form of the carrier frequency $(e^{-j2\pi f_c})$ via software. The real and imaginary parts of the complex passband signal are added to produce real digital samples, which are loaded into the AWG for transmission. Once the desired wave-

104
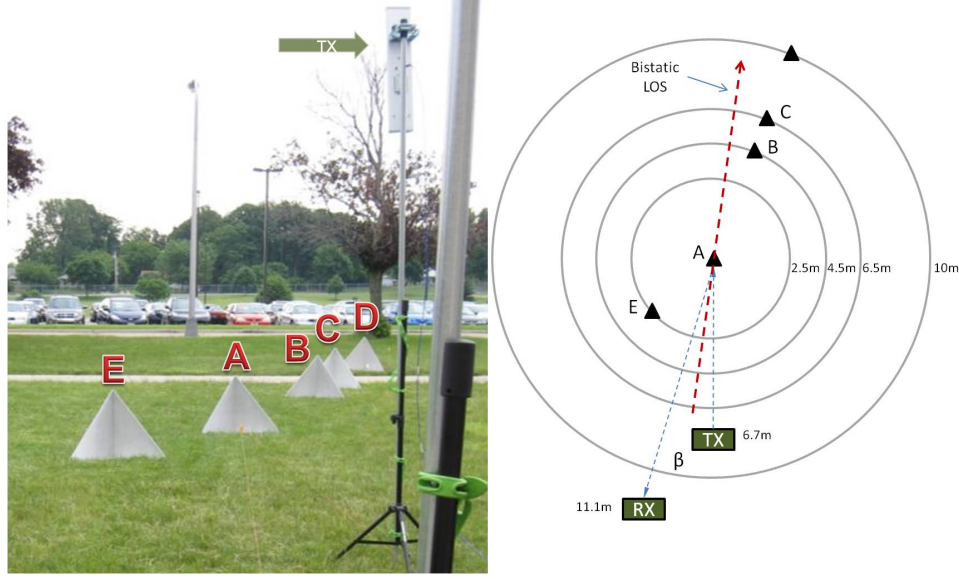
Figure 59. Experimental configuration I: Target setup for range profiles. Dimensions next to transmitter and receiver are slant ranges to center target A; isorange rings are ground ranges relative to target A. Bistatic angle $\beta = 7$ degrees.

form is loaded, the user selects the operation mode. During operation, the software triggers the AWG for transmission and a parallel output is routed to the DSO to trigger waveform acquisition for a specified time interval. All transmissions in this research employ horizontal polarization. After acquisition, the captured radar return and configuration data are saved for post processing in the digital domain.

6.2 Single-Dimensional Range Profiles

To verify the OFDM range profile model, Experimental configuration I is used and includes five identical corner reflectors for ground Targets A, B, C, D, and E; positioned as shown in Figure 59. The target arrangement is designed to ensure full target LOS to both antennas. Target A is chosen as the center of the target profile (range=0). The transmitter and receiver antennas are setup in a bistatic configuration, elevated 3.0 meters above ground and separated by 4.4 meters to reduce the

105

transmitter's direct path signal interference from the backlobes.

A generic (non-WiMAX) 256-point OFDM symbol is generated in MATLAB and loaded onto the AWG for transmission. The symbol bandwidth is $B = 115$ MHz and the transmission carrier frequency is set to $f_c = 2.35$ GHz. Single-symbol pulses are transmitted towards the center of the scene (Target A) and the returns collected in the DSO. The collected data are then processed to obtain range profiles using the inverse Fourier transform of (4.1.11) without the use of windowing functions or any other resolution enhancing techniques. The bistatic angle of $\beta = 7$ degrees produces a theoretical resolution along the bistatic LOS of [98]

$$\rho_y = \frac{c}{2B\cos(\beta)} = 1.3 \text{ meters.} \tag{6.2.1}$$

Note that for small values of β, the bistatic resolution approaches the theoretical monostatic down-range resolution.

To clearly identify targets in the range profiles, a target build-up approach is employed. The first set of collections use Target A only, with the remaining targets added to the scene in subsequent collections. All range profile figures are normalized with respect to Target D amplitude. The normalization of the results in lieu of using a decibel scale aids in the visual identification of the targets in the profiles.

Results for the single target case are shown in Figure 60 where the target A response is identified by the red arrow. In addition to target A, there are other relatively large returns observed. The one at -7 meters down-range (green arrow) is due to the backlobe of the transmitter antenna which was located at a slant range of approximately 7 meters from target A. The sources of the non-target returns seen beyond
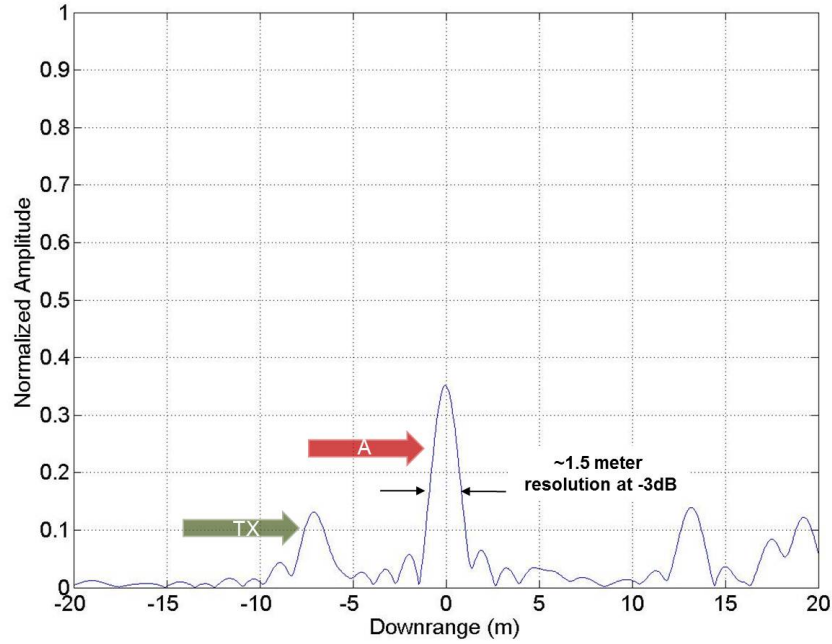
Figure 60. Range Profile 1, Bandwidth $B = 115$ MHz, Target A only.

13 meters down-range are unknown but could possibly be due to the tree, light pole, or vehicles seen in the background in Figure 59. The return sidelobes are measured graphically at approximately -15 dB below the main peak while the -3 dB measured point resolution for target A is $\rho_y = 1.5$ meters.

Next, targets B and C are added to the scene and separated 2 meters from each other to verify the achievable resolution using the OFDM waveform. Contrasting Figure 60, the two additional target responses are clearly observed in Figure 61.

The addition of targets D and E produces the results shown in Figure 62. Although target D is easily distinguishable, target E is not; one can argue that is not in the profile. Careful analysis of the data leads us to believe that the orientation of the target with respect to the transmitter and receiver antennas was such that returns were not reaching the receiver (a corner reflector will produce a signal return in the

107
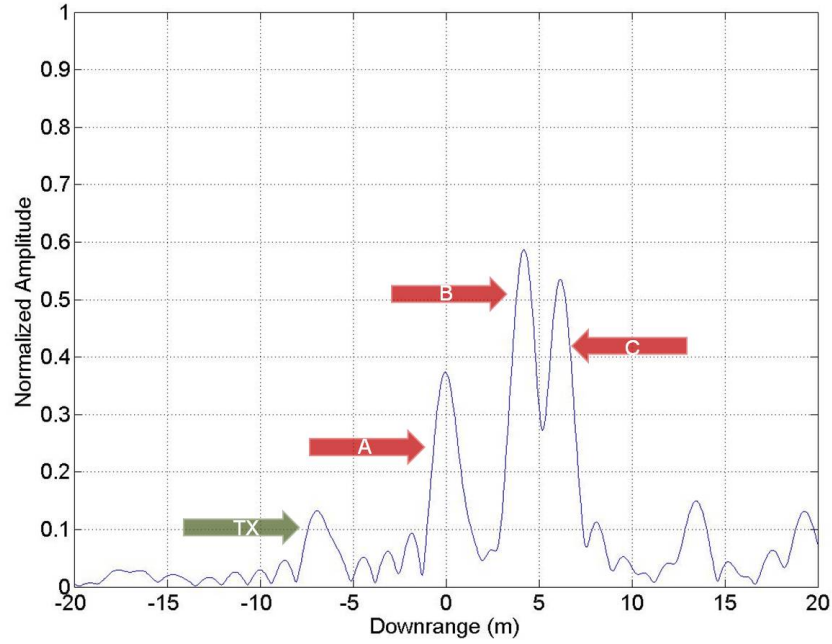
Figure 61. Range Profile 2, Bandwidth $B = 115$ MHz, Targets A, B, C.

direction of incidence).

Lastly, an OFDM waveform bandwidth of $B = 344$ MHz is used over the full target scene producing the range profile seen in Figure 63. In this case, the measured resolution at the -3 dB point is 0.4 meters. Note that as expected, the higher bandwidth improves the down-range resolution threefold. As in Figure 62, target E is not observed.

One interesting observation from the single-dimensional profiles is the variability in amplitude between the target returns; as much as a 4 dB difference in amplitude can be observed between targets A and D. The differences in amplitude can be attributed to variations in orientation between the transmitter, receiver, and the corner reflector targets. Figure 65 shows the antenna beam patterns for the horizontal polarization while Figure 64 shows the RCS pattern of the corner reflector for various

108
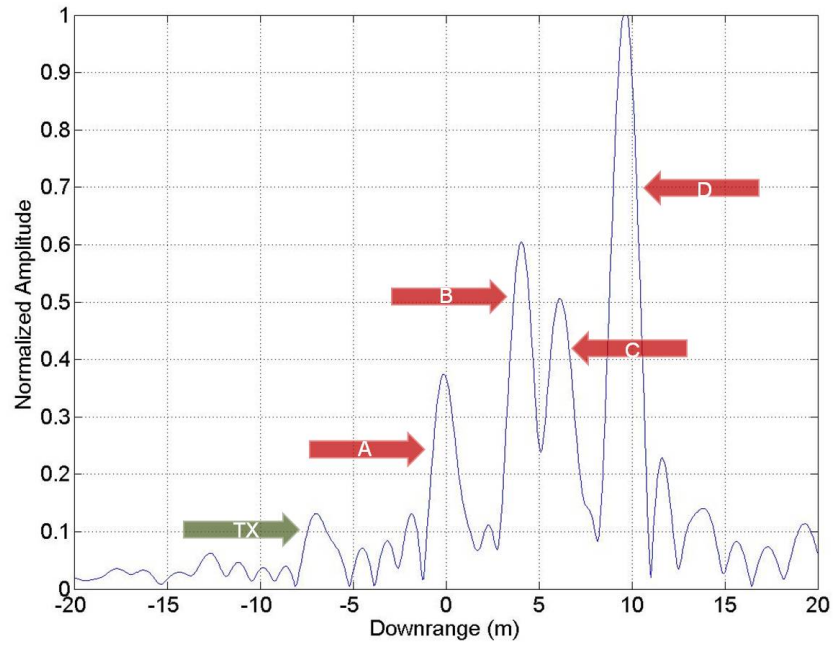
Figure 62. Range Profile 3, Bandwidth $B = 115$ MHz, Targets A, B, C, D, E.
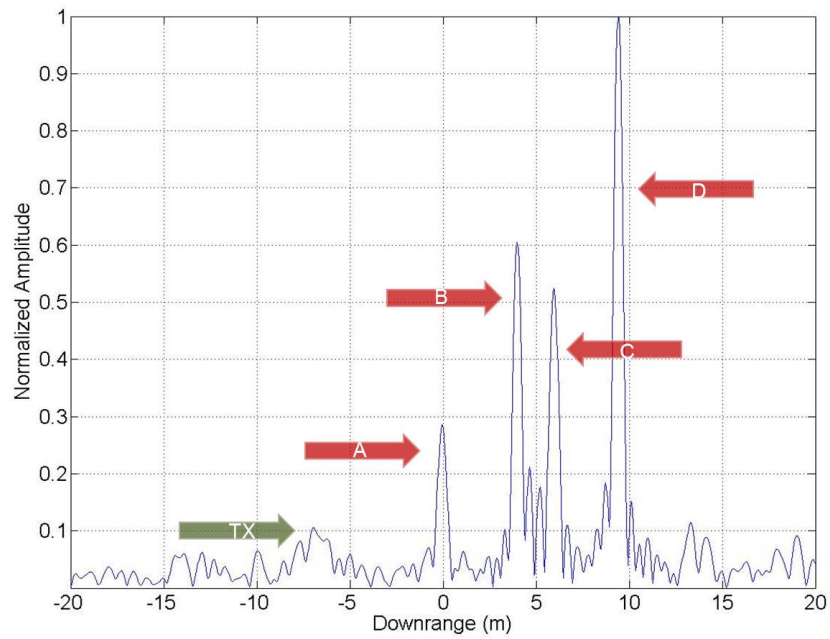
Figure 63. Range Profile 3, Bandwidth $B = 344$ MHz, Targets A, B, C, D, E.

109
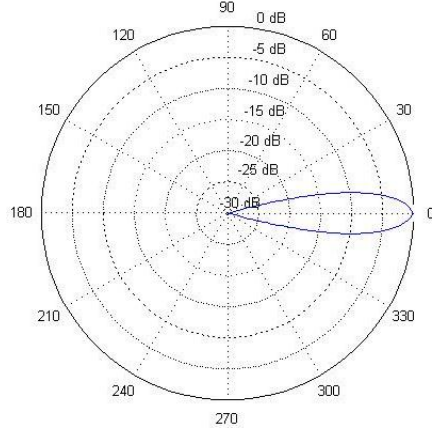
Figure 64. Simulated trihedral target RCS pattern along azimuth, normalized.
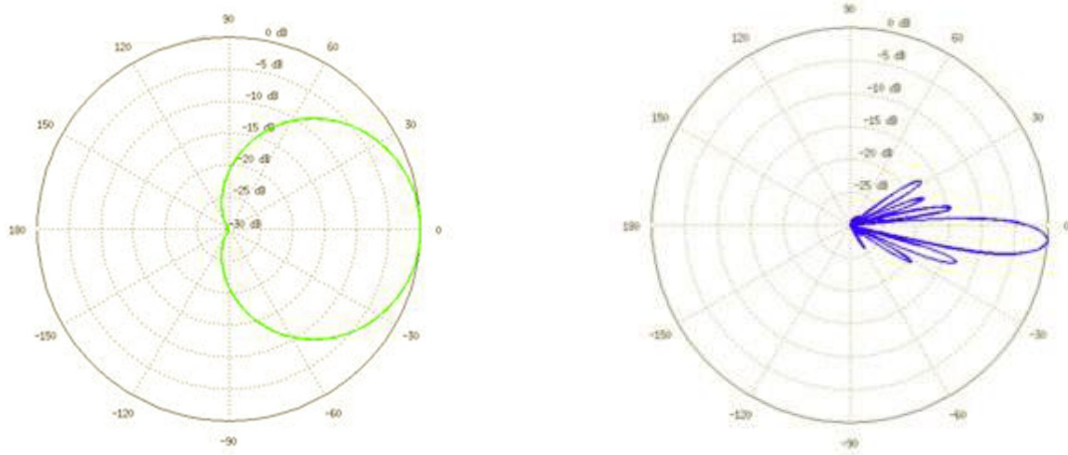
Figure 65. Air Max 2G-16-90 horizontal (left) and vertical (right) antenna patterns (normalized) for horizontal polarization [90].

angles of incidence in azimuth. The combination of the narrow antenna pattern in elevation combined with the narrow RCS response makes it difficult to obtain uniform returns from all targets simultaneously.

It is shown that the match filter in (4.2.8) [46] effectively recovers the correct target profile with a down-range resolution representative of the bandwidth used. The bandwidths of $B = 115$ MHz and $B = 344$ MHz used in the experiment were chosen to accommodate the reduced experimental target area and the limited transmission

110
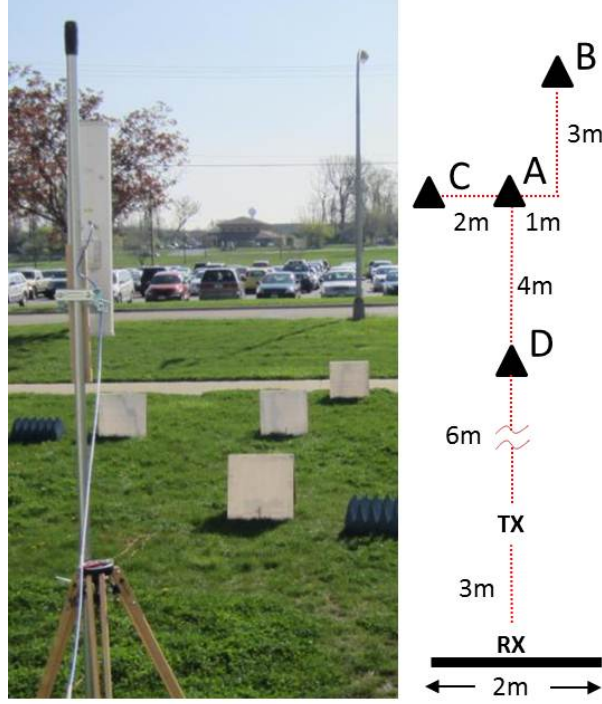
Figure 66. Experimental configuration II: Target array for SAR experiment. Targets are flat aluminum plates with an area of 0.4 m^2. A bandwidth of $B = 344$ MHz is used centered on a $f_c = 2.3$ GHz carrier. Target A is at the center of the scene and the antenna shown is the fixed transmitter.

power. In the context of real passive radar applications, actual WiMAX systems are designed to employ a maximum bandwith of $B = 20$ MHz [63], producing lower resolution profiles. The $B = 20$ MHz bandwidth is most appropriate for large-scale targets such as large aircraft on an airfield or building complexes in the scene.

6.3   Two-Dimensional SAR Images

Configurations II and III shown in Figures 66 and 73 respectively are used to produce SAR imagery using both OFDM and WiMAX pulses. In both configurations Target A defines the center of the scene. The experimental OFDM radar system is used to collect returns from individual transmissions [50]. The receiver antenna is mounted on RAILs linear track, a controllable linear moving track. Four 0.4 m^2 flat

111

plate targets are arranged to exploit the cross-range dimension and oriented to maximize the return energy to the receiving antenna. Configuration II produces a bistatic angle of $\beta = 0$ (measured at the center of the collection) and is used to demonstrate general filter performance and the impact of particular WiMAX features. Configuration III is used to show performance under a larger bistatic angle ($\beta = 100$ degrees) and to validate the OFDM bistatic SAR model. It is of interest to explore the experimental SAR results using the following research concepts: 1) the performance of the AMF and FSMF filters, 2) the impact on SAR of the WiMAX CP and the corresponding subcarrier array, and 3) large bistatic angles.

Filter Performance.

A $B = 344$ MHz bandwidth is employed to scale down the scene, producing a resolution of $\rho_y = 0.5$ meters. The geometry and transmitting center frequency of $f_c = 2.3$ GHz are chosen to produce a similar resolution in cross-range ($\rho_x = 0.3$ meters). A total of 33 pulses are transmitted and their returns collected uniformly over a 2-meter linear span covering approximately 12 degrees of aperture with respect to the scene center.

A 10-symbol, 256-point OFDM waveform is created using random d_n sequences with no preambles or CP. The SAR geometry employed resembles Figure 25 although the receiver and transmitter are at the same height. The center pulse is transmitted at approximately $\phi_T = 0$ degrees and the maximum receiver azimuth ϕ_R is 4.3 degrees at both aperture ends.

The array is radiated with the generic OFDM pulse. The OFDM symbols use

112
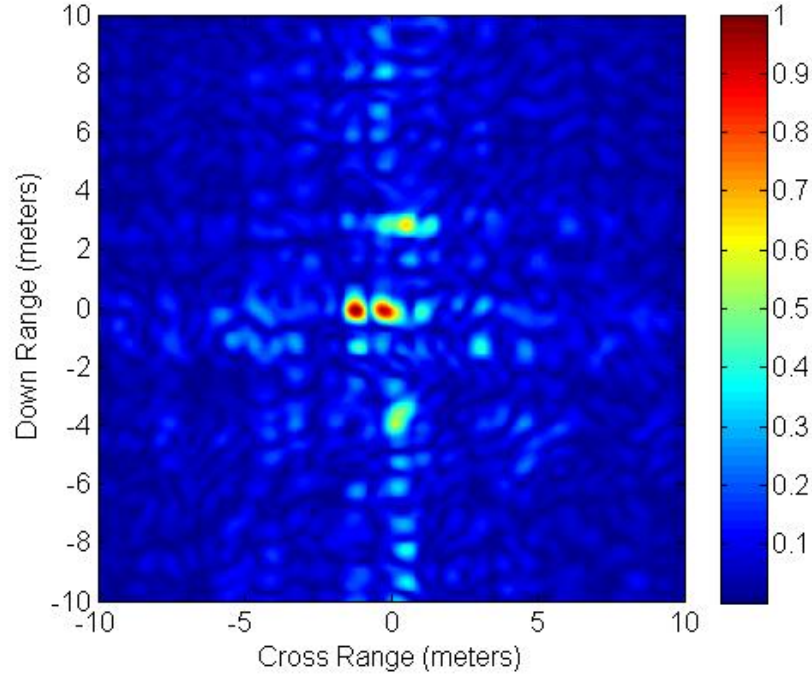
Figure 67. PFA SAR image using a generic 10-symbol 344 MHz OFDM pulse with the FSMF, RSR = 1/1.

all 256 subcarriers forming the complete 344 MHz bandwidth. Figure 67 shows the imaging results for the FSMF using a RSR of 1/1 (using only the first symbol in the sequence). The identification of the targets is clear, however considerable noise can be observed. Increasing the RSR to 10/10 in the FSMF reduces the noise level as can be seen in Figure 68. However the best results are seen in Figure 69 where the AMF is employed averaging the results of all 10 symbols. The reduction in noise is more noticeable along down-range, where the averaging nature of the filter acts. The cross-range noise is not a function of the waveform hence it is not improved.

WiMAX Features.

Next, a 10-symbol WiMAX waveform consisting of two preambles and eight data symbols is used over the same target array. The preambles are generated per [63]

113
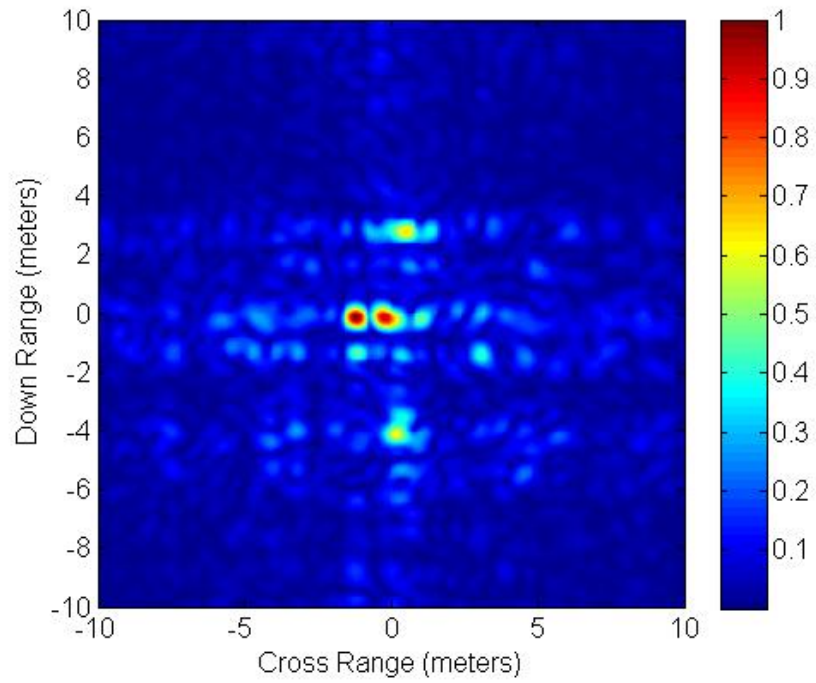
Figure 68. PFA SAR image using a generic 10-symbol 344 MHz OFDM pulse with the FSMF, RSR = 10/10.
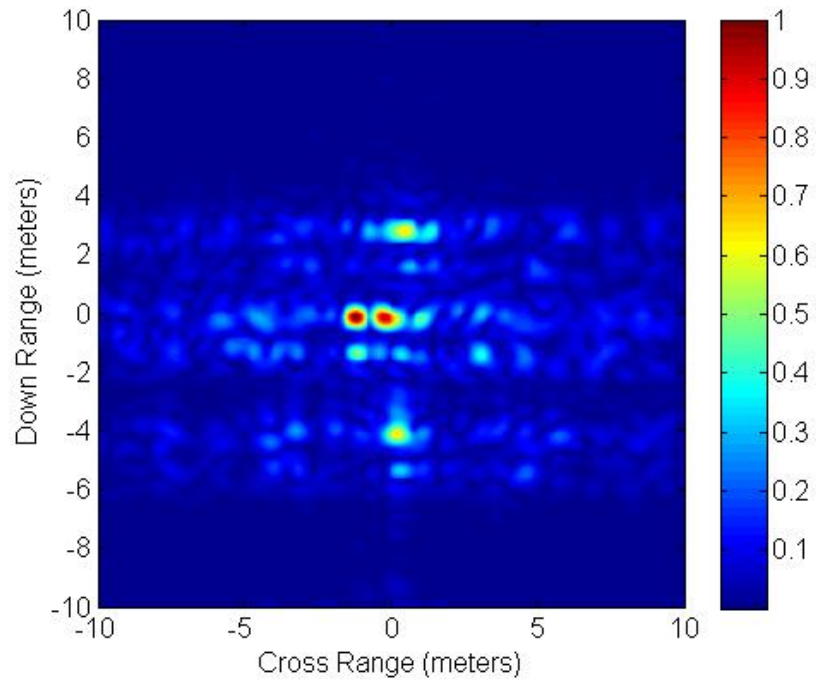
Figure 69. PFA SAR image using a generic 10-symbol 344 MHz OFDM pulse with the AMF, RSR = 1/1.
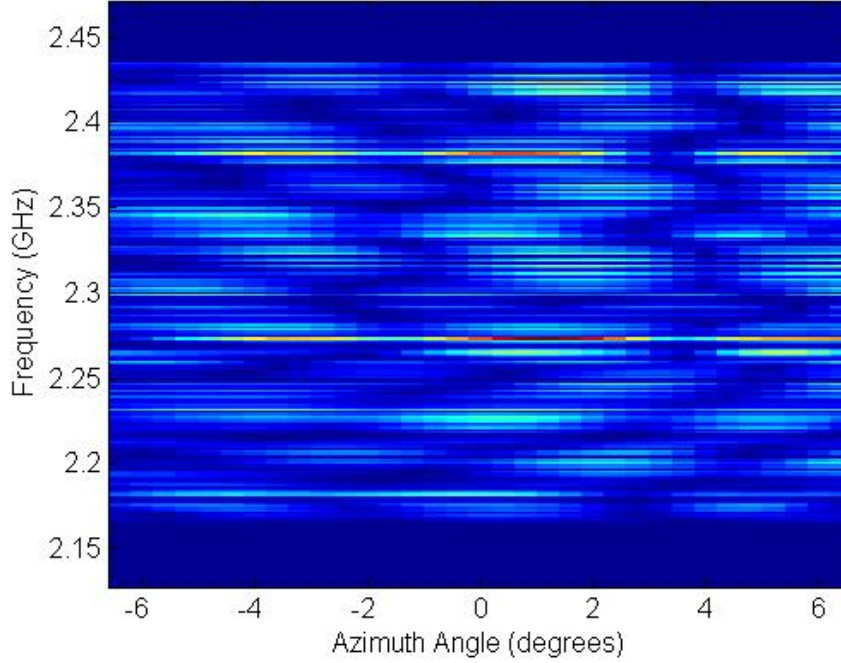
Figure 70. Magnitude of unformatted phase history using a $B = 344$ MHz WiMAX DL subframe (10 symbols). The two-dimensional phase history array was created using our experimental OFDM radar.

while the data symbols are created using random data sequences d_n. All the symbols are modified with the appropriate OFDM PHY features according to the WiMAX standard: null DC carrier, guardbands, pilot subcarriers, and cyclic prefix. The 200 subcarriers used in the WiMAX DL produce a reduced bandwidth of $B = 200*1.34$ KHz $= 269$ MHz.

Figure 70 shows the phase history of the WiMAX collection in frequency versus receiver azimuth (transmitter is stationary). The impact of the WiMAX guardbands to the bandwidth can be clearly seen in the 2.15 GHz and 2.45 GHz regions where no information is present. Although not easily discerned, the WiMAX DC nulling causes the same effect at the 2.3 GHz carrier line.

115

Applying the polar formatting algorithm (PFA) to the phase history results in the image shown in Figure 71. Note that compared to the full OFDM symbol, the difference in down-range resolution is visually negligible (0.4 meters for 344 MHz versus 0.5 meters for 269 MHz), although the targets are not clearly discernible as in the generic OFDM cases. Also, it can be seen that the WiMAX image is shifted in space by approximately 14 meters down-range. This spatial shift is caused by the CP, which introduces a linear phase shift along the subcarrier frequencies. The same phase shift will also degrade down-range phase coherence for off-center targets when re-formatting occurs within the PFA.

Knowledge of the CP duration is sufficient for proper phase correction prior to the PFA. The CP is simply appended to the reference symbols in the match filter. The corrected WiMAX image is shown in Figure 72 where coherence and spatial accuracy are effectively restored. The targets are now easily discerned with magnitudes similar to the generic OFDM waveform case.

Large Bistatic Angles.

Configuration III is shown in Figure 73, where target A again defines the center of the scene. The resulting bistatic angle is $\beta = 100$ degrees. The larger bistatic angle and the scaling of the scene increases the difficulty of acquiring returns experimentally with sufficient SNR, hence the targets are arranged to obtain the best possible SNR with the equipment used. A $B = 344$ MHz bandwidth is employed to scale down the scene with a bistatic down-range resolution of $\rho_y = 0.7$ meters. The geometry and transmitting frequency of $f_c = 2.3$ GHz produce a theoretical bistatic cross-range resolution of $\rho_x = 1.4$ meters. A total of $P = 33$ pulses are transmitted and their
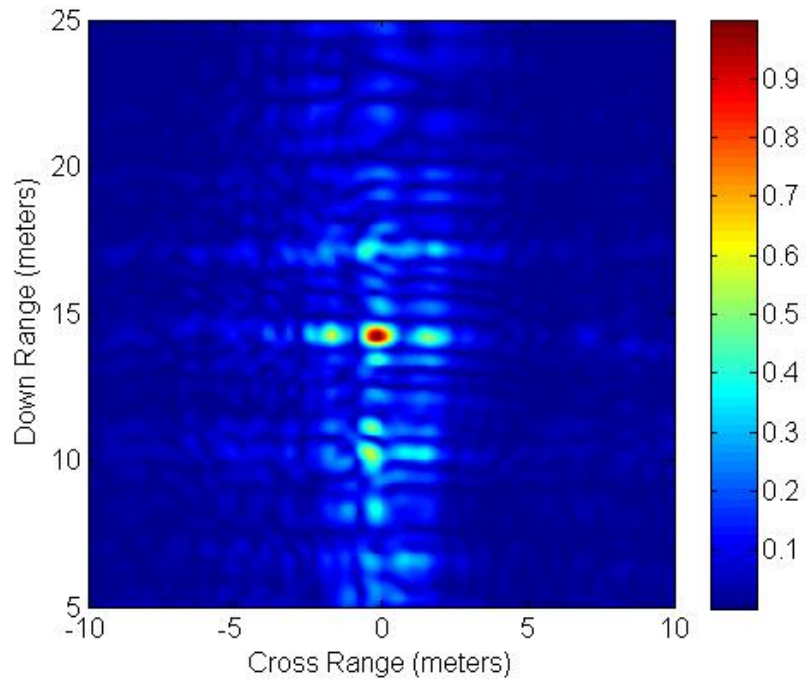
Figure 71. SAR image using a WiMAX 10-symbol DL subframe. Filter used: AMF. The CP shifts the spatial solution in down-range and hinders coherence of off-center targets.
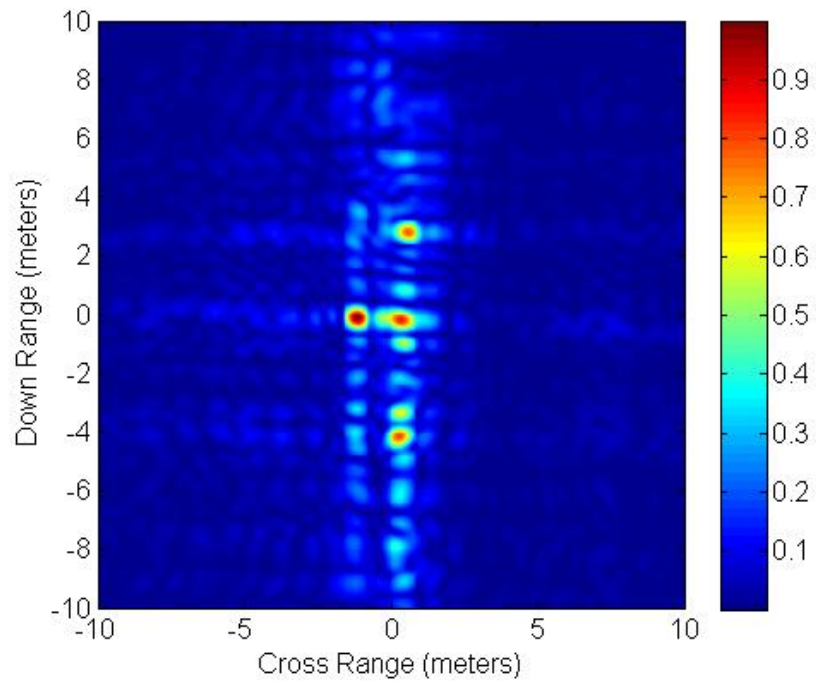
Figure 72. SAR image using a WiMAX 10-symbol DL subframe corrected for the cyclic prefix (CP). Filter used: AMF.

117
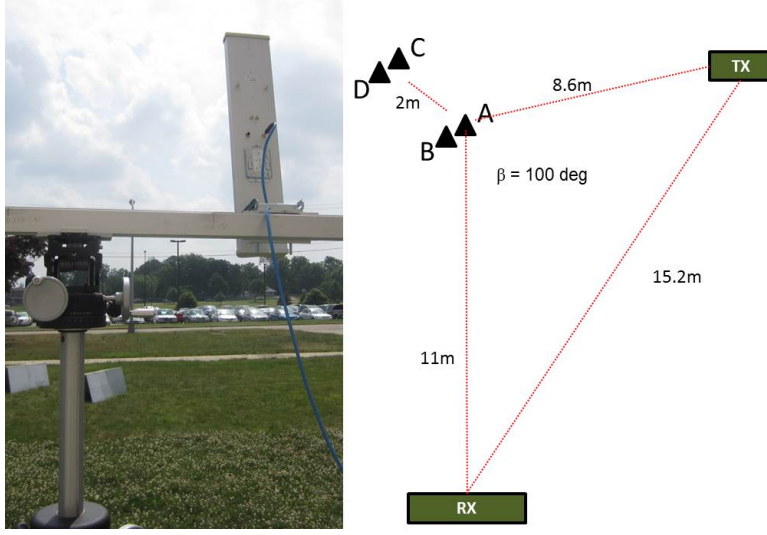
Figure 73. Experimental configuration III: Target array for SAR experiment. Targets are flat aluminum plates with an area of 0.4 m^2. A bandwidth of 344 MHz is used centered on a 2.3 GHz carrier. Target A is at the center of the scene and the antenna shown is the moving receiver.

returns collected uniformly over a 2-meter linear span covering approximately ϕ_R 10 degrees of aperture with respect to the center of the scene. A $\Lambda = 10$-symbol WiMAX waveform consisting of two preambles and eight data symbols is used. The bistatic azimuth aperture is approximately $\phi_b = 4.2$ degrees with the center pulse transmitted at a virtual look angle of $\beta = $ -39 degrees from the horizontal axis.

Figure 74 shows the simulated bistatic SAR for the large bistatic angle. Note the parallel orientation of the four targets with respect to the bistatic LOS in accordance with the model. The SAR image from the collected data is shown in Figure 75. To ensure maximum return energy, the actual targets were set in pairs side-by-side blurring the distinction between them in cross-range. The bistatic down-range dimension is along the bistatic LOS vector with corresponding resolution of approximately 0.7 meters. The cross-range resolution is perpendicular to the down-range and is measured at approximately 1.4 meters. Both resolutions agree with the models in (5.4.18) and (5.4.19). Although these results are not exclusive to OFDM waveforms, the results

118
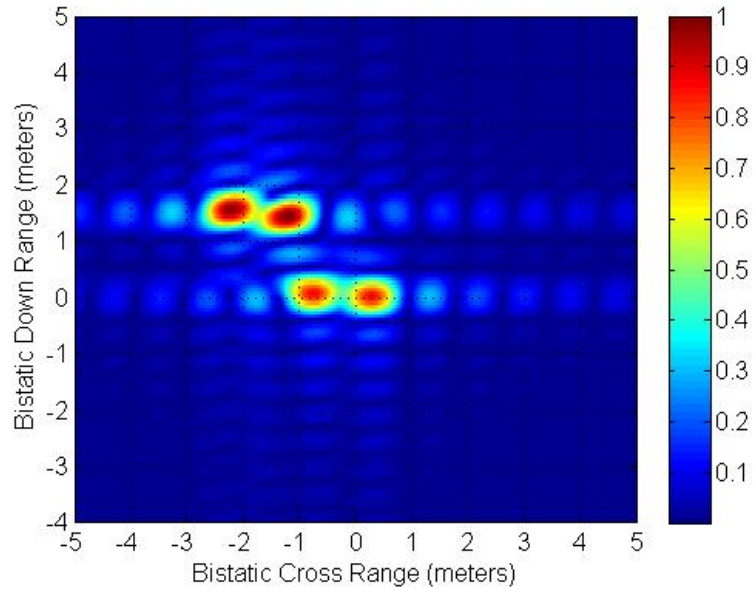
Figure 74. Simulated bistatic SAR image using experimental configuration III.
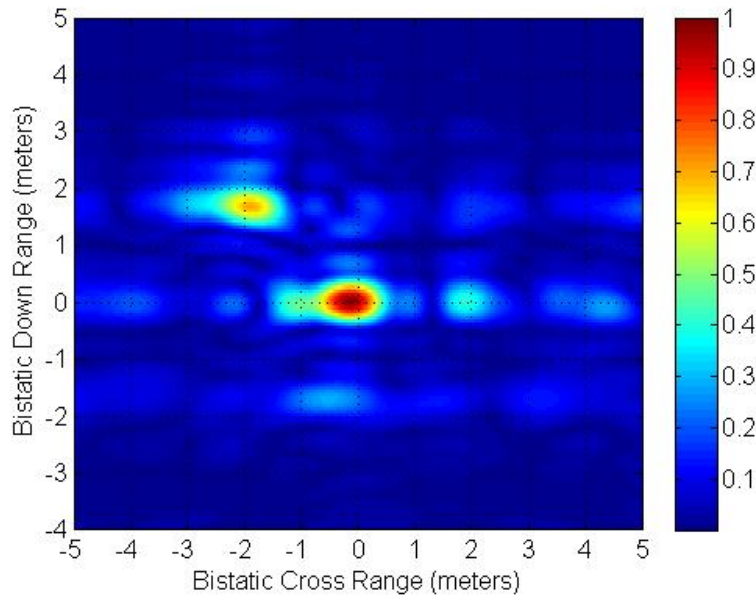
Figure 75. Bistatic SAR image using experimental configuration III. Waveform used is a WiMAX 10-symbol DL subframe corrected for the cyclic prefix (CP).

119

show that even under relatively large bistatic angles, the degradation in resolution is not visually significant, providing the passive radar operator flexibility when planning an imaging collection run.

VII. Conclusion

7.1 Summary

The potential of using commercial OFDM signals for SAR Imaging is evaluated. The research motivation stems from the premise that "range compression" is possible due to the inherent bandwidth in these waveforms. The monostatic and bistatic phase history models are derived for the OFDM-SAR and the solution is used to design signal processing schemes. Using WiMAX as an example of a modern communication network employing OFDM, a collection model is developed which leads to the collection of ground returns for post-processing. These returns are processed into a phase history array using two possible filter designs which exploit in a unique manner exclusive network transmission properties. Experimental data is collected to produce single-dimensional range profiles and two-dimensional SAR images validating the OFDM-SAR phase history models and signal processing concepts.

7.2 Research Conclusion

It is shown that OFDM signals have bandwidth and structured properties that are conducive to the deconvolution of the scene reflectivity function using fast Fourier transforms in match filter operations. Simulated and experimental SAR imagery validates the phase history collection process using both general OFDM and WiMAX-specific waveforms.

WiMAX is selected as a commercial network example to develop notional data collection and signal processing approaches for a passive radar system design. WiMAX follows deployment models used by current 4G and future cellular communication and broadband networks raising its relevance within the research topic. Several WiMAX-

specific features are highlighted in the research as being exploitable for SAR applications. Direct use of WiMAX preamble symbols seems to be a convenient approach to the data collection problem because its data code is known and invariant, it is the first symbol in the downlink (DL) subframes, and its amplitude is 3 dB higher than other DL symbols; however, preamble use produce a smaller sample set limiting the imaging scene size. Another exploitable WiMAX feature is the sequential transmission of data-independent symbols in every WiMAX DL transmission. This enables use of signal processing techniques that can reduce noise levels in the bistatic SAR down-range dimension through averaging. Lastly, the fact that the WiMAX transmitter location is fixed and publicly known, simplifies some bistatic radar models using a single moving platform.

The SAR models and designs developed here for WiMAX are readily extendable to other OFDM networks employing similar transmission schemes (cyclic prefix, guard bands, preambles, etc). Two-way OFDM communication transmissions will most likely employ TDD frame structure where multiple symbols are transmitted sequentially. The OFDM-SAR radar receiver does not need to know what the data means, it only needs to know what it is and the transmission parameters. On the other hand, an OFDM communication network could be designed with built-in features to maximize its use for both communications and radar functions such as ground imaging. The alternatives seem limitless.

7.3   Research Contributions

Although extensive passive radar research exists in terms of target detection and ranging [31,42,43,54] , contributions have been made here in the passive SAR imaging

concepts. Contributions to the field include:

1. Development of the monstatic OFDM range compression (phase history) model and proof-of-concept experiments [46,50].

2. Development of the bistatic OFDM range compression (phase history) model and proof-of-concept experiments [50].

3. Bistatic collection models and practical collection strategies of sectorized tower WiMAX transmissions coupled with airborne receiver platforms [51].

4. Collection and use of the WiMAX Downlink (DL) symbols for radar processing [51].

5. Multi-symbol SAR signal processing designs using WiMAX DL collections [51].

6. Evaluation of specific properties of the WiMAX OFDM physical layer and their impact to SAR imaging performance [47,51].

In addition and as a direct result of this research, the following contributions were made to the AFITs radar instrumentation laboratory:

1. Development of end-to-end simulation tools for proof-of-concept, SAR performance analysis, and future developments using alternative waveforms [49].

2. Development of an experimental radar system for real-time transmission and reception of alternative waveforms [49].

7.4   Recommended Future Research Topics

The complexity of OFDM signals along with the inherent complexities of passive radar processing creates a formidable engineering challenge. Nevertheless, the worldwide deployment of OFDM-based networks offers a unique opportunity of passive

global reach and motivates further research. Future research efforts in this area could include:

1. Multistatic model development of the OFDM passive radar. Develop models to incorporate multiple receivers collecting within a common OFDM communication sector to introduce spatial diversity to the SAR solution.

2. Estimation of OFDM network transmission parameters. This item will help answer the question: How can a non-subscriber (covert operator) intercept and exploit the DL transmission and obtain the necessary parameters for SAR image production?

3. Augment frequency diversity using other systems operating within the same OFDM sectors. For example, a cell phone sector that coincides with WiMAX can be used to augment the phase history data grid. The radar receiver is assumed to be capable of processing both returns independently.

4. Use the uplink (UL) in the WiMAX SAR solution. As a legitimate WiMAX subscriber, a user interacts with the base station via UL bursts which carry user-dependent data and other network requests. Is it possible to transmit controlled UL sequences for the purpose of radar employment?

5. Employing WiMAX OFDMA PHY for mobile communications. The WiMAX OFDM PHY subject in this research is designed for static applications. WiMAX OFDMA PHY on the other hand is designed for mobile applications where Doppler effects must be considered and corrected. In addition, moving users will drive real-time changes in the transmission parameters, raising the complexity of data collection and processing for imaging purposes.

6. The development of advanced processing techniques to exploit other specific

OFDM network features. The filters developed for this research only considered multi-symbol uses to reduce noise in the imaging solution. Other OFDM network features (e.g., cyclic prefix, pilot subcarriers, etc.) could be exploited in a similar manner to either enhance the resulting product or to add flexibility in the collection and processing mechanics.

7. Extend research using other existing 4G commercial networks having similar features, e.g.,LTE variants.

Appendix A. Preamble Code

Table 6. OFDM PHY preamble frequency domain P_{code}. Integers represent subcarriers, complex numbers define the code [63].

-128	0+0i	-96	1-1i	-64	-1-1i	-32	1+1i	0	0+0i	32	-1-1i	64	-1+1i	96	-1-1i
-127	0+0i	-95	1-1i	-63	-1-1i	-31	1+1i	1	-1-1i	33	-1-1i	65	1-1i	97	-1-1i
-126	0+0i	-94	-1+1i	-62	1-1i	-30	-1+1i	2	1+1i	34	-1+1i	66	1+1i	98	1+1i
-125	0+0i	-93	1-1i	-61	-1+1i	-29	1-1i	3	-1+1i	35	1+1i	67	1+1i	99	1-1i
-124	0+0i	-92	1-1i	-60	1-1i	-28	-1+1i	4	-1+1i	36	-1+1i	68	-1+1i	100	1-1i
-123	0+0i	-91	1-1i	-59	1-1i	-27	-1+1i	5	-1-1i	37	-1+1i	69	1-1i	101	0+0i
-122	0+0i	-90	1+1i	-58	-1-1i	-26	1-1i	6	1+1i	38	-1-1i	70	1+1i	102	0+0i
-121	0+0i	-89	-1-1i	-57	1+1i	-25	-1+1i	7	1+1i	39	1+1i	71	1-1i	103	0+0i
-120	0+0i	-88	1+1i	-56	1-1i	-24	1-1i	8	1+1i	40	1+1i	72	1-1i	104	0+0i
-119	0+0i	-87	1+1i	-55	1-1i	-23	1-1i	9	-1-1i	41	1+1i	73	-1-1i	105	0+0i
-118	0+0i	-86	-1-1i	-54	-1+1i	-22	1+1i	10	1+1i	42	-1-1i	74	-1+1i	106	0+0i
-117	0+0i	-85	1+1i	-53	1-1i	-21	-1-1i	11	1-1i	43	1-1i	75	-1+1i	107	0+0i
-116	0+0i	-84	-1-1i	-52	1-1i	-20	-1-1i	12	1-1i	44	1-1i	76	-1+1i	108	0+0i
-115	0+0i	-83	-1-1i	-51	1-1i	-19	-1-1i	13	1-1i	45	1+1i	77	1+1i	109	0+0i
-114	0+0i	-82	1-1i	-50	1+1i	-18	-1+1i	14	-1+1i	46	-1-1i	78	-1-1i	110	0+0i
-113	0+0i	-81	-1+1i	-49	-1-1i	-17	1-1i	15	-1+1i	47	1-1i	79	-1-1i	111	0+0i
-112	0+0i	-80	1-1i	-48	1+1i	-16	-1-1i	16	-1+1i	48	1-1i	80	1-1i	112	0+0i
-111	0+0i	-79	1-1i	-47	1+1i	-15	-1-1i	17	-1+1i	49	-1+1i	81	-1-1i	113	0+0i
-110	0+0i	-78	-1-1i	-46	-1-1i	-14	1+1i	18	1-1i	50	-1-1i	82	-1+1i	114	0+0i
-109	0+0i	-77	1+1i	-45	1+1i	-13	-1-1i	19	-1-1i	51	-1+1i	83	-1-1i	115	0+0i
-108	0+0i	-76	1-1i	-44	-1-1i	-12	-1-1i	20	-1-1i	52	-1+1i	84	1-1i	116	0+0i
-107	0+0i	-75	1-1i	-43	-1-1i	-11	-1-1i	21	-1+1i	53	1+1i	85	1-1i	117	0+0i
-106	0+0i	-74	-1+1i	-42	1-1i	-10	1-1i	22	1-1i	54	1-1i	86	-1+1i	118	0+0i
-105	0+0i	-73	1-1i	-41	-1+1i	-9	-1+1i	23	1+1i	55	1-1i	87	-1+1i	119	0+0i
-104	0+0i	-72	1-1i	-40	1+1i	-8	1-1i	24	1+1i	56	1-1i	88	-1+1i	120	0+0i
-103	0+0i	-71	1-1i	-39	1+1i	-7	1-1i	25	-1+1i	57	-1-1i	89	1-1i	121	0+0i
-102	0+0i	-70	1+1i	-38	1-1i	-6	-1+1i	26	1-1i	58	1+1i	90	-1+1i	122	0+0i
-101	0+0i	-69	-1-1i	-37	-1+1i	-5	1-1i	27	1-1i	59	1+1i	91	1+1i	123	0+0i
-100	1-1i	-68	1+1i	-36	1+1i	-4	-1+1i	28	-1-1i	60	-1+1i	92	1+1i	124	0+0i
-99	1-1i	-67	1+1i	-35	1+1i	-3	-1+1i	29	1+1i	61	1-1i	93	1+1i	125	0+0i
-98	-1-1i	-66	-1-1i	-34	-1-1i	-2	-1-1i	30	1-1i	62	-1+1i	94	-1-1i	126	0+0i
-97	1+1i	-65	1+1i	-33	1+1i	-1	1+1i	31	-1-1i	63	-1+1i	95	-1-1i	127	0+0i

$$P1 = \begin{cases} \sqrt{2}\sqrt{2}\ \mathrm{conj}(P_{code}(k)) & \text{for } k_{mod4} = 0 \\ 0 & \text{for } k_{mod4} \neq 0 \end{cases} \qquad (1.0.1)$$

$$P2 = \begin{cases} \sqrt{2}\ \mathrm{conj}(P_{code}(k)) & \text{for } k_{mod2} = 0 \\ 0 & \text{for } k_{mod2} \neq 0 \end{cases} \qquad (1.0.2)$$

Bibliography

[1] Almohammad, A. and G. Ghinea. "Stego image quality and the reliability of PSNR". *Image Processing Theory Tools and Applications (IPTA), 2010 2nd International Conference on*, 215 –220. July 2010.

[2] Bahai, A., B. Saltzberg, and M. Ergen. *Multi-Carrier Digital Communications, Theory and Applications*. Springer Science, New York, 2004.

[3] Berger, C.R., B. Demissie, J. Heckenbach, P. Willett, and Shengli Zhou. "Signal Processing for Passive Radar Using OFDM Waveforms". *Selected Topics in Signal Processing,IEEE Journal of*, 4(1):226–238, 2010.

[4] Berger, C.R., Shengli Zhou, and P. Willett. "Signal extraction using Compressed Sensing for passive radar with OFDM signals". *Information Fusion, 2008 11th International Conference on*. 30 2008.

[5] Bongioanni, C., F. Colone, D. Langellotti, P. Lombardo, and T. Bucciarelli. "A new approach for DVB-T Cross-Ambiguity Function evaluation". *Radar Conference, 2009. EuRAD 2009. European*, 37–40. 2009.

[6] Bongioanni, C., F. Colone, and P. Lombardo. "Performance analysis of a multifrequency FM based Passive Bistatic Radar". *Radar Conference, 2008. RADAR '08. IEEE*, 1–6. 2008.

[7] Braun, M., C. Sturm, and F.K. Jondral. "Maximum likelihood speed and distance estimation for OFDM radar". *Radar Conference, 2010 IEEE*, 256–261. May 2010.

[8] Brito, A. E., S. H. Chan, and S. D. Cabrera. "SAR image formation using 2D reweighted minimum norm extrapolation". E. G. Zelnio (editor), *Society of Photo-Optical Instrumentation Engineers (SPIE) Conference Series*, volume 3721 of *Presented at the Society of Photo-Optical Instrumentation Engineers (SPIE) Conference*, 78–91. August 1999.

[9] Cabrera, S., B. Flores, and G Thomas. "Application of one-dimensional adaptive extrapolation to improve resolution in range-Doppler imaging". *Society of Photo-Optical Instrumentation Engineers (SPIE) Conference Series*, volume 2230 of *Presented at the Society of Photo-Optical Instrumentation Engineers (SPIE) Conference*, 135–145. 1994.

[10] Cabrera, S. and T.W. Parks. "Extrapolation and spectral estimation with iterative weighted norm modification". *Signal Processing, IEEE Transactions on*, 39(4):842 –851, April 1991.

[11] Cardinali, R., F. Colone, C. Ferretti, and P. Lombardo. "Comparison of Clutter and Multipath Cancellation Techniques for Passive Radar". *Radar Conference, 2007 IEEE*, 469–474. 2007.

[12] Carrara, W., R. Goodman, and R. Majewski. *Spotlight synthetic aperture radar: signal processing algorithms.* Artec House, Boston, 1995.

[13] Carson, Steven, Daniel Kilfoyle, Michael Potter, and James Vance. "A passive, multi-static radar system". *Radar Systems, 2007 IET International Conference on*, 1–4. 2007.

[14] Cazzani, L., C. Colesanti, D. Leva, G. Nesti, C. Prati, F. Rocca, and D. Tarchi. "A ground-based parasitic SAR experiment". *Geoscience and Remote Sensing, IEEE Transactions on*, 38(5):2132–2141, 2000.

[15] Cetin, M. and W. C. Karl. "Feature-enhanced synthetic aperture radar image formation based on nonquadratic regularization". *Image Processing, IEEE Transactions on*, 10(4):623–631, 2001.

[16] Cetin, M. and A. D. Lanterman. "Region-enhanced passive radar imaging". *Radar, Sonar and Navigation, IEE Proceedings* -, 152(3):185–194, 2005.

[17] Cetin, M. and R. L. Moses. "Synthetic Aperture Radar Imaging from Wide-Angle Data with Frequency-Band Omissions". *Signal Processing and Communications Applications, 2006 IEEE 14th*, 1–4. 2006.

[18] Changchang, Liu, Xu Hao, He Xuezhi, and Chen Weidong. "The distributed passive radar 3-D imaging and analysis in wavenumber domain". *Signal Processing (ICSP), 2010 IEEE 10th International Conference on*, 2051 –2054. 2010.

[19] Cherniakov, M., F. Colone, C. J. Baker, D. O'Hagan, H. Griffiths, D. Gould, P. Tittensor, C. Sarno, R. Pollard, M. Isohookana, N. Morrison, R. Lord, M. R. Inggs, A. Benavoli, A. D. Lallo, A. Farina, R. Fulcoli, R. Mancinelli, L. Timmoneri, L. Chisci, and R. Cardinali. "Oral Session 10a: Passive Radar". *Radar Systems, 2007. RADAR 2007. The Institution of Engineering and Technology International Conference on*, 74–75. 2007.

[20] Chetty, K., K. Woodbridge, Hui Guo, and G. E. Smith. "Passive bistatic WiMAX radar for marine surveillance". *Radar Conference, 2010 IEEE*, 188–193. 2010.

[21] Colone, F., R. Cardinali, and P. Lombardo. "Cancellation of clutter and multipath in passive radar using a sequential approach". *Radar, 2006 IEEE Conference on*, 7 pp. 2006.

[22] Colone, F., R. Cardinali, P. Lombardo, O. Crognale, A. Cosmi, A. Lauri, and T. Bucciarelli. "Space-time constant modulus algorithm for multipath removal

on the reference signal exploited by passive bistatic radar". *Radar, Sonar & Navigation, IET*, 3(3):253–264, 2009.

[23] Colone, F., P. Falcone, and P. Lombardo. "Ambiguity Function analysis of WiMAX transmissions for passive radar". *Radar Conference, 2010 IEEE*, 689–694. 2010.

[24] Colone, F., D. W. O'Hagan, P. Lombardo, and C. J. Baker. "A Multistage Processing Algorithm for Disturbance Removal and Target Detection in Passive Bistatic Radar". *Aerospace and Electronic Systems, IEEE Transactions on*, 45(2):698–722, 2009.

[25] Cristallini, D., M. Caruso, P. Falcone, D. Langellotti, C. Bongioanni, F. Colone, S. Scafe, and P. Lombardo. "Space-based passive radar enabled by the new generation of geostationary broadcast satellites". *Aerospace Conference, 2010 IEEE*, 1–11. 2010.

[26] DeGraaf, S.R. "SAR imaging via modern 2-D spectral estimation methods". *Image Processing, IEEE Transactions on*, 7(5):729 –761, May 1998.

[27] Doren, N.E., Jr. Jakowatz, C.V., D.E. Wahl, and P.A. Thompson. "General formulation for wavefront curvature correction in polar-formatted spotlight-mode SAR images using space-variant post-filtering". *Image Processing, 1997. Proceedings., International Conference on*, volume 1, 861 –864 vol.1. October 1997.

[28] Ergen, M. *Mobile Broadband, Including WiMAX and LTE.* Springer Science plus Business Media, New York, 2009.

[29] Fabrizio, G., F. Colone, P. Lombardo, and A. Farina. "Passive radar in the high frequency band". *Radar Conference, 2008. RADAR '08. IEEE*, 1–6. 2008.

[30] Fabrizio, G., F. Colone, P. Lombardo, and A. Farina. "Adaptive beamforming for high-frequency over-the-horizon passive radar". *Radar, Sonar & Navigation, IET*, 3(4):384–405, 2009.

[31] Falcone, P., F. Colone, C. Bongioanni, and P. Lombardo. "Experimental results for OFDM WiFi-based passive bistatic radar". *Radar Conference, 2010 IEEE*, 516–521. 2010.

[32] Flood, J.E. *Telecommunication Networks, 2ed.* The Institution of Electical Engineers, London, 1997.

[33] Franken, G.E.A., H. Nikookar, and P. van Genderen. "Doppler Tolerance of OFDM-coded Radar Signals". *Radar Conference, 2006. EuRAD 2006. 3rd European*, 108 –111. 2006.

[34] Freeman, D. "The Silent Sentry System". *AoC 5th Multinational Conference of Passive Covert Radar.* 2007.

[35] Garmatyuk, D. and M. Brenneman. "Slow-time SAR signal processing for UWB OFDM radar system". *Radar Conference, 2010 IEEE*, 853–858. 2010.

[36] Garmatyuk, D. and K. Kauffman. "Radar and data communication fusion with UWB-OFDM software-defined system". *Ultra-Wideband, 2009. ICUWB 2009. IEEE International Conference on.* 2009.

[37] Garmatyuk, D. and J. Schuerger. "Conceptual design of a dual-use radar/communication system based on OFDM". *Military Communications Conference, 2008. MILCOM 2008. IEEE*, 1 –7. 2008.

[38] Garmatyuk, D., J. Schuerger, K. Kauffman, and S. Spalding. "Wideband OFDM system for radar and communications". *Radar Conference, 2009 IEEE*, 1 –6. May 2009.

[39] Garmatyuk, D. S. "Simulated Imaging Performance of UWB SAR Based on OFDM". *Ultra-Wideband, The 2006 IEEE 2006 International Conference on*, 237–242. 2006.

[40] Garmatyuk, Dmitriy, Yu Morton, and Xiaolei Mao. "Radar and GPS System Inter-Operability with UWB-OFDM Signals". *Aerospace and Electronic Systems, IEEE Transactions on*, 47(1):265 –274, 2011.

[41] Garmatyuk, D.S. and R.M. Narayanan. "SAR imaging using fully random bandlimited signals". *Antennas and Propagation Society International Symposium, 2000. IEEE.* 2000.

[42] Griffiths, H. D. and C. J. Baker. "Passive coherent location radar systems. Part 1: performance prediction". *Radar, Sonar and Navigation, IEE Proceedings -*, 152; 152(3):153–159, 2005.

[43] Griffiths, H. D., C. J. Baker, and I. Papoutsis. "Passive coherent location radar systems. Part 2: waveform properties". *Radar, Sonar and Navigation, IEE Proceedings -*, 152; 152(3):160–168, 2005.

[44] Guner, A, M. Temple, and R.L. Claypool. "Direct-path filtering of DAB waveform from PCL receiver target channel." *IET Electronic Letters*, 39(1), Jan 2003.

[45] Guner, Abdulkadir. "Ambiguity Function Analysis and Direct-Path Signal Filtering of the Digital Audio Broadcast (DAB) Waveform for Passive Coherent Location (PCL)", 2002.

[46] Gutierrez del Arroyo, J. and J. Jackson. "SAR Imaging Using WiMAX OFDM PHY". *2011 IEEE Radar Conference*, 129–134. 2011.

[47] Gutierrez del Arroyo, J., J. Jackson, and M. Temple. "WiMAX Ambigutity Function for PCL Systems". *NAECON Conference in Dayton, OH, 2009 IEEE.* 2009.

[48] Gutierrez del Arroyo, J. and J. A. Jackson. "Passive SAR Imaging Using Commercial OFDM Networks". *2011 MSS Tri-Service Radar Symposium.* 2011.

[49] Gutierrez del Arroyo, J. and J. A. Jackson. "Range Profiles from an Experimental OFDM Passive Radar". *International Waveform Diversity and Design Conference.* 2012.

[50] Gutierrez del Arroyo, J. and J. A. Jackson. "WiMAX OFDM for Active and Passive SAR Ground Imaging". *IEEE Aerospace and Electronic Systems Society (AESS)*, Accepted for publication, 2012.

[51] Gutierrez del Arroyo, J. and J. A. Jackson. "Signal Processing for SAR Ground Imaging using WiMAX Communication Networks". *IEEE Aerospace and Electronic Systems Society (AESS)*, Submitted Jul 2012, pending acceptance.

[52] Herman, M. and T. Strohmer. "Compressed sensing radar". *Radar Conference, 2008. RADAR '08. IEEE*, 1 –6. May 2008.

[53] Herman, M.A. and T. Strohmer. "High-Resolution Radar via Compressed Sensing". *Signal Processing, IEEE Transactions on*, 57(6):2275 –2284, 2009.

[54] Howland, P. E. "Target tracking using television-based bistatic radar". *Radar, Sonar and Navigation, IEE Proceedings*, 146; 146(3):166–174, 1999.

[55] Jackson, M.C. "The geometry of bistatic radar systems". *Communications, Radar and Signal Processing, IEE Proceedings F*, 133(7):604 –612, 1986.

[56] Jain, A. and S. Ranganath. "Extrapolation algorithms for discrete signals with application in spectral estimation". *Acoustics, Speech and Signal Processing, IEEE Transactions on*, 29(4):830 – 845, August 1981.

[57] Jakowatz, Charles V., Daniel E. Wahl, Paul H. Eichel, Dennis C. Ghiglia, and Paul A. Thompson. *Spotlight-mode synthetic aperture radar : a signal processing approach.* Kluwer Academic Publishers, Boston, 1996.

[58] Jun, Wang, Zhang Xinwen, and Bao Zheng. "Passive Radar Imaging Algorithm Based on Subapertures Synthesis of Multiple Television Stations". *Radar, 2006. CIE '06. International Conference on*, 1 –4. 2006.

[59] Kauffman, K., D. Garmatyuk, and J. Morton. "Efficient sparse target tracking algorithm for navigation with UWB-OFDM radar sensors". *Aerospace Electronics Conference (NAECON), Proceedings of the IEEE 2009 National*, 14 –17. 2009.

[60] Khomchuk, P., I. Bilik, and D.P. Kasilingam. "Compressive sensing-based SAR tomography". 354 –358. may. 2010.

[61] Kragh, T.J. and A.A. Kharbouch. "Monotonic Iterative Algorithms for SAR Image Restoration". *Image Processing, 2006 IEEE International Conference on*, 645 –648. 2006.

[62] Kuschel, H. and D. O'Hagan. "Passive radar from history to future". *Radar Symposium (IRS), 2010 11th International*, 1 –4. 2010.

[63] LAN/MAN Standards Committee. "IEEE Standard for Local and Metropolitan Area Networks. Part 16: Air Interface for Fixed Broadband Wireless Access Systems", 2002.

[64] Lanterman, Aaron D. and D.C. Munson. "Deconvolution techniques for passive radar imaging". *Algorithms for Synthetic Aperture Radar IX(Proceedings)*, volume 4727, 166–177. August 2002.

[65] Lei, Zhu and Qiu Chunting. "Application of compressed sensing theory to radar signal processing". *Computer Science and Information Technology (ICCSIT), 2010 3rd IEEE International Conference on*, volume 6, 315 –318. 2010.

[66] Levanon, N. "Multifrequency complementary phase-coded radar signal". *Radar, Sonar and Navigation, IEE Proceedings -*, 147(6):276 –284, December 2000.

[67] Levanon, Nadav and Eli Mozeson. *Radar signals*. J. Wiley, Hoboken, NJ, 2004.

[68] Li, Gang, Jia Xu, Ying-Ning Peng, and Xiang-Gen Xia. "Bistatic Linear Antenna Array SAR for Moving Target Detection, Location, and Imaging With Two Passive Airborne Radars". *Geoscience and Remote Sensing, IEEE Transactions on*, 45(3):554 –565, 2007.

[69] Liu, Kuang-Hung and D.C. Munson. "Autofocus in multistatic passive SAR imaging". *Acoustics, Speech and Signal Processing, 2008. ICASSP 2008. IEEE International Conference on*. 31 2008.

[70] Loffeld, O., H. Nies, V. Peters, and S. Knedlik. "Models and useful relations for bistatic SAR processing". *Geoscience and Remote Sensing Symposium, 2003. IGARSS '03. Proceedings. 2003 IEEE International*, volume 3, 1442–1445. 2003.

[71] Loffeld, O., H. Nies, V. Peters, and S. Knedlik. "Models and useful relations for bistatic SAR processing". *Geoscience and Remote Sensing, IEEE Transactions on*, 42(10):2031–2038, 2004.

[72] Ma, Pengge, Lin Qi, Enqing Chen, and Ning Zheng. "Navigation Satellite Passive Radar Moving Target Detection and SAR Imaging Based on FRFT". *Pervasive Computing Signal Processing and Applications (PCSPA), 2010 First International Conference on*, 767 –770. 2010.

132

[73] Matthes, D. "Convergence of ESM sensors and passive covert radar". *Radar Conference, 2005 IEEE International*, 430 – 44. May 2005.

[74] Ong, E. "WiMAX gains momentum across AsiaPac and the rest of the world". *Manila Bulletin Publishing Corporation*, 2010.

[75] Oppenheim, Alan and Ronald Schafer. *Discrete-Time Signal Processing*. Pearson, Upper Saddle, NJ, 2010.

[76] Potter, L. C., E. Ertin, J. T. Parker, and M. Cetin. "Sparsity and Compressed Sensing in Radar Imaging". *Proceedings of the IEEE*, 98(6), 2010.

[77] Radon, J. "On linear functional transformations and functional equations". *Uspekhi Mat. Nauk*, 1:200–227, 1936.

[78] Rigling, B. D. and R. L. Moses. "Polar format algorithm for bistatic SAR". *Aerospace and Electronic Systems, IEEE Transactions on*, 40(4):1147–1159, 2004.

[79] Roca, Amalia. *Implementation of a WiMAX Simulator in Simulink*. 2007. Internet: www.nt.tuwien.ac.at.

[80] Schuerger, J. and D. Garmatyuk. "Performance of random OFDM radar signals in deception jamming scenarios". *Radar Conference, 2009 IEEE*, 1 –6. May 2009.

[81] Si, Xiaoyun, Licheng Jiao, Hang Yu, Dongdong Yang, and Hongxiao Feng. "SAR images reconstruction based on Compressive Sensing". oct. 2009.

[82] Simpson, R.A. "Spacecraft studies of planetary surfaces using bistatic radar". *Geoscience and Remote Sensing, IEEE Transactions on*, 31(2):465 –482, March 1993.

[83] Soumekh, Mehrdad. *Synthetic Aperture Radar Signal Processing with MATLAB Algorithms*. Wiley-Interscience, 1999.

[84] Sturm, C., E. Pancera, T. Zwick, and W. Wiesbeck. "A novel approach to OFDM radar processing". *Radar Conference, 2009 IEEE*, 1–4. 2009.

[85] Sturm, C., T. Zwick, W. Wiesbeck, and M. Braun. "Performance verification of symbol-based OFDM radar processing". *Radar Conference, 2010 IEEE*, 60–63. 2010.

[86] Sullivan, Roger J. *Radar foundations for imaging and advanced concepts*. Scitech Publishing, Raleigh, NC, 2000.

[87] Suwa, K. and M. Iwamoto. "A Two-Dimensional Bandwidth Extrapolation Technique for Polarimetric Synthetic Aperture Radar Images". *Geoscience and Remote Sensing, IEEE Transactions on*, 45(1):45 –54, 2007.

[88] Suwa, K., S. Nakamura, S. Morita, T. Wakayama, H. Maniwa, T. Oshima, R. Maekawa, S. Matsuda, and T. Tachihara. "ISAR imaging of an aircraft target USING ISDB-T digital TV based passive bistatic radar". *Geoscience and Remote Sensing Symposium (IGARSS), 2010 IEEE International*, 4103 –4105. 2010.

[89] Tsao, T., M. Slamani, P. Varshney, D. Weiner, H. Schwarzlander, and S. Borek. "Ambiguity function for a bistatic radar". *Aerospace and Electronic Systems, IEEE Transactions on*, 33(3):1041–1051, 1997.

[90] UBIQUTI Networks Inc. "AirMax 2.4GHz Sector Antenna Datasheet." August 2012. Internet: http://dl.ubnt.com.

[91] Unknown. "The HA100 passive radar from Thales to play a role in protecting the flypast on 14th July in Paris". July 2010. Internet: http://www.thalesgroup.com/Pages/PressRelease.aspx?id=13287.

[92] Unknown. "WiMAX Forum Monthly Industry Report". February 2011. Internet: www.wimaxforum.org.

[93] Wang, Ling and Yacizi B. "Passive radar imaging of moving targets with sparsely distributed receivers". *Sensor Array and Multichannel Signal Processing Workshop (SAM), 2010 IEEE*, 257 –260. 2010.

[94] Wang, Qing, Chunping Hou, and Yilong Lu. "WiMAX signal generation based on MIMO-OFDM testbed for passive radar application". *Industrial Electronics and Applications, 2009. ICIEA 2009. 4th IEEE Conference on*, 2582 –2587. May 2009.

[95] Wang, Qing, Chunping Hou, and Yilong Lu. "WiMAX signal waveform analysis for passive radar application". *International Radar Conference - Surveillance for a Safer World*, 1–6. October 2009.

[96] Wang, Qing, Yilong Lu, and Chunping Hou. "An experimental WiMAX based passive radar study". *Microwave Conference, 2009. APMC 2009. Asia Pacific*, 1204–1207. 2009.

[97] Westra, Arend G. "Radar versus Stealth, Passive Radar and the Future of U.S. Military Power". *Joint Force Quarterly*, 4th Quarter(55):136, 2009.

[98] Willis, Nicholas J. and H. Griffiths. *Advances in bistatic radar*. SciTech Pub., Raleigh, NC, 2007.

[99] Wu, Yong and Jr. Munson, D.C. "Multistatic passive radar imaging using the smoothed pseudo Wigner-Ville distribution". *Image Processing, 2001. Proceedings. 2001 International Conference on*. 2001.

[100] Wu, Yong and Jr Munson, D.C. "Wide-angle ISAR passive imaging using smoothed pseudo Wigner-Ville distribution". *Radar Conference, 2001. Proceedings of the 2001 IEEE*. 2001.

[101] Wuming, Hu and Wang Jun. "Airborne SAR passive radar imaging algorithm based on external illuminator". *Synthetic Aperture Radar, 2007. APSAR 2007. 1st Asian and Pacific Conference on*, 642 –645. 2007.

[102] Xuezhi, He, Xu Hao, Liu Changchang, Wang Dongjin, and Chen Weidong. "A new approach to distributed passive radar imaging by 2-D NUFFT". *Signal Processing (ICSP), 2010 IEEE 10th International Conference on*, 2067 –2070. 2010.

[103] Yacizi, B. and I.Y Son. "Passive Imaging using Distributed Apertures in Multiple Scattering Environments". *Inverse Problems*, 26, 2010. ID: 065002.

[104] Yan, Li, Wang Jun, and Liu Jinrong. "ESPRIT super-resolution imaging algorithm based on external illuminators". *Synthetic Aperture Radar, 2007. APSAR 2007. 1st Asian and Pacific Conference on*, 232 –235. 2007.

[105] Yarman, C. E. and B. Yazici. "Synthetic Aperture Hitchhiker Imaging". *Image Processing, IEEE Transactions on*, 17(11):2156–2173, 2008.

[106] Yarman, C. E., B. Yazici, and M. Cheney. "Bistatic Synthetic Aperture Hitchhiker Imaging". *Acoustics, Speech and Signal Processing, 2007. ICASSP 2007. IEEE International Conference on*, volume 1, I–537–I–540. 2007.

[107] Yarman, C.E., Ling Wang, and B. Yazici. "Passive synthetic aperture radar imaging with single frequency sources of opportunity". *Radar Conference, 2010 IEEE*, 949 –954. May 2010.

[108] Zatman, M. "How narrow is narrowband?" *Radar, Sonar and Navigation, IEE Proceedings -*, 145(2):85 –91, April 1998.

[109] Zhang, P. and Ruliang Yang. "A New Superresolution SAR Imaging Algorithm based on Extrapolation". *Geoscience and Remote Sensing Symposium, 2008. IGARSS 2008. IEEE International*, volume 4, IV –407 –IV –410. 2008.

REPORT DOCUMENTATION PAGE

Form Approved
OMB No. 0704-0188

1. REPORT DATE *(DD-MM-YYYY)*	2. REPORT TYPE	3. DATES COVERED *(From - To)*
13-09-2012	Dissertation	17-08-2009 to 13-09-2012

4. TITLE AND SUBTITLE

Passive Synthetic Aperture Radar Imaging Using Commercial OFDM Communication Networks

5a. CONTRACT NUMBER

5b. GRANT NUMBER

5c. PROGRAM ELEMENT NUMBER

6. AUTHOR(S)

Gutierrez del Arroyo, Jose R., Maj

5d. PROJECT NUMBER

12G219

5e. TASK NUMBER

5f. WORK UNIT NUMBER

7. PERFORMING ORGANIZATION NAME(S) AND ADDRESS(ES)

Air Force Institute of Technology
Graduate School of Engineering and Management (AFIT/EN)
2950 Hobson Way
Wright-Patterson AFB OH 45433-7765

8. PERFORMING ORGANIZATION REPORT NUMBER

AFIT/DEE/ENG/12-10

9. SPONSORING / MONITORING AGENCY NAME(S) AND ADDRESS(ES)

Air Force Research Laboratory, Sensors Directorate
Attn: Dr. Alan D. Kerrick
2241 Avionics Circle, Area B, B620
Wright Patterson AFB, OH 45433
DSN: 798-4350 Alan.Kerrick@wpafb.af.mil

10. SPONSOR/MONITOR'S ACRONYM(S)

AFRL/RYMRA

11. SPONSOR/MONITOR'S REPORT NUMBER(S)

12. DISTRIBUTION / AVAILABILITY STATEMENT

Distribution A. Approved for Public Release; Distribution Unlimited.

13. SUPPLEMENTARY NOTES

This material is declared a work of the U.S. Government and is not subject to copyright protection in the United States.

14. ABSTRACT

Modern communication systems provide myriad opportunities for passive radar applications. OFDM is a popular waveform used widely in wireless communication networks today. Understanding the structure of these networks becomes critical in future passive radar systems design and concept development. This research develops collection and signal processing models to produce passive SAR ground images using OFDM communication networks. The OFDM-based WiMAX network is selected as a relevant example and is evaluated as a viable source for radar ground imaging. The monostatic and bistatic phase history models for OFDM are derived and validated with experimental single dimensional data. An airborne passive collection model is defined and signal processing approaches are proposed providing practical solutions to passive SAR imaging scenarios. Finally, experimental SAR images using general OFDM and WiMAX waveforms are shown to validate the overarching signal processing concept.

15. SUBJECT TERMS

Passive radar, radar imaging, synthetic aperture radar, bistatic radar, OFDM, broadband communication networks, WiMAX.

16. SECURITY CLASSIFICATION OF:			17. LIMITATION OF ABSTRACT	18. NUMBER OF PAGES	19a. NAME OF RESPONSIBLE PERSON
a. REPORT	**b. ABSTRACT**	**c. THIS PAGE**	UU	153	Dr. Julie A. Jackson
U	U	U			**19b. TELEPHONE NUMBER** *(include area code)* (937) 255-3636 x4678 julie.jackson@afit.edu

Standard Form 298 (Rev. 8-98)
Prescribed by ANSI Std. Z39.18